공학박사학위논문

Rational engineering of composite micro structures for advanced dry adhesion system

복합 미세 구조의 최적설계와 건식접착 시스템 응용

2014 년 2 월

서울대학교 대학원

협동과정 바이오엔지니어링

배 원 규

Rational engineering of composite micro structures for advanced dry adhesion system

복합 미세 구조의 최적설계와 건식접착 시스템 응용

지도교수 전 누 리

이 논문을 공학박사 학위논문으로 제출함

2013 년 10 월

서울대학교 대학원

협동과정 바이오엔지니어링

배 원 규

배원규의 공학박사 학위논문을 인준함

2013 년 12 월

위 원 장 : 구 중 서 (인)

부위원장 : 전누리 (인)

위 원 : 김희찬 (인)

위 원 : 정훈이 (인)

위 원 : 황석연 (인)

Abstract

In this thesis, we describe the bio-inspired design and fabrication methods to mimic scalable hierarchical structure in Nature and exploited 3 representative structures; lotus life, gecko's feet and extra cellular matrix (ECM). Multiscale, hierarchically patterned surfaces such as lotus leaves, butterfly wings, adhesion pads of gecko lizards are abundantly found in nature, where microstructures are usally used to strengthen the mechanical stability while nanostructures offer the main functionality, i.e., wettability, structural color, or dry adhesion. To emulate such hierarchical structures in nature, multiscale, multilevel patterning has been extensively utilized for the last few decades towards various applications ranging from wetting control, structural colors, to tissue scaffolds. In this thesis, we suggested simple yet robust fabrication method to scalable multiscale patterning to bring about improved functions that can even surpass those found in nature, with particular focus on the analogy between *natural* and *synthetic* architectures in terms of the role of different length scales.

First, we present here an enhanced dry adhesive skin patch with composite micropillars; the stem region of the pillars is formed by a relatively rigid material like hard polydimethylsiloxane (h-PDMS) (Young's modulus: ~8.2 MPa) or PDMS with a higher amount of curing agent, e.g., 15% (Young's modulus: ~2.8 MPa). The top layer is additionally integrated by transferring a soft PDMS layer

with a lower amount of curing agent, e.g., 5% (Young's modulus: ~0.8 MPa). In this way, monolithically integrated composite PDMS micropillars can be prepared with better adhesion strength and durability.

Next, we present a simple method of fabricating robust dry adhesives by coating a soft polydimethyl siloxane (PDMS) thin layer on rigid backbone micropillars of polyurethane acrylate (PUA). These core-shell type micropillars demonstrated enhanced durability both in normal and shear adhesion over more than 100 cycles of attachment and detachment. Relatively strong normal (~11.4 N/cm^2) and shear (~15.3 N/cm^2) adhesion forces were observed, which were similar to or even larger than those of homogeneous PDMS micropillars. A simple theoretical model based on beam deflection theory was used to explain the experimental results.

Finally, Inspired from exceptional climbing ability of gecko lizards, rtificial fibrillar adhesives have been extensively studied over the last decade both experimentally and theoretically. Therefore, a new leap towards practical uses beyond the academic horizon is timely and highly anticipated. To this end, we present a fibrillar adhesive in the form of bridged micropillars and its application to a transportation system with the detachment mechanism inspired by the climbing behaviour of gecko lizards. The adhesive shows strong normal attachment (~30 N/cm^2) as well as easy and fast detachment within 0.5 sec without involving complex dynamic mechanisms or specific stimulus-responsive

materials. The fabrication of the bridged micropillars consists of replica moulding of polydimethylsiloxane (PDMS) micropillars, transfer of the PDMS precursor to the heads of micropillars, and inverse placement on an inert Teflon-coated surface. Owing to spontaneous interconnections of low viscosity PDMS precursor, bridged micropillars with a uniform capping nanomembrane (~800 nm thickness) are formed over a large area. Interestingly, macroscopic adhesion in normal direction can be immediately switched between on and off states by changing the two detachment modes of pulling and peeling, respectively. To prove the potential of the fibrillar adhesive for practical use, an automated transportation system is demonstrated for lifting and releasing a mass of stacked glass slides over 1000 cycles of attachment and detachment.

Key Words : Biomimetics, Multiscale structure, Hierarchical structure, Patterning, Nanofabrication

Student Number: 2009-21069

Contents

List of Figures

an optimal adhesion force of up to ~1.8 Ncm^{-2} was observed for the 5 wt% curing agent.

Figure 2-3. (a) Durability tests of composite micropillars with comparisons to homogeneous micropillars and commercially available acrylic medical patch. As shown, the adhesion was maintained at ~1.8 Ncm^{-2} over 30 repeating cycles of attachment and detachment for the composite micropillars. The stem region of composite micropillars is enforced with 15 wt% curing agent of PDMS, showing good physical integrity and uniformity (i). For the homogeneous micropillars, the adhesion is continuously deteriorated via structural collapses (ii). The results with low modulus PDMS (7.5 wt% curing agent) and acrylic adhesive are adapted from our previous report.[142] (b) SEM images of replicated low-modulus PDMS (5 wt% curing agent) micropillars, showing that the tip layer is easily torn-off in the demolding procedure.

Figure 2-4. (a-b) Photographs showing the use of dry adhesive patch as a fixation unit in ECG module on the volunteer's chest (relatively flat surface) (a) and wrist (large curvature surface) (b). The inset images show the corresponding ECG signals from the volunteer's heart. (c) A schematic illustration of the inserted electrode along with an actual image on the skin (inset).

Figure 3-1. (a) Schematic illustration of fabricating PDMS-coated PUA micropillars (core-shell micropillars) by replica molding and thin film wetting. (b) An SEM image of the as-formed PUA micropillars along with a cross-sectional view. (c) An SEM image of the PDMS-coated PUA micropillars along with a cross-sectional view. The inset shows a cross-sectional TEM image, indicating that the thickness of PDMS skin is 100 to 200 nm.

Figure 3-2. (a-b) Measurement of (a) macroscopic normal and shear

PDMS (step 3) and bridged micropillars after squeezing the PDMS liquid (step 4).

Figure 4-3. Optical images showing that the fidelity of bridged micropillars depends on the mixing ratio of spin-coated PDMS in n-hexane, (a) 1:1, (b) 1:3, and (c) 1:10. The inset SEM images display a side-view of each case.

Figure 4-4. Time-force plot of the bridged and straight micropillars when detached (a) in the pulling mode and (b) the peeling mode, respectively. Also shown are the corresponding illustrations for crack trapping or propagation at the bottom panel. In the pulling mode, the bridged micropillars show a larger maximum adhesion force of ~29.6 N cm^{-2} than that of the straight micropillars. Also, the former exhibits a more prompt detaching response that is associated with single crack propagation via the monolithic capping membrane. In the peeling mode, while the maximum normal load of each sample was decreased to ~2 N cm^{-2}, the bridged micropillars still show a quicker detaching response as compared to that of the straight micropillars.

Figure 4-5. (a) Change of macroscopic normal adhesion force of the bridged micropillars as a function of applied preload. The decrease of adhesion force after passing the maximum point may be associated with the elastic energy of the back film that is stored by the compressive deformation due to an excessive normal preload as illustrated in the middle panel in the order of 1 to 3 with the increase of the preload. The structures remain intact even after applying the preload of 100 N cm^{-2}, as seen from the inset SEM images. (b) Durability test of the bridged micropillars over 1000 cycles of attachment and detachment.

Each sample was attached on a glass surface under the preload of 30 N cm^{-2} and detached in the pulling mode.

Figure 4-6. (a-d) Demonstration of a prototype of automated transportation system based on the fibrillar adhesive with bridged pillars. (a) A stack of three glass slides was lifted from the stage in the pulling mode enabling the maximum macroscopic adhesion force and (b) laid on the stage again in the peeling mode by switching to the minimized adhesion force. (c-d) Photographs showing the operation of the system (c) in the pulling and (d) peeling modes, respectively. (e) Plot of normal adhesion over 50 cycles under the preload of 30 N cm^{-2}, demonstrating a large difference in macroscopic normal adhesion force between on and off states. (f) Comparison of straight and bridged micropillars in terms of working time or yield of the operation with repeated cycles. The working conditions are as follows: displacement = 3 mm in normal direction, lifting speed = 0.6 mm/s, lowering speed = 0.3 mm/s, preload = 30 N cm^{-2} for 3 s.

Figure 5-1. (a) Schematic diagram to fabricate dual-scale structures on metallic surfaces by WEDM. By using a single step machining of sinusoidal patterns, a secondary roughness is spontaneously formed due to surface exfoliation process. (b) Optical image of the droplets of dyed-DI water on the fabricated aluminum surface in (a). (c) The SEM images of patterned metallic surface with distinct dual-scale structures.

Figure 5-2. (a) Schematic diagram of WEDM process.(b) A waveform of voltage between a workpiece and a wire electrode

Figure 5-3. Schematic of the fabrication process with different machining conditions to obtain rough surface (a) and smooth surface (b). (c) SEM images of the secondary roughness with various cutting conditions.

Figure 5-4. (a) Three-dimensional images of metallic surfaces after WEDM process taken by surface profiler. As shown, the 1^{st} cut with higher energy produces the roughest surface compared to those in the 2^{nd}, 3^{rd}, and 4^{th} cuts with lower energy. The static wetting angles on the corresponding surfaces are shown in (b) together with theoretical models using the Wenzel (purple line) and Cassie (blue line) states. Note that experimental measurements are highly matched with the Cassie state in all surfaces with relatively low CAHs; 8.2°, 10.7°, 13.2°, 15.8° respectively.

Figure 5-5. (a) SEM images of hierarchical structures on metallic surfaces with various wavelengths (λ) of sinusoidal micropatterns. The optical images of water droplets are shown in the inset. (b) Static wetting angles on the various samples in (a) with comparison to theoretical models. As shown, the wetting states are highly matched with the *C'-C"* state (superhydrophobic) for the samples with λ = 400 μm and 500 μm with one- or two-step WEDM process. For three-step WEDM process or higher, a transition to the *W'-C"* state is observed. For the

the pattern. The cross–sectional SEM images show an example of reduced spacing by ~75% with respect to the original size. Finally, the SMP sheet recovers its original shape after heating to the second programming temperature of 115℃.

Figure 6-2. SEM images showing the pattern evolution when the first and second programming temperatures are the same ($T_{trans} = T_{im}$ = 80℃): (a) initial nanoimprinted structure (500 nm line, 400 nm spacing and 500 nm depth), (b) a rounded structure with a reduced depth (~ 250 nm) when heated at 84℃ and (c) a further flattened structure (depth: ~ 150 nm) after recovery process at 86℃. As shown, the pattern gradually disappears as the temperature increases. Here, the horizontal contraction corresponds to the first programming, while the vertical recovery to the second programming,

Figure 6-3. SEM images for the fabrication of various size-controllable nanopatterns by TME and self-replication of a UV curable PUA mold: (a) Initial imprinted SMP pattern with 400 nm width and 400 nm spacing. (b) Reduced spacing to 250 nm (37.5% reduction) when heated to 84℃, (c) Reduced spacing to 100 nm (75% reduction) when heated to 86℃. (d) Inverse replica of patterned SMP with 100 nm width and 400 nm spacing after replica molding and self-replication. (e) Reduced spacing to 250 nm (37.5% reduction) when heated to 84℃. (f) Reduced spacing to 100 nm (75% reduction) when heated to 86℃.

Figure 6-4. Pattern formation with a 200 % uni-directionally stretched

SMP sheet (shrink ratio = 3:1). SEM images showing (a) silicon master mold for NIL, (b) imprinted SMP pattern, (c) the same after recovery process at 86℃ (spacing: 250 nm), and (d) the same after recovery process at 89℃ (spacing: 70 nm).

Figure 6-5. Fabrication of gradient patterns by a temperature gradient: (a) Fabrication of a SMP gradient pattern by local heating. As shown, multiscale patterns ranging from 1 μm to 250 nm (75% reduction) were formed on the same SMP substrate. (b) SEM images of the replicated PUA pattern from the patterned SMP. (C) Schematic of fabricating multiscale SMP gradient channels. Fluorescent images of a Rhodamine B dye in DI water after introduction into the channels by surface-tension driven flow.

Nomenclature

γ_{SV}	Interfacial tension at the solid/vapor interface
γ_{SL}	Interfacial tension at the solid/liquid interface
γ_{LV}	Interfacial tension at the liquid/vapor interface
z	Length of capillary movement
θ	Contact angle
γ	Surface tension
λ	Wave length
SV	Interface of solid/vapor
SL	Interface of solid/liquid
LV	Interface of liquid/vapor
n	Refractive index
E	Elastic modulus
A	Hamaker constant
F_f	Friction force
F_{vdw}	Van der Waals force
F_{shear}	Total shear adhesion
R	Radius of hairs
l_o	Length of hairs

Chapter 1. Introduction

The multiscale structural hierarchies of biological materials in nature possess various inspiring properties; these provide us with creativity or design rule for the fabrication of artificial, nature-inspired multiscale structures with multifunctional properties.[1, 2-4] Structural hierarchies can be observed in various biosystems such as lotus leaves, gecko feet,[5] insect compound eyes,[6] spider silks,[7, 8] bone, nacre, and shell.[9, 10, 11] A significant feature of these creatures is that they exhibit highly characteristic hierarchical structures from the nano- to the microscale. Interestingly, each microstructure and nanostructure has different roles, in which microstructures have a significant influence on the mechanical properties of the system (e.g., stability, strength, and elasticity), whereas nanostructures induce unique properties (e.g., superhydrophobicity, structural color, and directional adhesion). Along with these unique features, these structures have received great attention in recent years due to their fascinating multifunctionality, e.g., superhydrophobicity, directional wetting, reversible adhesion, anti-reflection, selective filtration, and structural color. Such research has paved the way for various promising applications in the fields of biomimetics,[12, 13] biomedicine,[14] microfluidics,[15, 16] electronics,[16, 17] optics, and[18, 19] chemistry.[20] Inspired by these interesting multifunctions of biostructures, many researchers have performed experiments to reveal novel

functionalities and to develop diverse methods of fabricating multiscale hierarchical surfaces or structures based on the bottom-up, top-down, and hybrid approaches.

1-1. The role of multiscale, hierarchical structures in nature

Multiscale structural hierarchies can be observed in a variety of biological systems from nanosize proteins and microsize cells to macrosize organisms exhibiting multifunctional properties.[2, 21] In this section, we summarize the progress of recent research in examining typical multiscale hierarchical structures in nature with multifunctions. These structures can be divided into the following two categories: EHS such as gecko feet,[22] butterfly wings,[23] lotus leaves,[24] and rose petals,[25] and IHS such as spider silk,[8] armadillo shells,[10] bone,[22] fish scales[26] and plant stems.[27] These categories are shown in **Figure 1-1** together with an illustration that includes representative scanning electron microscope (SEM) image of the multiscale structural hierarchies. Especially, in this section, representative four examples in **Figure 1-2**; gecko, butterfly, bone materials, and glomerulus in kidney are discussed in detail in terms of their role of micro-/ nanostructures and additionally other interesting examples; water-repellent leaves, spider silk fibers, dermal armor, and plant stem are also presented.

The attachment pads of geckos represent one of the most versatile and

effective adhesives known in nature due to these animals' ability to run freely on various surfaces, including vertical walls.[5, 28, 29, 30] Microscopically, the gecko foot exhibits a representative multiscale hierarchical structure. It is composed of well-aligned microsize hairs called setae, of which the distribution density is 500 setae/mm^2; these branch into smaller nanoscale hairy structures called spatulae. The spatula tips have a size of approximately 200 nanometers, generating intermolecular force known as van der Waals force, which is the main reason for the remarkable adhesion of the gecko. It should be noted that the microsize hairy structure provides mechanical stability, which prevents lateral collapse of the fibers and provides an extremely high aspect ratio in the hairy structure of the gecko toe. In addition to this prominent adhesion feature, the gecko toe also exhibit multifunctions such as superhydrophobicity and self-cleaning properties due to the characteristics of the multiscale structural hierarchy. Mimicking the high adhesion force and self-cleaning abilities of the gecko foot, a series of artificial dry adhesives have recently been fabricated.

Another interesting example of a multiscale structural hierarchy in nature is the butterfly, specifically Morpho butterfly wing scales.[19, 31] These butterflies are famous for their amazing and beautiful blue iridescent colors, which come from a novel multiscale hierarchical structure on their wing scales. The Morpho butterfly has a brilliant blue coloration on the top surface of the wings, whereas it exhibits a camouflaged brown coloration on the underside of the wings. Such

coloration, called structural color, help these butterflies to avoid predators such as bird when they fly, the brown color on the ventral side of the wings matches their surroundings when they land. The iridescent colors of the butterfly come from the well-defined and sophisticated hierarchical structure from the nanometer to micrometer and millimeter size on the wing scales. It should be noted that the multiscale structure of the scales plays an important role in determining their multifunctional properties. This causes structural coloration and superhydrophobicity, which are both critical properties for the butterflies to fly in the rain.

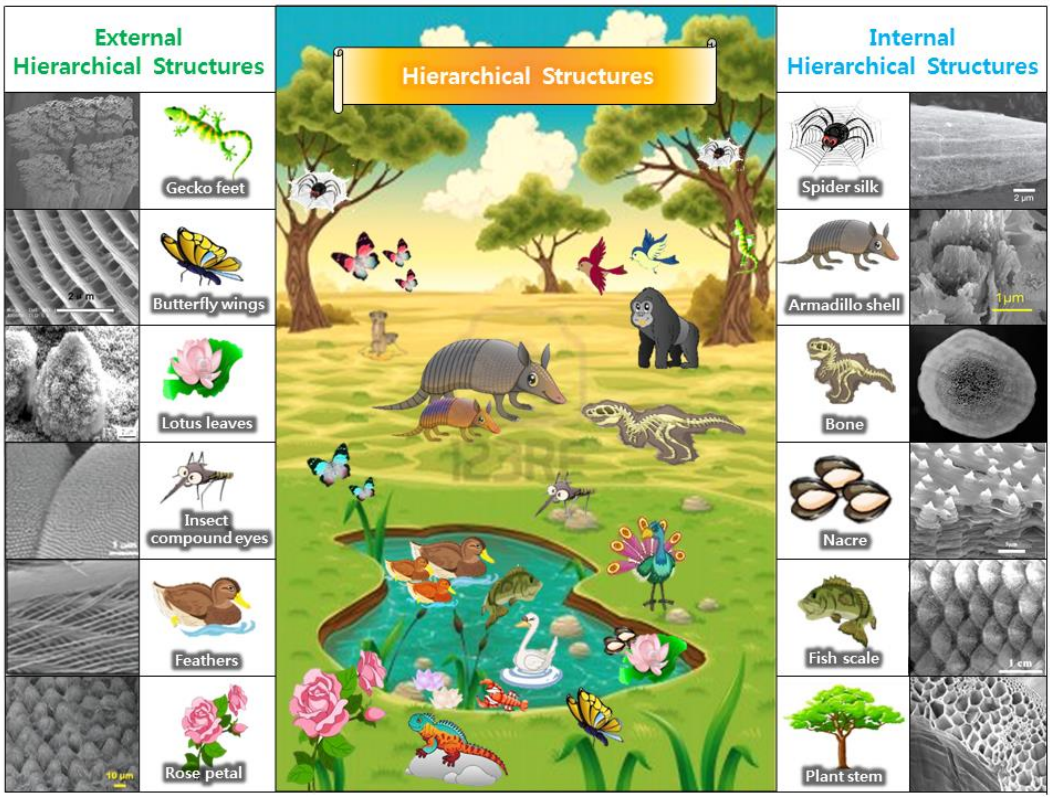

Figure 1-1. Typical biological multiscale hierarchical structure with multifunctional properties in nature. Multiscale structure can divided into two categories; external multiscale hierarcical structures; gecko feet, butterfly wings, lotus leaves, insect compound eyes, feathers and rose petal and internal multiscale hierarchical structures; spider silk, armadillo shell, bone, nacre, fish scale and plant stem. In each case typical illustration images and scanning electon microscopy (SEM) images of corresponding multiscale structure are presented.

In addition, their wings show directional adhesion due to an oriented one-dimensional arrangement covered by lamella-stacking microsize stripes, on which water can easily roll along in the outward direction. In addition to these two interesting properties, butterfly wings also show a chemical-sensing capability and fluorescence-emission function caused by their structural hierarchy. These multifunctional properties of butterfly wings have inspired many researchers to mimic and learn the design role of hierarchies in nature, resulting in various outstanding research results.

A representative example of multilevel structural hierarchy in the human body is bone materials with prominent mechanical properties.[32] It should be noted that bone has a hierarchical structure consisting of a nanometer-sized, very hard mineralized component in a soft protein matrix. From a structural viewpoint, bone can be divided into two different material parts—a dense external shell and a spongy interior part. The combination of nano- and microstructures exhibits optimized mechanical performance in terms of rigidity and resistance against fracture, whereas, nanoscale structure could influence cell behavior such as orientation, alignment, attachment and other important functions, inspiring many materials scientists to develop new composite materials with unique mechanical properties and functionalities.

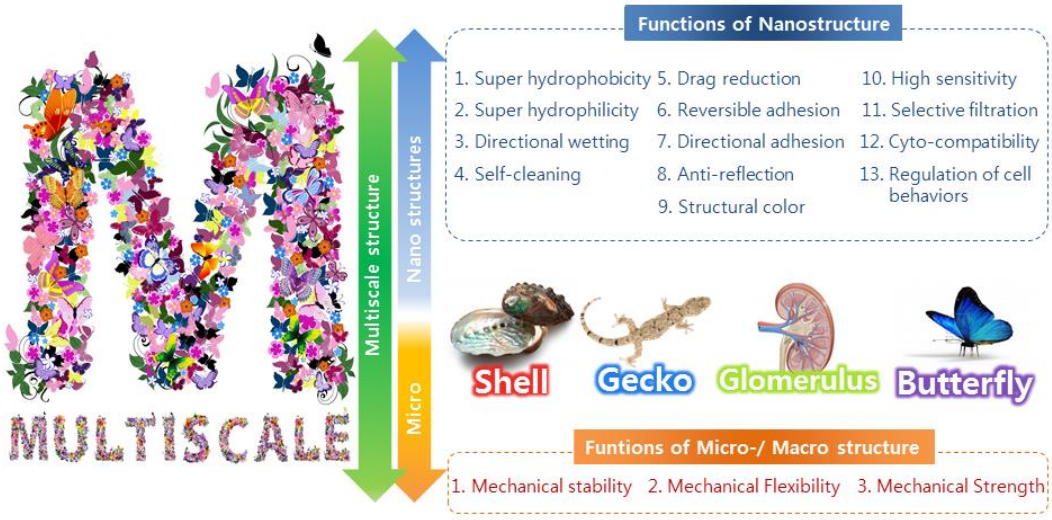

Figure 1-2. Functions of macro/micro- and nanostructures in their hierarchical organizations. In general, a large scale structure serves as a mechanical support to enhance strength, stability, and flexibility, while a nanostrucutre provides the main functionality such as directional wetting, reversible adhesion, low friction, light reflection, selective filtration, and so on. The character “M” is comprised of many small butterflies symbolizing the role of multiscale hierarchy. On the right panel, four representative examples of multiscale structures are shown: shell, gecko, glomerulus in kidney, and butterfly wing.

In the filtration system in our body, the glomerulus in kidney is typical example of hierarchical structure. The glomerular capillary wall forms a sophisticated filter, which permits water and small plasma solutions to pass into the urinary area, while preventing albumin and larger molecules from being filtered.[33] The glomerular basement membrane (GBM), which is one of the filtration barrier layers, contains a unique composition of collagen type Ⅳ and laminin molecules in which the laminin network is crucial for the filter function. The pedicel layers, which is another filtration barrier layers, act as a supporting structures providing mechanical strength to support their filtration barriers. Recently, inspired by ability of selective filtration in glomerular capillary, nanoporous membranes and nanostencils for mass transport have been explored for biomolecule separation, detection and purification. In artificial nanoporous stencils, the microsize structures play a role in mechanically supporting free-standing nano membrane, whereas porous membranes provide a highly selective transport property.

The water-repellent leaves of lotus and rice plants exhibit special wettability characters, such as superhydrophobicity and self-cleaning properties, because of their unique surface structural hierarchy.[13, 34] In the case of the lotus leaf, it has randomly distributed micropapillae with branch-like nanostructures, providing superhydrophobic and low-adhesion functions in which the water droplets can roll freely in all directions. The fine, branch-like nanostructures

guarantee the robustness of superhydrophobicity on its surface. On the other hand, rice leaves exhibit superhydrophobicity and anisotropic wettability. Their multiscale hierarchical structures on the surface possess arranged micropapillae with a one-dimensional order, resulting in anisotropic wettability. Another typical example of a plant with a superhydrophobic surface is the rose petal. This exhibits multifunctions, specifically superhydrophobicity, high water adhesiveness, and structural color due to the multiscale structure on its surface. Because of the unique nanofold structure on micropapillae, they demonstrate superhydrophobicity and high water adhesion. In addition, their combination of periodic arrays of micropapillae and nanostructures on top surface of the leaf results in the structural color of the red rose leaf.

Another interesting creature with a multiscale structural hierarchy in nature is the spider.[35] Spider silk fiber has novel properties such as high mechanical strength, continuity, insolubility in water, and the generation lightweight orb-webs for prey capture. In addition, the spider silk web can capture a significant amount of water droplets and withstand harsh environment such as wind, rain, and sunlight. Spider silk has multiscale hierarchical structures from the nano- to microscale, and the hierarchical organization at these levels plays an important role in achieving the mechanical and physical properties of the silk. Specifically, the structure of spider silk consists of electron density at the atomic scale, as well as β-sheet nanocrystals and a semi-amorphous phase at the

nanoscale; these properties assemble into macroscopic silk fibers. The spider generates two types of silk fibers: dragline silk and capture silk. These are used for different purposes. Dragline silk exhibits amazing mechanical properties that are excellent compared to most natural and synthetic materials due to their unique structural hierarchy in terms of chemical composition and morphological structure. On the other hand, capture silk has other unique properties, e.g., exceptional elasticity, strength, and adhesiveness, because their main role is to capture high velocity insects when flying with a high damping capacity. In addition, capture silk possesses directional water-collection ability because of its unique multiscale fiber structure with periodic spindle-knots. Due to the special multifunctions of spider silk, a number of studies have been conducted to mimic their mechanisms.

Another representative example of an IMSH is dermal armor. Many animals, including mammals, reptiles, and fish have flexible dermal armor for protective purposes and other unique multifunctions.[3, 11] The scales of fish and the armor of armadillos have a multiscale hierarchical structure with collagen fibers joining with more mineralized hard components, resulting in significant flexibility and high strength. Furthermore, these dermal hierarchical structures exhibit multifunctional properties such as waterproofing, hydrodynamic drag, fluid regulation, luminescence, and coloration for camouflage. For example, fish scales are composed of two different layers: an external and internal layer. The external layer of the scale is highly mineralized, providing sufficient hardness

against external attack, while the internal layer has softer collagen fibers that create a buffer layer to promote toughness. In addition, due to the surface roughness produced by the nanoscale structure, such scales exhibit unique wetting properties. The surface of carp scales is covered by microsize papillae with nanostructures, resulting in superoleophilicity in air and superoleophobicity in water, as well as having a drag-reducing function. The structure of an armadillo's shell also has a multiscale sandwich structure below the epidermis, comprising external dense bone, central porous bone, and internal dense bone layers to enhance external energy absorption and flexibility against attack by predator. The armadillo's outer epidermis, which is composed of α-keratin, also has multifunctional properties such as sufficient stiffness or hardness and waterproof characteristics due to this structural hierarchy.

Another multiscale, bone-like, porous structure in nature is the plant stem, e.g., tree stems and grass stems.[36] The novel porous structure of the stem exhibits outstanding mechanical stability and flexibility, providing mechanical support in strong wind. These unique mechanical properties come from the porous structural hierarchy in the stem. The outer shell of the stem has a denser structure than the porous structure of core. This is similar to the previously mentioned animal dermis. The multiscale hierarchical structure of plant stems, especially in terms of nano- and micropores, also acts as an artery to efficiently transport water or other nutrients, thereby overcoming gravity. In other words, the multiscale structure of

the stem exhibits multifunctional properties, specifically structural strength, mechanical stability, and an effective transport system to survive in harsh environments.

In ***Chapter 2***, we present here an enhanced dry adhesive skin patch with composite micropillars; the stem region of the pillars is formed by a relatively rigid material like hard polydimethylsiloxane (h-PDMS) (Young's modulus: ~8.2 MPa) or PDMS with a higher amount of curing agent, e.g., 15% (Young's modulus: ~2.8 MPa). The top layer is additionally integrated by transferring a soft PDMS layer with a lower amount of curing agent, e.g., 5% (Young's modulus: ~0.8 MPa). In this way, monolithically integrated composite PDMS micropillars can be prepared with better adhesion strength and durability.

In ***Chapter 3***, we present a simple method of fabricating robust dry adhesives by coating a soft polydimethyl siloxane (PDMS) thin layer on rigid backbone micropillars of polyurethane acrylate (PUA). These core-shell type micropillars demonstrated enhanced durability both in normal and shear adhesion over more than 100 cycles of attachment and detachment. Relatively strong normal (~11.4 N/cm^2) and shear (~15.3 N/cm^2) adhesion forces were observed, which were similar to or even larger than those of homogeneous PDMS micropillars. A simple theoretical model based on beam deflection theory was used to explain the experimental results.

In ***Chapter 4***, inspired from exceptional climbing ability of gecko lizards,

rtificial fibrillar adhesives have been extensively studied over the last decade both experimentally and theoretically. Therefore, a new leap towards practical uses beyond the academic horizon is timely and highly anticipated. To this end, we present a fibrillar adhesive in the form of bridged micropillars and its application to a transportation system with the detachment mechanism inspired by the climbing behaviour of gecko lizards. The adhesive shows strong normal attachment (~30 N/cm^2) as well as easy and fast detachment within 0.5 sec without involving complex dynamic mechanisms or specific stimulus-responsive materials. The fabrication of the bridged micropillars consists of replica moulding of polydimethylsiloxane (PDMS) micropillars, transfer of the PDMS precursor to the heads of micropillars, and inverse placement on an inert Teflon-coated surface. Owing to spontaneous interconnections of low viscosity PDMS precursor, bridged micropillars with a uniform capping nanomembrane (~800 nm thickness) are formed over a large area. Interestingly, macroscopic adhesion in normal direction can be immediately switched between on and off states by changing the two detachment modes of pulling and peeling, respectively. To prove the potential of the fibrillar adhesive for practical use, an automated transportation system is demonstrated for lifting and releasing a mass of stacked glass slides over 1000 cycles of attachment and detachment.

In ***Chapter 5***, we present a novel method to fabricate dual-scale superhydrophobic metallic surfaces using wire electrical discharge machining

(WEDM). A dual-scale structure was spontaneously formed by the nature of exfoliation characteristic of Al 7075 alloy surface during WEDM process. A primary microscale sinusoidal pattern was formed via a programmed WEDM process, with the wavelength in the range of 200 to 500 μm. Notably, a secondary roughness in the form of microcraters (average roughness, Ra: 4.16 to 0.41 μm) was generated during the exfoliation process without additional chemical treatment. The low surface energy of Al 7075 alloy (γ = 30.65 mJ/m^2) together with the presence of dual-scale structures appears to contribute to the observed superhydrophobicity with a static contact angle of 156° and a hysteresis less than 3°. To explain the wetting characteristics on dual-scale structures, a simple theoretical model was used. It was found that Cassie state is likely to present on the secondary roughness in all fabricated surfaces. On the other hand, either Wenzel or Cassie state can present on the primary roughness depending on the characteristic length of sinusoidal pattern. In an optimal condition of the serial cutting steps with applied powers of ~30 kW and ~8 kW, respectively, a stable, superhydrophobic metallic surface was created with a sinusoidal pattern of 500 μm wavelength.

In ***Chapter 6***, we introduce a new nanoimprint lithographic method to reduce the pitch and size of nanopatterns using temperature memory effect (TME) in shape memory polymers (SMPs). To utilize the temperature memory effect, two

thermal programming steps were devised at the transition (Ttrans = 80°C) and higher imprinting (Tim = 115°C) temperatures. In the first programming, a sheet of polyethylene-based SMP (thickness: 100 μm, size: 3 × 3 cm2) was uni-directionally stretched by 100%. In the second programming, thermal nanoimprinting was performed with a silicon master onto the first programmed SMP sheet. When the sheet was heated above Ttrans, the pattern spacing started to be shrunken in proportional to the amount of temperature rise, with the line width fixed for T <. Tim. With further temperature rise to or above Tim, the patterns were completely removed, recovering the original shape of the sheet. By exploiting self replication characteristics, various size-controllable nanopatterns were generated with reduced pitches and sizes.

Chapter 2. Enhanced skin adhesive patch with modulus-tunable composite micropillars

2-1. Introduction

The term “ubiquitous healthcare” (U-healthcare) refers to the delivery of health related services and information via ubiquitous computing and wiring technologies. There are several forms of U-healthcare ranging from simple conversations over the telephone between a patient and a doctor to telemedicine consultation via videoconferencing or robotic technology. With rapid transition to an aging society, such U-health devices are considered to play a key role in future diagnostics and healthcare systems.[37]

In general, a U-health device may consist of two units: (1) an organ signal detection/wiring component for diagnostics and (2) an adhesive patch that can fix the device on the human skin. Traditionally, an acrylate-based adhesive patch has been widely used as the adhesive unit due to its strong adhesive properties (e.g., for 3M electrode unit, adhesion force is ~3 N/cm^2). With increasing demands on long-term uses for U-healthcare, especially for the aged, a simple method of fabricating less skin-irritating and biocompatible patches is potentially of great benefit.[38]

Recognizing such needs for a new biocompatible medical patch, we have shown in our recent study[39, 40] that the dry adhesive skin patch possesses several potential advantages as compared to acrylic-based chemical adhesives. First, the dry adhesive patch showed repeatable and restorable adhesion, and was less affected by surface contamination, oxidation, and other environmental factors with the help of an external cleaning process (e.g., water wash or scotch taping). This is due to the fact that the adhesion largely originates from the structural characteristics of high-density micropillars.[4, 41, 42, 43] Second, it provided better biocompatibility in a prolonged exposure presumably due to increased ventilation of air, moisture, and skin residues with minimal contact with potentially irritating chemical species.[39] Despite these advantages, the relatively low normal adhesion (maximum adhesion force: ~1.3 Ncm^{-2}) may be a hurdle to practical uses of the dry adhesive patch with homogeneous mushroom-like micropillars.

To address this limitation, we present here an enhanced dry adhesive skin patch with composite micropillars; the stem region of the pillars is formed by a relatively rigid material like hard polydimethylsiloxane (h-PDMS) (Young's modulus: ~8.2 MPa) or PDMS with a higher amount of curing agent, e.g., 15% (Young's modulus: ~2.8 MPa).[44, 45] The top layer is additionally integrated by transferring a soft PDMS layer with a lower amount of curing agent, e.g., 5% (Young's modulus: ~0.8 MPa) [46] In this way, monolithically integrated composite PDMS micropillars can be prepared with better adhesion strength and durability.

It is worthwhile noting that such a composite structure is inspired by the gecko' toe pad in which micro and nanohairs are hierarchically organized to give strong, yet reversible attachment against surfaces of varying roughness and orientation (adhesion force of ~10 N/cm^2).[47, 48] Interestingly, the bottom part of hairs (seta) has large diameters of ~4.2 μm to secure mechanical stability, which is then branched into 100 to 1000 tiny units of nano-sized spatulae for enhanced contact. Therefore, the spatula tip may be considered as a highly soft contact unit with an overall effective modulus as small as ~110 kPa, despite that the entire hairs are composed of rigid β-keratin with the modulus in the range of 1~3 GPa.[49]

2-2. Experimental

Fabrication of SOI Master Mold, a SOI (silicon-on-insulator) wafer was purchased from Mico MST Ltd. (Korea). The wafer was composed of 3 layers: a p-type (100) bare silicon wafer (resistivity: 1~30 Ω), a SiO2 etch-stop layer of 500-nm-thickness, and a polysilicon layer of 15-μm thickness. A 800-nm-thick SiO2 layer was deposited on the SOI wafer by plasma-enhanced chemical vapor deposition process with tetraethoxysilane (TEOS). Holes of 5 μm in diameter and 15 μm in height were made by conventional photolithography with AZ1512 photoresist. Anisotropic dry etching was subsequently carried out in an inductively coupled plasma (ICP) etching system with SF6 and Ar gas plasma in order to remove the polysilicon layer until the exposure of the SiO2 etch-stop layer. Under the same etching condition, the polysilicon layer was further etched to the lateral direction to replicate mushroom-like micropillars. For clean release, the SOI master was treated with a fluorinated self-assembled-monolayer (SAM) solution ((tridecafluoro- 1,1,2,2-tetrahydrooctyl)-trichlorosilane: FOTCS, Gelest Co.) diluted to 0.03 M in anhydrous heptane (Samchon Co.) in an Ar chamber. The surface-treated master was annealed at 120 ℃ for 20 min.

Fabrication of Enhanced Skin Adhesive by Inking Method, The stalk PDMS micropillars were made by mixing the PDMS base (Sylgard A, Dow Corning, USA) with the 15 wt% curing agent (Sylgard B, Dow Corning, USA).

After degassing and curing at 70 ℃ for 1 hr, the PDMS replica was carefully detached from the master. Subsequently, the replica was placed on a low-modulus PDMS (curing agent: 2.5 to 15 wt%) layer (thickness ~500 nm) spin-coated on glass substrate at 3000 rpm for 60 s after dissolving in n-hexane (Daejung Chemicals & Metals Co.). During this step, a soft PDMS layer was selectively transferred to the head of micropillars. Then, the PDMS replica was inversely placed (pillars facing the surface) on a Teflon substrate in order to make the pillar tip flattened and easily released from the surface. While maintaining a uniform contact, the inked PDMS replica was cured at 70 ℃ for 1 hr. After curing, the monolithically integrated composite micropillars were carefully removed from the Teflon substrate to be used as a skin adhesive.

Scanning Electron Microscopy (SEM), SEM Images were taken with high-resolution SEM (S4800, Hitachi, Japan) at an acceleration voltage higher than 5 kV and a working distance of 8 mm. Samples were coated with a 3-nm Au layer prior to analysis to prevent electron charging.

Normal Adhesion Tests on Skin, The macroscopic normal adhesive forces were measured by a pulling test on the back of a male volunteer’s hand. Prior to the adhesion test, the skin was shaved completely to prevent the influence of hairs and fatty surface. Then, an adhesive (thickness: 1 mm, area: 1 × 1 cm2) was attached to the skin under a preload of ~0.3 N cm−2 and the adhesive force was measured by gradually increasing the pulling weight until adhesion failure

occurred. The same measurement was performed with a pristine PDMS sheet (thickness: 1 mm, area: 1 × 1 cm2). For statistical significance, the adhesion measurement was carried out 50 times for each sample under identical conditions (i.e., relative humidity of 40% and ambient temperature of 25℃) and the averaged data were used throughout the experiment.

2-3. Results and Discussion

In our recent report, we presented direct, one-step replica molding of mushroom-like micropillars to fabricate a dry adhesive medical patch. Here, an optimal dry adhesive patch was observed by adding 7.5 wt% of curing agent (Sylgard B) into the PDMS base (Sylgard 184A).[39] A further reduction of curing agent caused a failure in the demolding process, i.e., the pillars were stuck or torn off from the master in the demolding step. Furthermore, low-modulus PDMS pillars are prone to collapse or mating between the neighboring ones.[50] An increase of curing agent also results in a decrease of the adhesion force owing to elevated elastic modulus of the micropillars. We further demonstrated a rational design rule for skin-attachable dry adhesive that needs to incoporate the effect of complex, dual-scale roughness (macro- and microscale) on the human skin. It was found that the thickness of a backing layer determines the compliance on a rough skin surface with macroscale roughness, while the mushroom-like micropillars can make an intimate contact with microscale undulations.

The current method consists of two sequential steps of replica molding and inking. Figure 2-1a illustrates a schematic diagram of the experimental procedure. First, relatively rigid mushroom-like micropillars were directly replicated from the silicon-on-insulator (SOI) master having 5-μm holes using a high modulus PDMS of 15% curing agent (see experimental details). Here, a thin SiO2 etch-stop layer

of the SOI wafer was used to control dry etching, first in the vertical direction and second in the lateral direction right on the etch-stop layer. This method is advantageous over our earlier approach since the entire etching can be carried out in one step without changing the etching conditions.[47, 51, 52] After replicating the mushroom-like micropillars, a soft PDMS layer was selectively transferred to the head of micropillars by placing the PDMS replica in conformal contact with a thin spin-coated PDMS layer (thickness of ~500 nm) on glass substrate. The amount of curing agent was controlled from 2.5 to 15 wt%. No pressure was applied in the inking step with the duration of 10 s. In order to make the tip shape flat and smooth, we cured the composite PDMS pillars by inversely placing (pillars facing downward) onto a Teflon-coated, low-surface-energy substrate without application of a pressure. Then, the tip became flattened and clearly released from the Teflon-coated substrate after curing.[53]

Figure 2-1b shows a conceptual image of the dry adhesive patch along with a representative SEM image of fabricated micropillars (diameter, 5 μm; height, 15 μm). As shown, the micropillars are defined with good physical integrity and uniformity. Here, the stem region acts as a stabilizing structural component, whereas the tip layer provides an efficient contact component on the human skin. To verify the selective inking of a soft PDMS layer, the half of micropillars was contacted with a PDMS layer containing red-fluorescent Rhodamine B dye. There is a clear demarcation between the contacted and non-

contacted regions as shown in Figure 2-1c, suggesting that the inking is highly selective and controllable within the contacted areas. Two reaons may be responsable for this observation: limited mass transfer and meniscus pinning. Since the amount of the spin-coated layer is limited to ~500 nm thickness, it would be hard to wet the entire pillars. Also, the mushroom-like profile may prevent the PDMS precursor from filling into the cavity due to the pinning of a meniscus to the entrant part of pillars.

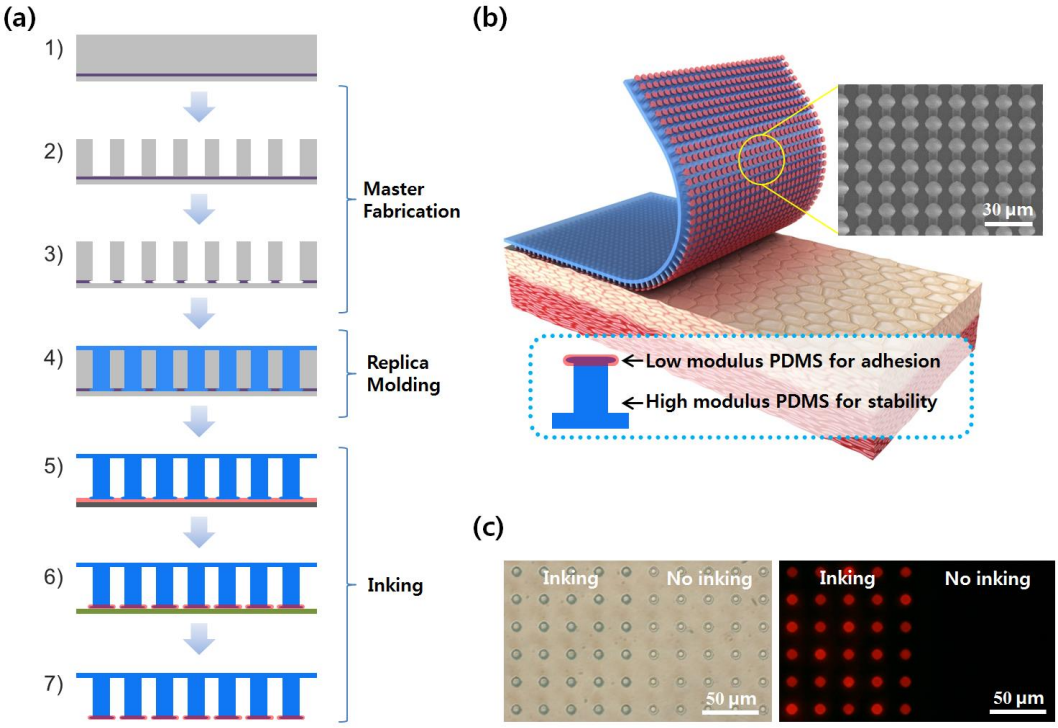

Figure 2-1. (a) Schematic diagram of the fabrication procedure for modulus-tunable composite micropillars by replica molding and inking. (b) Conceptual illustration of dry adhesive skin medical patch along with a representative SEM image of replicated micropillars. (c) Optical and fluorescent images of the half-inked micropillars with red fluorescent dye (Rhodamine B).

Using the fabricated composite micropillars, we measured the adhesion force on the back of a volunteer's hand by varying the amount of curing agent (Figure 2-2). Also, the adhesion force of pristine PDMS (without patterns) was measured for comparison. For statistical significance, the adhesion measurement was carried out 50 times for each sample under identical conditions (i.e., relative humidity of 40% and ambient temperature of 25℃) and the averaged data were used. As shown, the adhesion force increased with the decrease of the curing agent up to 5 wt%. Note that there is a sharp jump of the adhesion force between 7.5 and 5 wt%. Interestingly, a further reduction of the curing agent (< 5 wt%) gave rise to a decrease of the adhesion force, which, as described earlier, is associated with the fact that micropillars are too soft to be replicated from the master and susceptible to structural collapses.[54, 55]

In order to explain the observed adhesion behaviors with a simple theory, we employ the traditional JKR model introduced by Johnson, Kendall and Roberts.[56] As is well documented, the adhesion of gecko lizards is characterized by numerous nano-sized spatula contacts at the end of each hierarchical hair, which is analogous to the current composite micropillars. In terms of the effective modulus, this hierarchical geometry leads to a lower effective modulus than that of the bulk material. In the present case, the tip of a composite micropillar possesses a relatively low modulus, allowing for enhanced conformal contact on the rough skin surface. Suppose that a skin roughness can be expressed as an array of

sphere-caps, i.e., $h = r - \sqrt{r^2 - \lambda^2 / 4}$, where *h* and *r* are the height and radius of the sphere cap, respectively, and λ is the separation distance between the caps. Then, the elastic deformation of the tip layer in contact with the skin can be evaluated after some algebraic manipulation on one unit cell, i.e., the contact between a single sphere cap and a flat spatula tip. The radius of the contact area is given by[57]

$$a_{JKR} = \left(\sqrt{\frac{9\pi w r^2}{8E}} + \sqrt{\frac{3\left(F + \frac{3}{2}\pi w r\right) r}{4E}} \right)^{2/3} \qquad (1)$$

where *w* is the work of adhesion, *F* is the preload, and *E* is the elastic modulus. It can be seen from the relation that the contact area becomes larger as the modulus decreases, which supports our results that the composite micropillars with low-modulus spatula shows a higher adhesion force than that of the homogeneous micropillars.

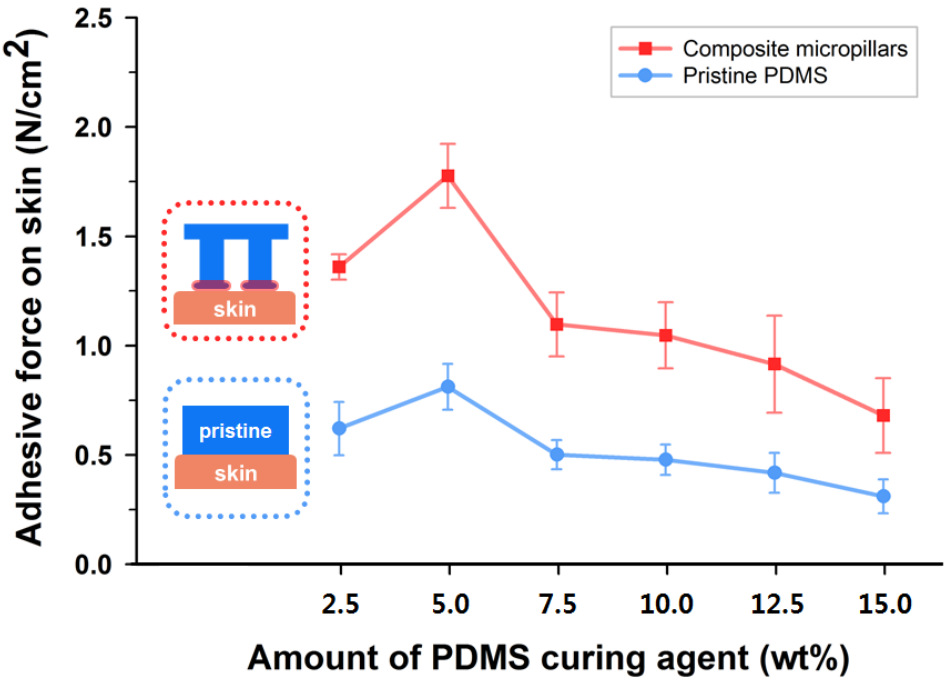

Figure 2-2. Changes of normal adhesion force for composite micropillars and flat PDMS on the back of a volunteer's hand with various mixing ratios of curing agent from 2.5 to 15 wt%. As shown, an optimal adhesion force of up to ~1.8 Ncm^{-2} was observed for the 5 wt% curing agent..

To elaborate on the detailed adhesion performance of the composite micropillars presented here, we performed durability tests with three different samples: composite micropillars (15 wt% stem region + 5 wt% tip layer), homogeneous micropillars (7.5 wt%), and commercially available acrylic medical patch. As shown in Figure 2-3a, the conventional medical tape with an electrode unit (3M monitoring electrode), starting from ~3 Ncm-2, shows a monotonic decrease of adhesion force after five-time uses due to the fact that contaminants are irreversibly adhered and not easily washed out on the sticky acrylic surface. Homogeneous micropillars also displayed a typical cyclic behavior of monotonic decrease of adhesion force and restoration by an external cleaning process such as water wash or scotch taping.[39] This is because the micropillars, which are intact when freshly replicated, are continuously destroyed via structural collapses with repeated uses (see SEM image on the right). In contrast, the composite micropillars were more stable and demonstrated superior durability over 30 cycles of adhesion and detachment (see SEM image on the right).

To gain an understanding on the increased durability of composite micropillars, a simple beam deflection model can be used: $V = PL^3 / 3EI$ where V is the displacement of micropillars, I is the moment of inertia, P is the pulling force when the micropillars are detached from the substrate, and L is the height of micropillars. Here, the stem region of composite micropillars has a higher modulus (15 wt% curing agent) than that of homogeneous micropillars (7.5 wt%

curing agent), which in turn yields a reduced displacement upon an external load. Such small displacement can be interpreted as lower chances of self-mating or collapse between the neighboring micropillars. Remarkably, the average adhesion force was maintained nearly at ~1.8 Ncm-2 with repeated cycles, which is approximately 65% of the current acrylic-based wet medical patch.

As shown above, the structural instability is greatly enhanced due to the existence of an enforced stem region of PDMS micropillars. For example, for the 15 wt% curing agent, the tensile strength is approximated to be ~1.1 GPa.[58] When low-modulus PDMS is used to replicate whole mushroom-like micropillars (e.g., 5 wt %), the tip layer is easily torn off in the demolding step, resulting in nearly straight pillars in many locations instead of mushroom-like ones (Figure 2-3b). These defects may account for continuous deterioration of the adhesion force of homogeneous mushroom-like micropillars used in our previous approach.[39]

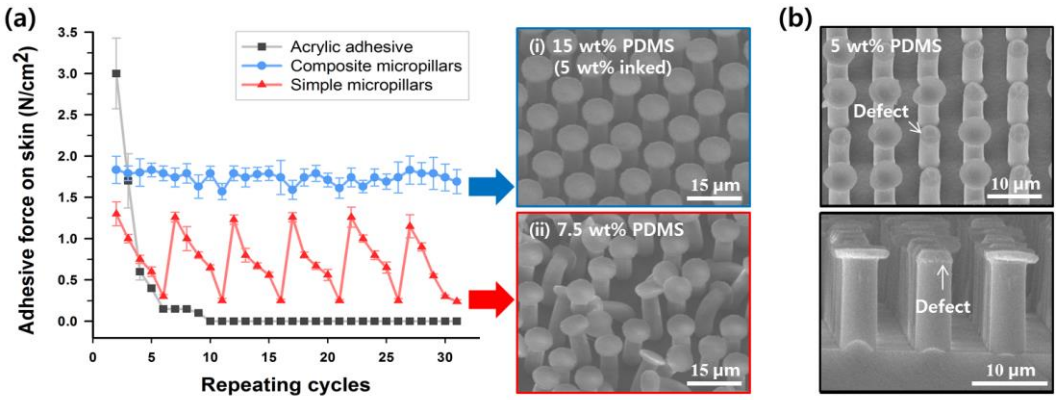

Figure 2-3. (a) Durability tests of composite micropillars with comparisons to homogeneous micropillars and commercially available acrylic medical patch. As shown, the adhesion was maintained at ~1.8 Ncm^{-2} over 30 repeating cycles of attachment and detachment for the composite micropillars. The stem region of composite micropillars is enforced with 15 wt% curing agent of PDMS, showing good physical integrity and uniformity (i). For the homogeneous micropillars, the adhesion is continuously deteriorated via structural collapses (ii). The results with low modulus PDMS (7.5 wt% curing agent) and acrylic adhesive are adapted from our previous report.[39] (b) SEM images of replicated low-modulus PDMS (5 wt% curing agent) micropillars, showing that the tip layer is easily torn-off in the demolding procedure.

To demonstrate utility as a fixation unit in the existing diagnostic devices, we integrated the current dry adhesive patch of 6 cm in diameter with a commercially available U-health monitoring device and measured electrocardiogram (ECG) for the time period of 48 hrs on two locations of a volunteer's skin (chest and wrist) in Figure 2-4a-b. For these tests, a commercially available unit of electrode and conductive gel was inserted in the center of a dry adhesive after making a hole as shown in Figure 2-4c. Then, several vital signals (e.g., T, U, P. and QRS) were recorded in real time. It turned out that the dry adhesive patch provided sufficient adhesion in most daily activities including walking, sitting, sleeping, etc. However, it was difficult to detect the signals under highly dynamic conditions such in running. Typically, the delamination initiated and propagated from the electrode site due to the electrode's own weight, which eventually resulted in a adhesion failure on the skin. During the entire testing period, no side effects such as allergy, redness, or skin damage were observed, suggesting that the dry adhesive skin patch presented here is biocompatible and reliable enough to monitor ECG for a long period of time.

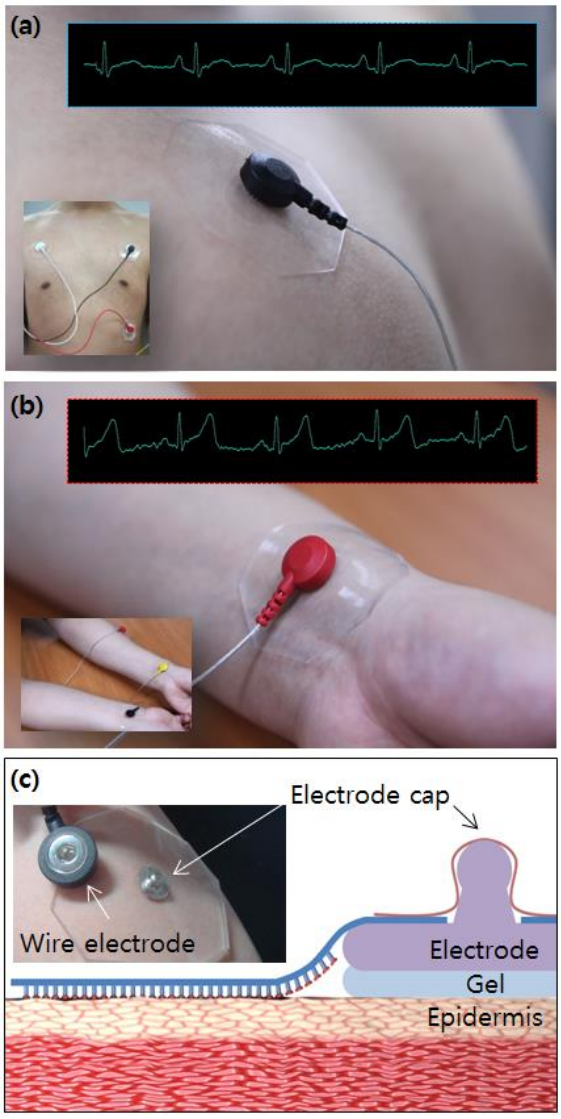

Figure 2-4. (a-b) Photographs showing the use of dry adhesive patch as a fixation unit in ECG module on the volunteer's chest (relatively flat surface) (a) and wrist (large curvature surface) (b). The inset images show the corresponding ECG signals from the volunteer's heart. (c) A schematic illustration of the inserted electrode along with an actual image on the skin (inset).

2-4. Summary

In summary, we have presented a simple method for fabricating an enhanced dry adhesive skin patch by utilizing modulus-tunable composite micropillars made of stiff and soft PDMS materials. The method consists of direct replica molding of rigid bottom micropillars (curing agent ~ 15%) and selective inking of soft tip layer (curing agent ~ 5%). Such monolithically integrated composite micropillars show a larger normal adhesion force up to ~1.8 Ncm-2 (maximum: ~2 Ncm-2) on the human skin as well as high durability (~30 cycles) without notable degradations. Using the composite micropillars electrocardiograms (ECGs) were successfully recorded in real time for the time period of 48 h with minimal side effects. This improved approach would shed light on more biocompatible, long-term skin-attachable devices in future U-health applications.

Chapter 3. Fabrication and analysis of enforced dry adhesives with core-shell micropillars

3-1. Introduction

Since the discovery of exquisite adhesion and locomotion capability of gecko lizards, the research on dry adhesives has passed the teenage years and is now faced with a next level of innovations in terms of new materials and designs.[59, 60] For the last decade, many research groups have introduced useful fabrication methods based on various top-down and bottom-up approaches; it is now possible to fabricate multiscale, hierarchical structures with controlled geometry.[41, 61, 62, 63, 64] In addition, significant advances have been made towards our understanding on the gecko's smart adhesion and locomotion mechanism as to why a multi-level, angled structure is advantageous over a single-level, vertical one.[47, 49, 65]

Despite these efforts and achievement, two main issues have not been explored to a large extent: robust adhesive materials and versatile attachment/detachment mechanism. For the latter, our group and others have introduced several stimulus-responsive reversible adhesion mechanisms based on wrinkling,[51] thermal cycle,[66, 67] and an external electric field.[68] Further

studies are required to implement these concepts in a more cheap and scalable manner. Regarding robust adhesive materials, there also has been notable accomplishment by using mechanically-enforced micro- or nanostructures. Examples include metal-coated nanopillars either on the top or stem region and Janus-faced nanopillars with polymer and metal sides.[69, 70] Such enforced nanopillars may ensure a long-term use of dry adhesive at the expense of relatively high costs for fabrication and difficulty of tuning pillar geometry.

In the field of dry adhesives, PDMS has been widely used for its excellent properties like simple prototyping and tuneable modulus. It is now well understood that when a replicated PDMS structure is too soft, the intrinsic adhesion would be high but it is difficult to prepare dense micro or nanopillars. Roughly, a moderately cured PDMS (Sylgard 184, curing agent =10 wt%) pillar array becomes hardly replicated from an original master for pillars of <400 nm diameter with an aspect ratio (AR) larger than unity. On the contrary, if a PDMS is too rigid (e.g., hard-PDMS or a PDMS with curing agent > 15 wt%), densely populated micro- or nanopillars could be produced at the expense of reduced intrinsic adhesion strength. These observations suggest the possible existence of an optimal modulus of dry adhesive material to ensure sufficient adhesion strength without causing a large degree of surface contamination or structural collapse.[71]

Mushroom-like micropillars have been proposed as an efficient shape for a structured dry adhesive. In this case, a number of theoretical and experimental

works have demonstrated that high-AR polymeric structures are susceptible to collapse in the form of pillar-to-pillar interactions (lateral collapse or mating) or pillar-to-substrate interactions (ground collapse or clumping).[72] Generally, adhesion force dominates over gravity or other forces at (sub)micrometer scale,[54] such that the merged pillars would not be restored against such lateral or ground collapses. In particular, together with some elongation and breakage the clumping of pillars usually occurs when replicated from the master. Furthermore, they are easily paired with strong van der Waals or electrostatic interactions, forming a multi-body cluster with repeated uses,[43, 73] mainly due to large surface areas between mushroom-shaped pillars. To overcome these limitations, many strategies have been suggested for better durability, including the use of a high modulus material,[55] deposition of a rigid film,[69, 74] and thin film terminated pillar arrays.[75, 76] Nonetheless, the post collapsing of mushroom-shaped micropillars still poses a great challenge to practical and widespread uses of dry adhesive materials.

3-2. Experimental

Molding Process of Mushroom-like PDMS and PUA Micropillars. The SOI wafer with microholes (diameter = 5 μm, height = 15 μm, AR = 3 and pillar density = 1.0 × 106 cm2) was prepared by photolithography and subsequent reactive ion etching (RIE). The SOI wafer (p-type, 100) had a 300-nm-thick oxide layer on a 500-μm-thick silicon layer. Then, a 15-μm-thick top silicon layer was formed over the oxide layer. The patterned wafers were treated with a fluorinated-self-assembled monolayer (SAM) solution ((tridecafluoro- 1,1,2,2-tetrahydrooctyl)-trichlorosilane: FOTCS, Gelest Corp.) diluted to 0.03 M in anhydrous heptane (Samchon Corp. Korea) in an Ar chamber. The surface-treated masters were annealed at 120 ℃ for 20 min. To make PUA micropillars, drops (~ 100 μl) of UV-curable PUA prepolymers (MINS 301 RM, elastic modulus: 19.8 MPa, Minuta Tech, Korea) were dispensed onto the master, and a flexible polyethylene terephthalate (PET) film (thickness ~50 μm) was slightly pressed against the liquid drop to be used as a supporting backplane. After preparing a polymer replica by UV exposure (λ = 250 ~ 400 nm, dose = 300 mJ/cm2) and mold removal, the PUA replica was additionally exposed to UV for several hours for complete curing. Details on synthesis and characterization of the PUA polymers can be found elsewhere.[77] For PDMS micropillars, a 10:1 mixture of the PDMS prepolymer (Sylgard 184A) and the curing agent (Sylgard 184B) was

poured onto the master. Subsequently, the master was placed in a vacuum chamber to degas for 30 min in several decades of mTorr. After degassing, it was put into a convection oven and cured at 70 ℃ for 2 hrs. Lastly, the cured PDMS replica was carefully detached from the master to avoid possible fracture of the bulged tips.

Fabrication of core-shell micropillars. The mushroom-shaped PUA micropillars (height = 15 μm, diameter = 5 μm, spatula diameter = 7 μm) were prepared as described above. The as-formed PUA micropillars were treated with oxygen plasma treatment for 60 s (60 W, PDC-42G, Harrick Scientific, Ossining, YN) to increase surface free energy. After that, the micropillars were inversely placed (pillars facing down) on a PDMS spin-coated wafer substrate (20 wt% PDMS in toluene, 6000 rpm, 60 s) to create a uniform skin layer of PDMS. Subsequently, the coated PUA micropillars were inversely placed on a Teflon-coated substrate and cured in a convection oven at 70 ℃ for 2 hrs. After curing, the PDMS-coated PUA micropillars were carefully removed from the substrate.

Normal and Shear Adhesion Tests. The macroscopic normal and shear adhesion forces were evaluated by a custom-built equipment at a relative humidity of 50% (Supporting information Figure S3). An adhesive patch was attached to a glass surface under a preload of ~0.1 N/cm2, and an in-plane strain was applied with strict alignment until a separation occurred. For comparison, the adhesion forces of PDMS and PUA micropillars were also measured in the same way.

3-3. Results and Discussion

To find an optimal geometry or modulus of a structured dry adhesive, we present here an alternative approach of utilizing core-shell type micropillars that are composed of relatively rigid backbone micropillars of PUA (Young's modulus ~19.8 MPa) and a thin shell layer of PDMS (Young's modulus ~1.8 MPa). The PUA pillars are simply replicated from a patterned silicon-on-insulator (SOI) master having an array of holes (diameter =5 μm, height =15 μm, AR =3 and pillar density =1.0 × 106 cm2), whose geometry is the same used in our previous study.[71] Subsequently, a thin PDMS layer is uniformly coated by placing the replicated PUA structure onto a spin-coated, diluted PDMS prepolymer. Then, capillarity forces the viscous PDMS prepolymer to rises into the cavity, thereby forming a uniformly-coated shell of PDMS layer to the thickness of 100 to 200 nm. These composite micropillars display enhanced durability over 100 cycles of attachment and detachment as well as fairly high normal and shear adhesion forces that are similar to or even larger than those of simple replicated PDMS micropillars.

A schematic illustration for fabricating PDMS skin-coated PUA micropillars is shown in Figure 3-1(a). Here, a SOI wafer was used to replicate mushroom-like micropillars using a UV-curable PUA material after a series of processes including photolithography, vertical anisotropic etching and slight

lateral overetching. The detailed fabrication method was reported earlier.[51, 71] After replication, the PUA micropillars with bulged tips (height = 15 μm, diameter = 5 μm, spatula diameter = 7 μm) were formed over a large area of 3 × 3 cm2 with good physical integrity and minimal defects (Fig ure 3-2- 1(b)). Next, the as-formed PUA pillars were surface treated by O2 plasma to increase the surface free energy. This step turned out to be important to tightly bond the PDMS shell layer to the PUA micropillars; otherwise some local delaminations were detected over repeated uses (see Supplementary Figure S1). In order to coat a PDMS shell layer, the O2 plasma treated PUA micropillars were inversely placed for few seconds onto a spin-coated PDMS layer on silicon wafer, resulting in uniform wetting of the PDMS on the entire micropillars by capillary rise. Finally, the replica was cured by inversely placing onto a Teflon-coated, low surface-energy substrate to flatten and cleanly release the mushroom-like, core-shell micropillars.

Fig ure 3-2- 1(c) shows an SEM image of PDMS-coated PUA micropillars, in which a well-defined meniscus is shown between the neighbouring micropillars. According to the TEM image in the inset, the thickness of the shell layer ranged between 100 and 200 nm, with the maximum thickness being observed on the top surface where a direct contact had been made between the patterned PUA replica and the spin-coated PDMS layer.

Using the fabricated composite pillar arrays, normal and shear adhesion

forces were measured against a flat smooth glass surface under a preload of ~0.1 N/cm2 using custom-built equipment (see Supplementary Figure S2). As shown in Fig ure 3-2-2(a), the core-shell type micropillars displayed large normal (~11.4 N/cm2) and shear (~15.3 N/cm2) adhesion forces as compared to PUA and homogeneous PDMS micropillars with the same curing agent.

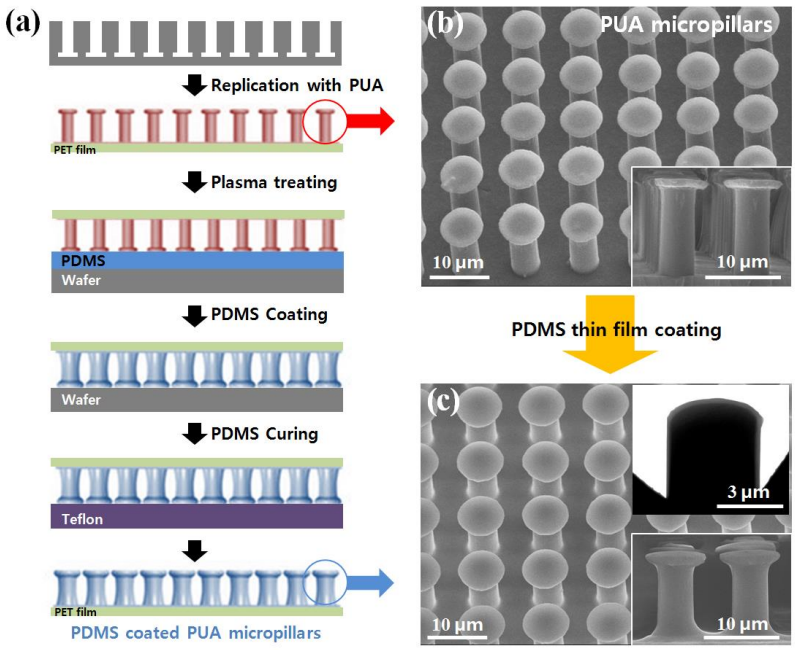

Figure 3-1. (a) Schematic illustration of fabricating PDMS-coated PUA micropillars (core-shell micropillars) by replica molding and thin film wetting. (b) An SEM image of the as-formed PUA micropillars along with a cross-sectional view. (c) An SEM image of the PDMS-coated PUA micropillars along with a cross-sectional view. The inset shows a cross-sectional TEM image, indicating that the thickness of PDMS skin is 100 to 200 nm.

Notably, the measured forces are slightly larger than those of the homogeneous PDMS micropillars, which seems to be associated with less structural collapses over time as described before. Durability tests in Figure 3-2(b) also demonstrated that the core-shell type micropillars were more mechanically robust than the PDMS pillars as evidenced by negligible degradations over 100 repeated cycles of attachment and detachment. In sharp contrast, the PDMS pillars alone showed a substantial drop of the adhesion from the initial value of ~15 N/cm2 to ~5 N/cm2 after ~10 uses.

To gain an understanding on the generation of post collapse between neighbouring pillars, a simple beam deflection model is used here, in which the displacement V of micropillars is given by (detailed derivation is provided in Supporting Information along with Figure S3)

$$V = \frac{PL^3}{12EI} \tag{1}$$

where E is the Young's modulus, I is the moment of inertia (EI: flexural rigidity), P is the pulling force (theoretical shear adhesion force per single hair), and L is the height of micropillar.[78]

For simplicity, the core-shell type micropillar presented here can be viewed as a composite microstructure with a rigid core surrounded by a soft skin layer. Consequently, an approximate core-shell composite model[79] is employed

to describe the size-dependent elastic properties in a linear combination, yielding

$$EI = E_{PUA} I_{PUA} + E_{PDMS} I_{PDMS} \tag{2}$$

where EI is the effective flexural rigidity of the composite micropillars that is responsible for transverse deformation, E_{PUA} and E_{PDMS} are the Young's moduli of the PUA and PDMS materials, respectively, and I_{PUA} and I_{PDMS} are the moments of inertia for the cross section of PUA core and the PDMS shell, respectively.

For the geometric layouts shown in **Figure 3-3(a-c)**, one can obtain the maximum displacement of PDMS, PUA, and composite PUA/PDMS micropillars when detached from an adhered surface using the beam deflection model and flexural rigidity mentioned above. As seen from **Figure 3-3(d)**, the displacement of micropillars is given as a function P for the three cases where the largest displacement is expected for PDMS due to its lowest modulus. As a result, the displacement of PDMS micropillars would become larger than the distance between neighbouring pillars, which in turn gives rise to self-mating or lateral collapse of micropillars (**Figure 3-3(a)**). In contrast, PUA and core-shell micropillars rarely contact each other for a given displacement field, leading to elevated stability over time (**Figure 3-3(b, c)**).

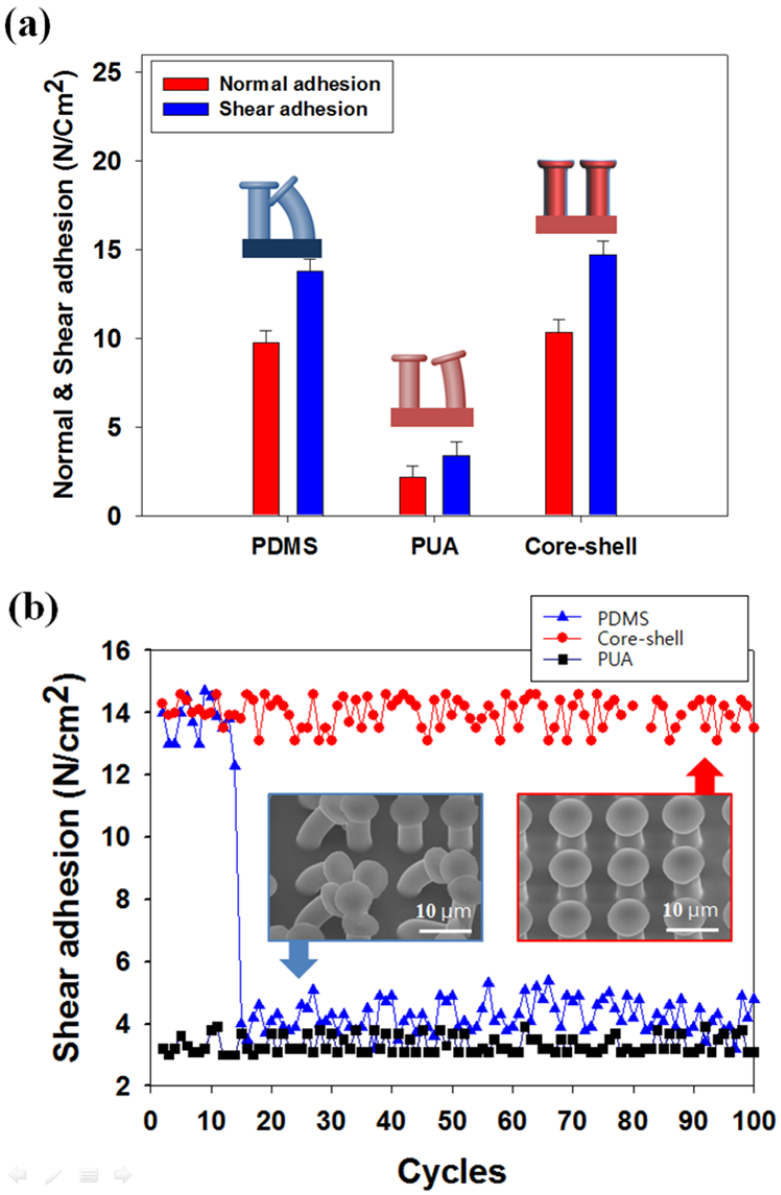

Figure 3-2. (a-b) Measurement of (a) macroscopic normal and shear adhesion forces and (b) durability over 100 repeating cycles of attachment and detachment for PDMs, PUA, and core-shell micropillars. Tilted SEM images in the inset of (b) show the core-shell structures are stable over repeated uses.

The mechanical stability of core-shell micropillars can be determined by the competition between the elastic bending and van der Waals (VdW) forces, which account for the restoring and adhering forces exerted on the micropillars, respectively. **Figure 3-4(a)** shows a schematic of the self-mating micropillars with three different cases (case 1: minimum contact: case 2: intermediate contact, and case 3: maximum contact). For each case, the adhesion force between pillars, F_{vdw}, can be written as:[80]

$$F_{vdw} = \frac{Aa}{6\pi D^3} \tag{3}$$

where A is the Hamaker constant of PDMS material (4.5×10^{-20} J),[81] D is the distance (1.65 nm) of the paired pillars and a is the contact area. Therefore, the VdW force increases with the increase of a, indicating that the force increases from the case 1 to case 3. The corresponding recovering force (P) can be estimated based on the displacement of each case, e.g., d_1 = 2.5, and d_3 =7.5 μm, respectively, by using same beam deflection model. Here, we assumed that the maximum contact area and bending displacement of each pillar would not be changed for multiple (>3) self-mated pillars.

The comparison of the two competing forces is shown in **Figure 3-4(b)**. As shown in the graph, the recovering forces of PDMS micropillars are lower than the VdW forces in all the three cases. As a result, once the PDMS micropillars are

mated with neighbouring pillars, they would not return to their original position, causing continuous reduction of normal and shear adhesion forces over time as shown in **Figure 3-2**. In contrast, the core-shell micropillars possess higher restoring forces than VdW forces in the three cases; one can expect enhanced stability even with high-density micropillars presented here.

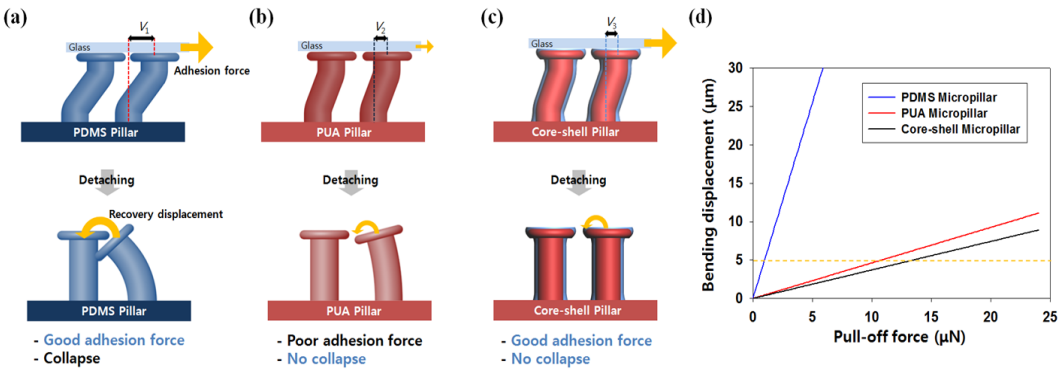

Figure 3-3. (a-c) Schematic illustrations for the displacement of (a) PDMS, (b) PUA, and (c) core-shell micropillars. As shown, the micropillars are distorted in a lateral direction when an external shear force is applied. (d) Plots of bending displacement as a function of pull-off force for the three cases. The insert yellow line indicates the distance between neighbouring pillars used in our experiment.

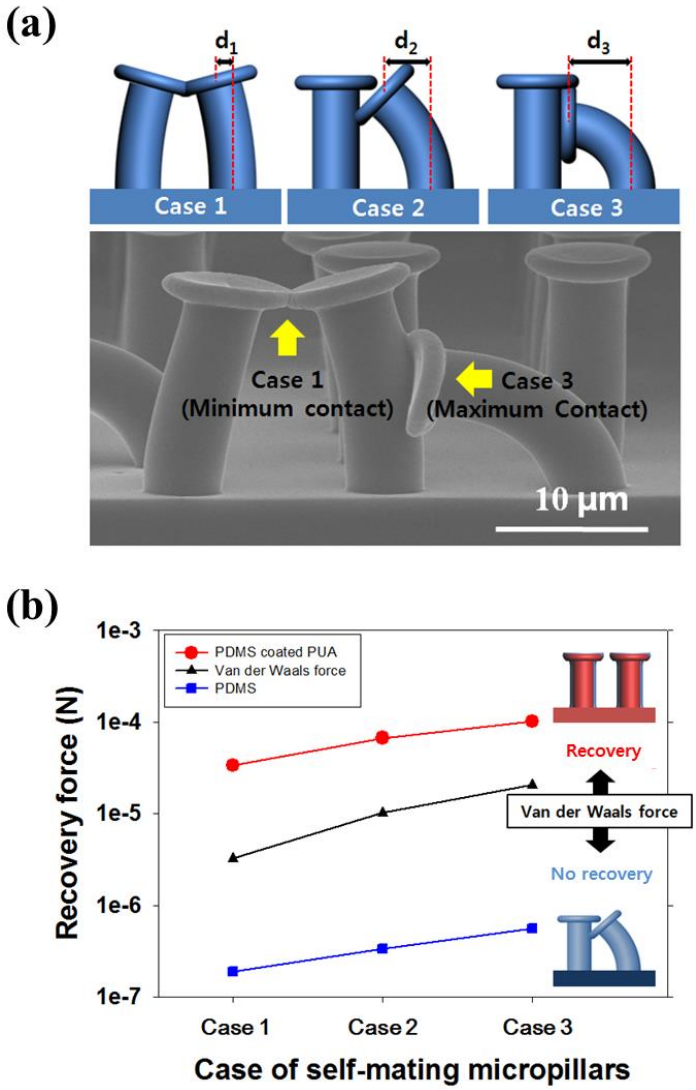

Figure 3-4. (a) The three cases of self-mating PDMS micropillars with minimum (Case 1), intermediate (Case 2), and maximum contact areas (Case 3). (b) Comparisons of the predicted recovery and van der Waals forces with the three cases. In the case of PDMS micropillars, the recovery forces in all cases are smaller than the adhesion forces between neighbouring pillars.

3-4. Supplemental

Detailed derivation of the displacement *V* of micropillars using beam deflection theory

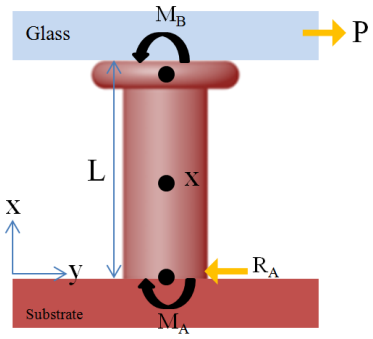

Boundary condition:

$$\sum F = 0 \quad (\because R_A = P)$$

$$\sum M = 0 \quad (\because -M_A - PL + M_B = 0)$$

Figure S3. Geometric description of micropillar.

The above expression for the bending moment can be expressed into a second-order differential equation, yielding

$$\frac{d^2v}{dx^2} = \frac{M_{(x)}}{EI} \tag{S1}$$

$$EI\frac{d^2v}{dx^2} = M_{(x)} = M_a + R_a x \tag{S2}$$

$$EI\frac{dv}{dx} = M_a x + \frac{1}{2}R_A x^2 + C_1 \tag{S3}$$

$$EIv = \frac{1}{2}M_a x^2 + \frac{1}{6}R_A x^3 + C_1 + C_2 \tag{S4}$$

$$C_1 = 0, \because x = 0, \frac{dv}{dx} = 0 \tag{S5}$$

$$C_2 = 0, \because x = 0, v = 0 \tag{S6}$$

Then, the deflection ν at the tip is given by

$$v = \frac{1}{EI}\left(\frac{1}{2}M_a x^2 + \frac{1}{6}R_A x^3\right) \tag{S7}$$

$$v_{(x=L)} = \frac{1}{EI}\left(\frac{1}{2}M_a L^2 + \frac{1}{6}R_A L^3\right) \tag{S8}$$

$$v_{(x=L)} = \frac{1}{EI}\left(-\frac{1}{4}PL^3 + \frac{1}{6}P L^3\right) \quad \because M_a = -\frac{P}{2}L, R_A = P \tag{S9}$$

$$\mathrm{A}\, v_{(x=L)} = \frac{1}{EI}\left(-\frac{1}{12}P L^3\right) = -\frac{PL^3}{12EI} \tag{S10}$$

3-5. Summary

In conclusion, we have presented a simple method to fabricate a robust dry adhesive by utilizing core-shell micropillars made of rigid PUA backbone and soft PDMS skin layer. The method consists of well-established replica molding and capillarity-assisted uniform wetting, allowing for a scalable, low-expertise route to the preparation of structured dry adhesives. The composite micropillars showed relatively strong normal (~11.4 N/cm^2) and shear adhesion (~15.3 N/cm^2) forces with enhanced durability over 100 repeating cycles of attachment and detachment. Also, a simple beam deflection model was used to analyze the stability of the core-shell micropillars, demonstrating that the enhanced restoring forces from the PUA core overwhelms the VdW forces, leading to less chances of lateral collapse, whereas the soft PUA skin layer elevates the adhesion strength. The current strategy would be useful to create robust dry adhesive materials with precise tip geometry and enhanced mechanical stability.

Chapter 4. Instantly switchable adhesion of bridged fibrillar adhesive via gecko-inspired detachment mechanism and its application to a transportation system

---

4-1. Introduction

It has been more than a decade since the mystery of micro/nanofibrillar structures on the feet of climbing creatures was discovered, inspiring a wide range of research areas from biomimetic robotics to medical bandage through artificial fibrillar adhesives.[60, 63, 82] Fibrillar adhesives can provide superior adhesion properties to chemical-based conventional ones because the adhesion force mainly stems from intermolecular interactions between the end of fibrils and the contact surface, exerting attractive van der Waals force for universal adhesion.[5, 30, 83] Furthermore, they allow for reversible and repeatable adhesion on rough surfaces as can be seen in the locomotion of gecko lizards. One striking feature of fibrillar adhesives is that they can preserve the contact surface without leaving behind chemical residues or particles even after numerous cycles of attachment and detachment.[61]

Motivated by such fouling-free adhesive properties, researchers have been trying to exploit the switchable adhesion of fibrillar adhesives in various

applications such as wall-climbing robots, clean transportation, particle gripping, and medical patch. For example, our group demonstrated a clean transportation system for precision industry in which a gecko-inspired fibrillar adhesive was installed to convey thin, large-area glass panels for assembly process.[61] Also, other groups utilized fibrillar structures as a tool for micromanipulation of micro-sized parts by taking advantages of adhesion hysteresis between on and off states.[84] In parallel, fibrillar structures were used as a tissue adhesive for wound healing[85] and a fixation unit for medical skin patches to monitor life signal.[71, 86] For robotic applications, fibrillar adhesives were integrated with robots to realize wall-climbing function[87], and some biomedical microrobots were suitably operated under wet or flow conditions *in vivo* (*e.g.* blood vessel, intestine, or muscle tissue).[88]

Of the various applications mentioned above, active transport with an advanced adhesion mechanism is potentially of great benefit in views of its strong industrial needs in precision industry (semiconductor, display, solar cells, *etc.*) and impacts in other related areas involving micromanipulation. To date, active or passive control of normal/shear adhesion has been achieved with various approaches by utilizing switchable adhesion with thermally- or magnetically-responsive materials[66, 89], wrinkling surface[51, 90], modifying tips of fibrils[64, 75, 86, 91, 92], and designing anisotropic tip shape[93]. The widespread use of these methods, however, has been limited partly due to complex fabrication steps,

difficulty of implementing adhesion switching, or low adhesion hysteresis. A recent study by Crosby and co-workers suggested that a high shear loading capacity of ~29.5 N/cm^2 could be achieved by using a simple pattern-less fabric composite even without a specific contacting geometry such as fibrils.[94] In addition to our initial demonstration with hierarchically angled nanopillars[61], most of the previous reports have focused on the strong shear adhesion force with implications to switchable adhesion; however, a dry adhesive with switchable adhesion capability together with strong normal adhesion has been rarely reported. Therefore, it is needed to identify and further expand the role of fibrillar structures in active, dynamic control of dry adhesion for more practical applications.

To tackle such a challenge, we introduce here the use of fibrillar adhesives in the form of bridged micropillars with a uniform capping membrane for strong normal attachment and easy detachment without involving complex dynamic mechanisms or specific stimulus-responsive materials. We utilized a large adhesion contrast between the two detaching methods of pulling and peeling for “on-state” and “off- state”, respectively, to enable instantly switchable adhesion. The pulling mode is engaged by placing the capping membrane to a target surface, exerting a large lifting force by trapping internal cracks and hampering crack propagation. The peeling mode, on the other hand, is activated by deliberately generating a crack at one end of the capping membrane, thereby propagating the crack to the other direction rapidly due to its connected,

monolithic architecture. In particular, the peeling mode is inspired from the climbing behaviour of a gecko lizard – it curls its toes to release its foot from the surface. By combining the fibrillar adhesive with an automated transportation system, we could enable an active transport of a hanging mass of stacked glass slides over 1000 cycles of attachment and detachment without appreciable surface contamination or deterioration of adhesion capability.

4-2. Experimental

Preparation of master mould. A silicon-on-insulator (SOI) master was prepared as a mould for replicating mushroom-shaped straight micropillars by conventional photolithography and dry etching (Supporting information, Figure. S3). The SOI wafer (Mico MST Ltd., Korea) consisted of 3 layers: a p-type (100) bare Si wafer (resistivity: 1 ~ 30 Ω) at the bottom, a SiO2 etch-stop layer with the thickness of 500 nm in the middle, and a polysilicon layer with the thickness of 60 μm on the top. Plasma-enhanced chemical vapour deposition process was performed to deposit a SiO2 layer of 800 nm on the top of the SOI wafer. Anisotropic dry etching in the vertical direction was carried out to pattern holes of 30 μm in diameter until the complete exposure of the etch-stop layer. Subsequent over-etching in the lateral direction resulted in the negative patterns of mushroom-shaped micropillars on the SOI wafer. The patterned mould was treated with a fluorinated self-assembly-monolayer solution ((tridecafluoro-1,1,2,2-tetrahydrooctyl)-trichlorosilane: FOTCS, Gelest Inc., USA) diluted in anhydrous heptane (Samchon Co., Korea), followed by annealing process at 120 ℃ for 20 min.

Fabrication of bridged micropillars. Straight PDMS (Sylgard 184, Dow Corning, USA) micropillars were replicated from the SOI master with 15 wt% curing agent. The mixture was filled into the master mold, left in a vacuum

chamber for 30 min, thermally cured at 75 ℃ for 2 h, and the cured one was carefully removed from the master mold. A thin film of low modulus PDMS (5 wt% curing agent) was prepared by spin-coating a diluted PDMS solution in hexane at 6000 rpm. The as-prepared straight micropillars were carefully placed onto the film and left undisturbed for a few seconds, so that a slight amount of soft liquid PDMS was transferred to the heads of the micropillars.[95] Then, the inked micropillars were inversely placed onto a Teflon-coated low-surface-energy substrate without applying a pressure, resulting in the bridging of entire micropillars covered by a thin PDMS capping membrane of ~800 nm thickness (Supporting information, Figure. S4). Finally, the sample was left in a hot oven of 75 ℃ for more than 12 h and after curing the bridged micropillars were detached clearly from the Teflon substrate.

Normal adhesion tests by a custom-built measurement system. A custom-built adhesion measurement system was used to measure normal adhesion force of the bridged micropillars on a reference surface (Supporting information, Figure. S1). The system is composed of two motorized load cells and a finely flat stage. Each of the load cells (UMMA-K20, Dacell, Korea) was used for measuring adhesion force in x (lateral) and z (vertical) directions, respectively, and the load cell in z direction enabled exerting a preload on the loaded adhesive in a controlled manner in Newton (N). The flat stage provided a space allowing horizontal contact to a reference surface. As for a reference surface, a sheet of flat

glass slide was positioned on the stage and the sample with bridged micropillars of 1 × 1 cm2 was loaded on the load cell in z direction. A preload was applied in the normal direction to make the adhesive and the reference surface fully contact each other. The data for normal load was obtained in N and saved every 0.01 second until a complete detachment occurred. Under the pulling mode, both sides of a sample were firmly fixed on the motorized stage to distribute the load evenly on the sample during the measurement. Under the peeling mode, only single side of a sample was fixed on the stage with an asymmetric load distribution while a preload was uniformly applied on the sample.

4-3. Results and Discussion

In order to enable an active transport in a fast, reversible fashion, one needs to have two seemingly contradicting attributes: strong adhesion and easy detachment. Our key idea here is that the bridged micropillars are highly adhesive on flat surfaces at the expense of relatively small adhesion capability on rough surfaces, while they can be readily separated from the surface by rapid crack propagation. **Figure. 1** displays our strategy with a custom-built adhesion measurement system used in the study (see the experimental section and the supporting information, **Figure. S1**). Here, we define two different detaching methods that can be termed as “pulling” mode and “peeling” mode, respectively. In the pulling mode, the two edge parts of the adhesive are firmly fixed on the motorized stage, so that the load can be evenly distributed on the patterned surface, resulting in a large macroscopic normal adhesion force. In contrast, the peeling mode is designed to induce crack propagation at one edge deliberately, which is similar to the climbing mechanism of gecko lizards by curling their toes when they take a step while climbing. Specifically, only one of the two edges is fixed on the motorized stage in this mode; the adhesive fails to maintain its adherence on the surface due to the rapid crack propagation. As a consequence, in the peeling mode, the macroscopic normal adhesion force becomes minimized, facilitating

easy detachment within a very short period of time.

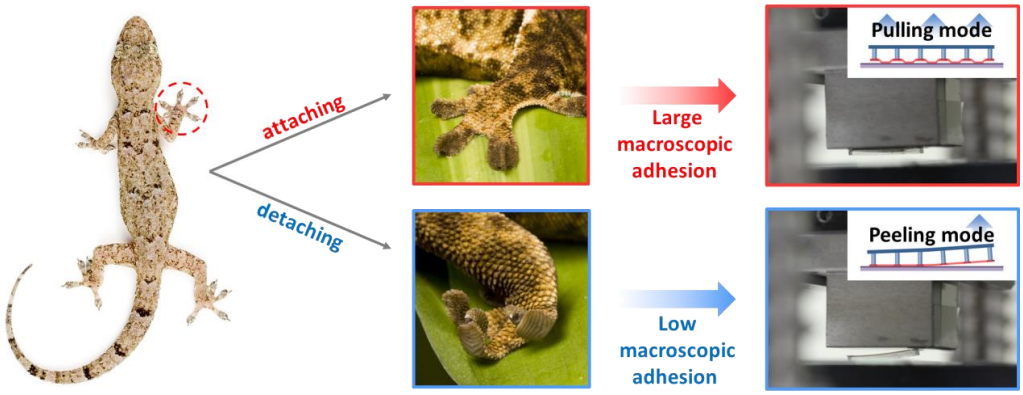

Figure. 4-1 When climbing, a gecko lizard controls macroscopic adhesion force of its foot by changing the way of taking steps. In order to cling, it attaches its foot with stretched toes as much as possible to maximize macroscopic adhesion force exerted by the fibrils on its foot. On the other hand, it curls its toes outward when taking another step to facilitate the detachment from the end of the toe. The detachment mechanism in our study is inspired by such a selective detachment mechanism of the gecko's toes. Specifically, the "pulling" mode corresponds to the stretched toes for maximizing normal adhesion force, while the "peeling" mode mimics the curling toes, which leads to a sharp decrease in normal adhesion force.

A schematic description of fabrication process is shown in **Figure 4-2a**, in which the fabrication process was mainly composed of replicating straight micropillars (diameter = 30 μm, height = 60 μm) from a master mould with rigid PDMS (*15 wt%* curing agent) and transferring relatively soft PDMS (with *5 wt%* curing agent) precursor on the heads of the as-prepared micropillars to form a mesh-like membrane. It is noted that the elastic modulus of the material was tuned by applying different amount of curing agent for the micropillars as well as for the membrane[44], so that the structural integrity of bridged micropillars was optimized along with the exploitation of viscoelastic and dissipative characteristic of the membrane on a flat surface.[92] It is noted that a thin membrane can be formed spontaneously in the course of liquid bridging without a complicated process such as the preparation of an additional substrate with a sacrificial layer or etching process to transfer the as-prepared membrane.[75, 96] Fig ure 3-3-2b displays the liquid bridging by spontaneous interconnections of low viscosity PDMS precursor by inversely placing the fibrillar structures on an inert surface, which was a Teflon-coated substrate in this case. For visualization, Rhodamine B (Sigma-Aldrich Co., USA) was mixed in the diluted soft PDMS and the transfer to the micropillar heads was observed under an inverted fluorescence microscope. As shown, the micropillars were bridged in a grid, square pattern such that the neighbouring pillars were merged to form a mesh-like thin (~800 nm thickness) membrane, while the micropillars that were diagonally faced were rarely

connected. It seems that the membrane gets thinner as the solvent evaporates, leaving behind a hole in the centre due to the coffee-ring effect.[97] This can be easily seen from the fluorescent images in which the red signal at the edge of fibrillar heads is much stronger than that of the central region of the heads.

It is worthwhile noting that the solid fraction of PDMS precursor plays a crucial role in forming a well-defined capping membrane with bridged pillars as shown in **Figure 4-3**. Here, we prepared three different solutions in n-hexane with different volumetric mixing ratios (PDMS: solvent) of 1:1 (a), 1:3 (b), and 1:10 (c), respectively. It turned out that the excessive amount of the PDMS precursor was squeezed out of the assembly, forming a non-uniform membrane in the 1:1 mixing ratio. Also, the 1:10 mixing ratio was not successful with many unconnected or partly connected micropillars. Based on our experimental conditions used here (diameter, type of packing, distance between micropillars, *etc.*), the 1:3 mixing ratio was optimal, allowing for a uniform capping membrane with bridged micropillars over a large area (1.0×1.0 cm^2)

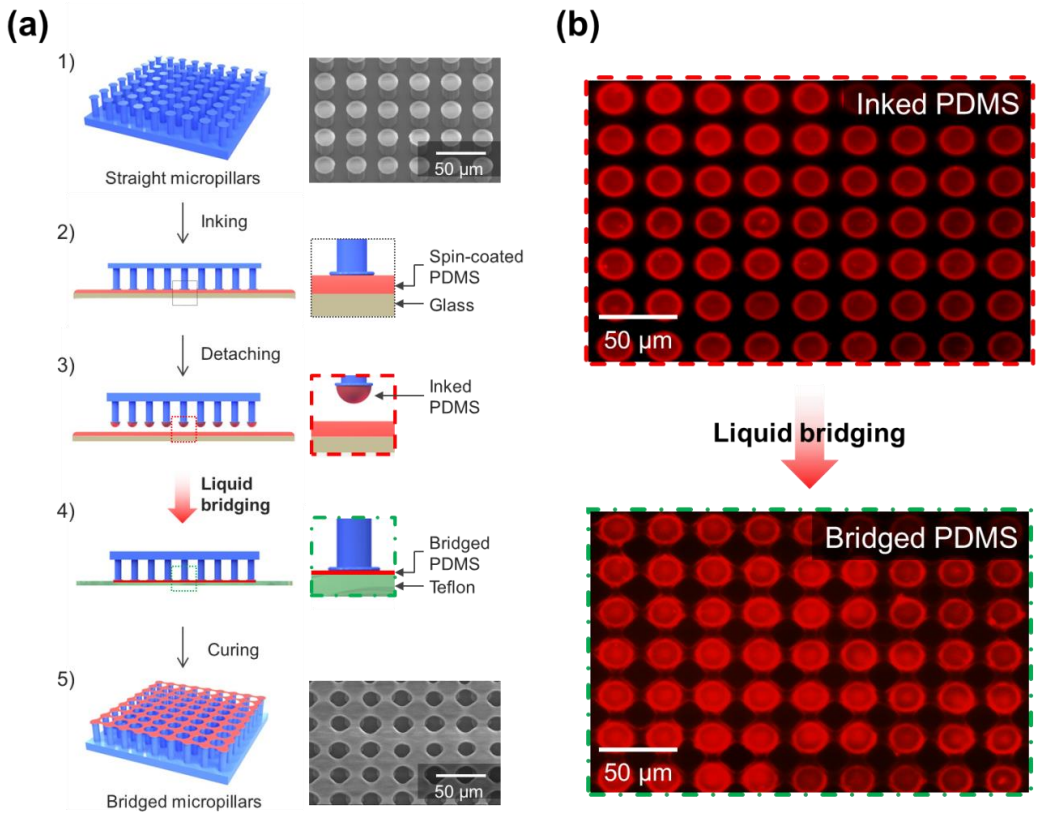

Figure. 4-2 (a) Schematic illustration of fabricating bridged micropillars along with the corresponding scanning electron microscopy (SEM) images before and after the inking process. (b) Fluorescent images of inked micropillars with a low-viscosity PDMS (step 3) and bridged micropillars after squeezing the PDMS liquid (step 4).

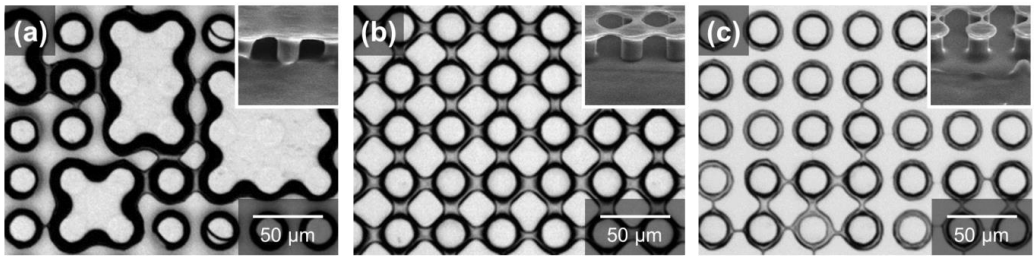

Figure. 4-3 Optical images showing that the fidelity of bridged micropillars depends on the mixing ratio of spin-coated PDMS in n-hexane, (a) 1:1, (b) 1:3, and (c) 1:10. The inset SEM images display a side-view of each case.

Figure. 4-4 shows the measurement of macroscopic normal adhesion forces of two different samples (1.0 × 1.0 cm^2): bridged micropillars and straight micropillars. The loads in normal direction were recorded by a load cell in N and the data were saved every 0.01 second. In the pulling mode (**Figure 4-4a**), the sample fixed on the moving part was brought into contact with a flat glass surface under the preload of 30.0 N cm^{-2} and lifted by the motorized stage at the speed of 0.2 mm s^{-2}. The straight micropillars exhibited an adhesion force of ~10.3 N cm^{-2} within 0.04 sec, which is similar to our earlier observations as well as those from other groups.[51, 63] Strikingly, the maximum normal adhesion force of bridged micropillars was enhanced to ~29.6 N cm^{-2} within 0.05 sec which is quite comparable to the shear adhesion capacity of a carbon fibre fabric composite reported recently (~29.5 N cm^{-2}).[94] The normal adhesion force would be changed for different rate of detachment ("rate-dependent adhesion") due to viscoelastic nature of the membrane.[96, 98] Another notable feature is that the time it takes to separate the adhesive pad was much reduced for the bridged pillars (~0.05 sec) as compared to the straight pillars (~0.15 sec). This suggests that the individual pillars are gradually losing contacts in a cascade fashion for the straight micropillars[29], whereas the detachment is fast and instantaneous in the case of the bridged pillars.

In **Figure 4-4b**, the time-dependent normal load was measured in the peeling mode in the vertical direction after the two different samples were

attached under a preload of 30.0 N cm^{-2}. As can be seen from the **figure**, there is a sharp difference in the detachment behavior in terms of separation time. For the straight pillars, the force was rapidly reduced to ~2.0 N cm^{-2} within 1.5 sec because of the rapid crack propagation of the adhesive pad. It took another 1.5 sec to fully separate the adhesive pad. In contrast, the bridged pillars exhibited a similar force within 1.5 sec and then detached completely within 0.5 sec. This can be explained by the fact that single crack propagation is sufficient to induce a full detachment of bridged micropillars due to its connected, monolithic structural architecture.

To explain the observed adhesion behaviours with a simple theory, we simplify the network of bridged micropillars as micropillars with an extremely widen tip. According to a recent theoretical study, the detachment of micropillars from the surface can be explained by three different modes: i) crack propagation from the edge of micropillars, ii) propagation of defects in the inner contact region, and iii) de-cohesion due to a load larger than the theoretical contact strength that is related to van der Waals forces.[43] Here, the cracks start to propagate from the edge of micropillars once the interfacial tractive stress (σ) under a uniform normal load becomes larger than the critical value (σ_c) that is defined as

$$\sigma_c = \left(\frac{8E^* \Delta\gamma}{\pi R} \right)^{1/2} \quad (1)$$

where R is the radius of micropillar, $E^* = E / (1 - \mu^2)$ (E: Young's modulus

of the material, μ: Poisson's ratio), and $\Delta\gamma$ is the work of adhesion. [99] In general, an array of straight micropillars is prone to such a stress concentration at the edge that is associated with the geometric feature of micropillars, leading to detachment from the contact surface. [100] In the presence of an extremely widen tip, however, the stress singularity that mainly causes a local stress larger than σ_c could be removed, thereby suppressing significantly the crack initiation from the edge, one of the determining mode in detachment mentioned above.

In addition, even though an excess load nucleates interfacial voids in the inner contact region, the periodic structural nature of the bridged micropillars can hamper the propagation of such defects, as previously suggested by Glassmaker *et al*. with a simplified two-dimensional model of a fibrillar array with a flat terminal membrane on top.[75] To elaborate on this argument, let us consider the case in which an inner crack of the fibrillar array stays in a state of stable equilibrium, which can be expressed as

$$G_{\mathrm{L}} = W_{\mathrm{ad}}, \frac{dG_L}{dl} < 0 \tag{2}$$

where G_{L} is the rate of the local energy release for propagating the crack, *i.e.* elastic strain energy of the material per unit length that is released just nearby the edge of the crack, W_{ad} is the thermodynamic work of adhesion per unit area required to separate the interface, and l is the characteristic crack length. Here, the amount of released energy G_{L} can be assumed to fluctuate in a sinusoidal fashion

due to the periodic structure of bridged micropillars. Assuming that energy is supplied to the fibrillar array at a rate G_R per unit length, one can have the following expression by considering energy conservation:

$$G_L = G_R - \frac{dW_s}{dl} \tag{3}$$

where Ws is the stored elastic strain energy in the mesh-like membrane. From (3), one can notice that the supplied energy is either stored in the membrane (dWs / dl > 0) or discharged from the membrane in order to propagate the crack (dWs / dl < 0), which results in the sinusoidal fluctuation of GL as proposed above. This ultimately means that there occurs a difference of GR for advancing the crack depending on the position due to the existence of the membrane. Therefore, in order for the crack to continuously progress (GL ≥ Wad, dGL / dl ≥ 0), the crack must overcome the receding point where Ws is maximized at the expense of an extra amount of supplied energy. This is the reason for the phenomenon of crack trapping, which corresponds to our observation in **Figure 4-4a**. It demonstrates that macroscopic adhesion force significantly increased in the pulling mode as the detachment of the bridged micropillars was largely suppressed as compared to the straight micropillars. This also supports the result **in Figure 4-4b** in that the supplied energy per unit length in the peeling mode is much larger than the pulling mode, with the initial crack being in the state of unstable equilibrium at once. Such a behavior collectively brings about a rapid detachment with lower macroscopic adhesion.

Based on our experimental observations and theoretical consideration, we arrive at the conclusion that the fibrillar adhesive based on bridged micropillars is advantageous in terms of transportation devices thanks to its large normal adhesion force and fast detachment capability.

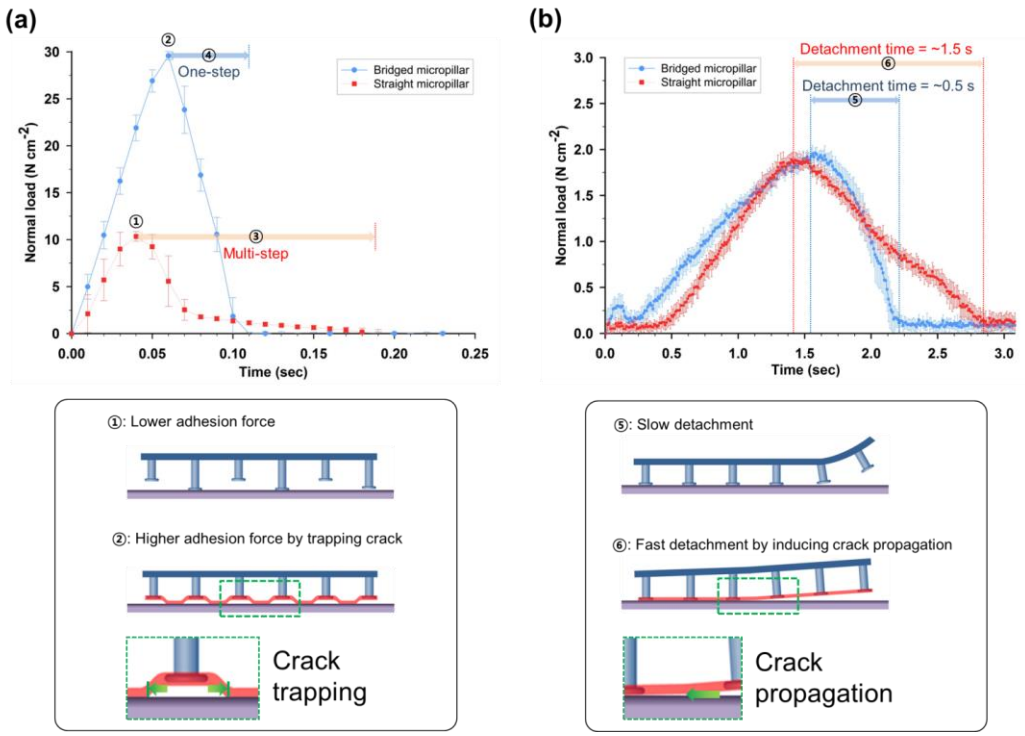

Figure. 4-4 Time-force plot of the bridged and straight micropillars when detached (a) in the pulling mode and (b) the peeling mode, respectively. Also shown are the corresponding illustrations for crack trapping or propagation at the bottom panel. In the pulling mode, the bridged micropillars show a larger maximum adhesion force of ~29.6 N cm^{-2} than that of the straight micropillars. Also, the former exhibits a more prompt detaching response that is associated with single crack propagation via the monolithic capping membrane. In the peeling mode, while the maximum normal load of each sample was decreased to ~2 N cm^{-2}, the bridged micropillars still show a quicker detaching response as compared to that of the straight micropillars.

We tested the robustness and durability of fabricated samples and the results are shown in **Figure 4-5**. The mechanical stability of bridged micropillars was verified in a quantitative fashion by applying controlled normal preload from 0.3 to 100 N cm^{-2} (~300 times as large as a typical preload[61]) with an increment of 5 N cm^{-2} in the pulling mode (**Figure 4-5a**). In contrast to the straight micropillars, the normal adhesion of bridged micropillars was elevated to ~29.6 N cm^{-2} with the increase of the preload until 30.0 N cm^{-2} and monotonically decreased thereafter. As can be seen in the inset SEM images of **Figure 4-5a**, the bridged pillars remained intact even after applying the preload of 100.0 N cm^{-2} over many cycles with increasing preloads, suggesting the enhanced durability of bridged micropillars.

The increase of normal adhesion from the preload of 0.3 N cm^{-2} to 30.0 N cm^{-2} is attributed to the increase of actual contact area. By inducing compressive contraction of micropillars, the bridge region between two micropillars is more likely to contact the surface, which eventually leads to the increase of the contact area or a higher adhesion force. The decrease of adhesion force after passing the maximum point may be caused by the displacement of micropillars due to the lateral deformation of the backfilm by Poisson effect under an excessive normal preload. When the backfilm is deformed under a high preload, the lateral deformation causes the distance between micropillars to increase slightly, which makes the membrane in an extended state. Once the preload is removed, the

deformed backfilm starts to recover its initial state, leading to local crack nucleation, which eventually facilitates local detachment of bridged micropillars. Also, **Figure 4-5b** displays the result of repeating 1000 cycles of attachment and detachment under the preload of 30.0 N, showing an excellent reusability of the bridged micropillars without deterioration in normal adhesion force.

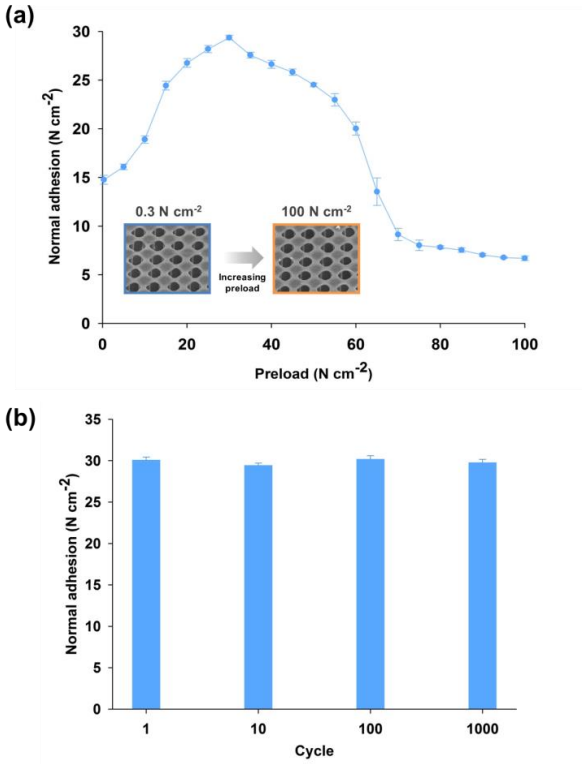

Figure. 4-5 (a) Change of macroscopic normal adhesion force of the bridged micropillars as a function of applied preload. The decrease of adhesion force after passing the maximum point may be associated with the elastic energy of the back film that is stored by the compressive deformation due to an excessive normal preload as illustrated in the middle panel in the order of 1 to 3 with the increase of the preload. The structures remain intact even after applying the preload of 100 N cm^{-2}, as seen from the inset SEM images. (b) Durability test of the bridged micropillars over 1000 cycles of attachment and detachment. Each sample was attached on a glass surface under the preload of 30 N cm^{-2} and detached in the pulling mode.

Figure 4-6 demonstrates a prototype automated transportation system based on the fibrillar adhesive. We could change macroscopic adhesion force by switching detachment methods between the pulling and peeling modes. Firstly, we fixed both ends of the sample of 1.0 cm × 1.0 cm on the motorized driving part so as to maximize the adhesion force (pulling mode, **Figure 4-6a**). A stack of three glass slides (0.5 kg) was used as a hanging mass. With the preload of 30.0 N cm^{-2}, the fibrillar adhesive was brought in intimate contact with the glass slides and lifted to transport them at a target location (on the same stage in this case) as shown in **Figure 4-6c** (corresponding to the step 3 in **Figure 4-6a**). After the glass slides were placed on the stage again, one of the two junctions of the sample was released from the driving part to switch from the pulling to the peeling mode, thereby propagating a crack from one end (peeling mode, **Figure 4-6b**). In this step, the glass slides were separated instantaneously and smoothly from the adhesive pad as shown in **Figure 4-6d** (corresponding to the step 6 in **Figure 4-6b**). **Figure 4-6e** represents the repeatability of this process as confirmed by carrying out the operation of the system between on and off states over 50 cycles in a serial manner. Furthermore, as seen from **Figure 4-6f**, we verified the direct advantage of using the bridged micropillars compared to the straight micropillars, through the simulation test of transporting an objective item with the system. The working conditions are given as follows: displacement = 3 mm in normal direction, lifting speed = 0.6 mm s^{-1}, lowering speed = 0.3 mm s^{-1}, preload = 30 N

cm^{-2} for 3 s. It is obvious that fibrillar adhesive with bridged micropillars can shorten the process time, which becomes more pronounced as the total number of conveyed items increases; we could save approximately 6 h to handle 10,000 glass slides with the same system by using the bridged micropillars. Taken together, the current scheme for automated transportation system based on the fibrillar adhesive is potentially useful for assembly process in the precision industry as well as micromanipulation (gripping, releasing, *etc.*) of objects in microdevices (Supporting information, **Figure. S2**).[101]

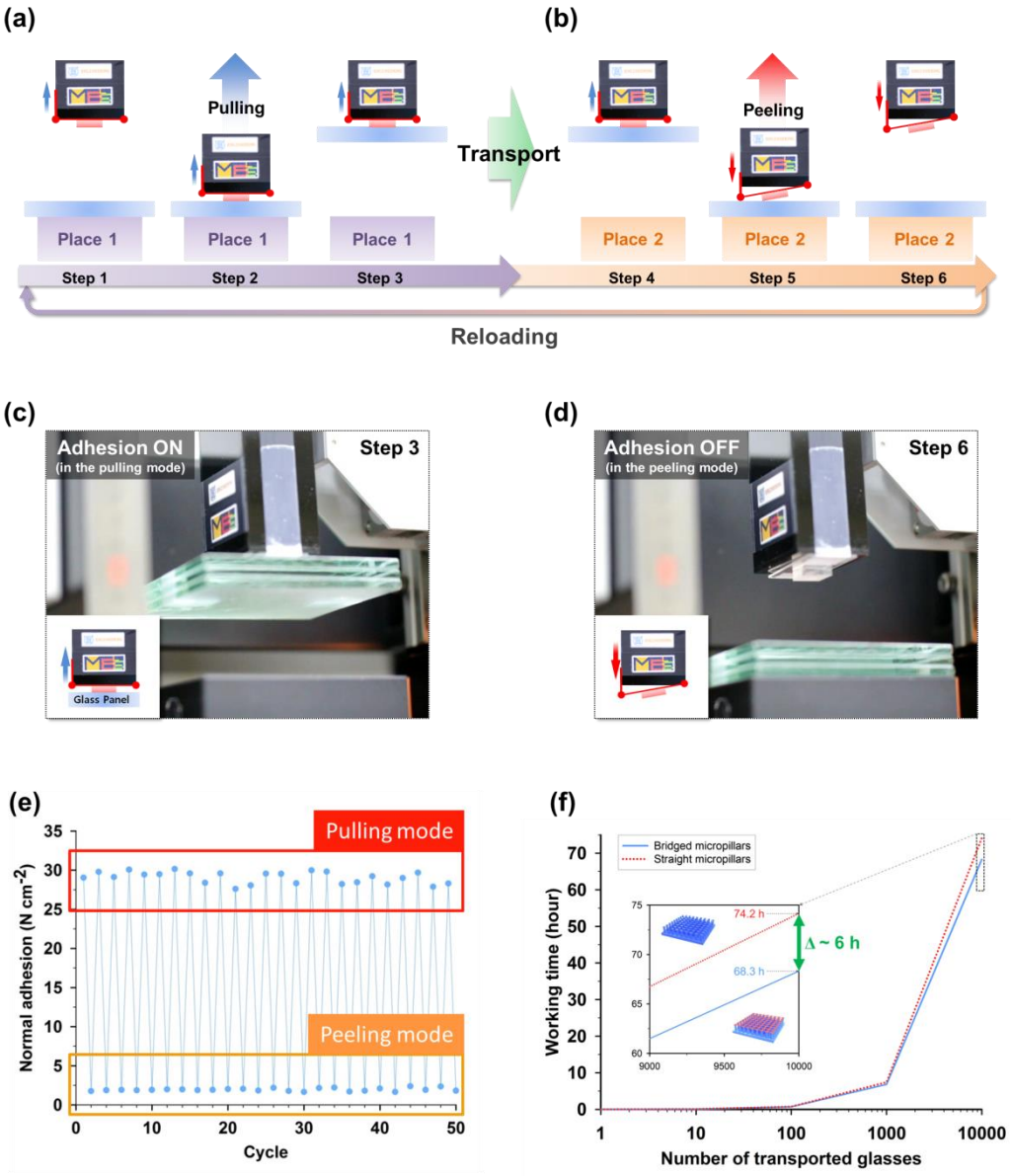

Figure. 4-6 (a-d) Demonstration of a prototype of automated transportation system based on the fibrillar adhesive with bridged pillars. (a) A stack of three glass slides was lifted from the stage in the pulling mode enabling the maximum macroscopic adhesion force and (b) laid on the stage again in the peeling mode by

switching to the minimized adhesion force. (c-d) Photographs showing the operation of the system (c) in the pulling and (d) peeling modes, respectively. (e) Plot of normal adhesion over 50 cycles under the preload of 30 N cm^{-2}, demonstrating a large difference in macroscopic normal adhesion force between on and off states. (f) Comparison of straight and bridged micropillars in terms of working time or yield of the operation with repeated cycles. The working conditions are as follows: displacement = 3 mm in normal direction, lifting speed = 0.6 mm/s, lowering speed = 0.3 mm/s, preload = 30 N cm^{-2} for 3 s.

4-4. Supplemental

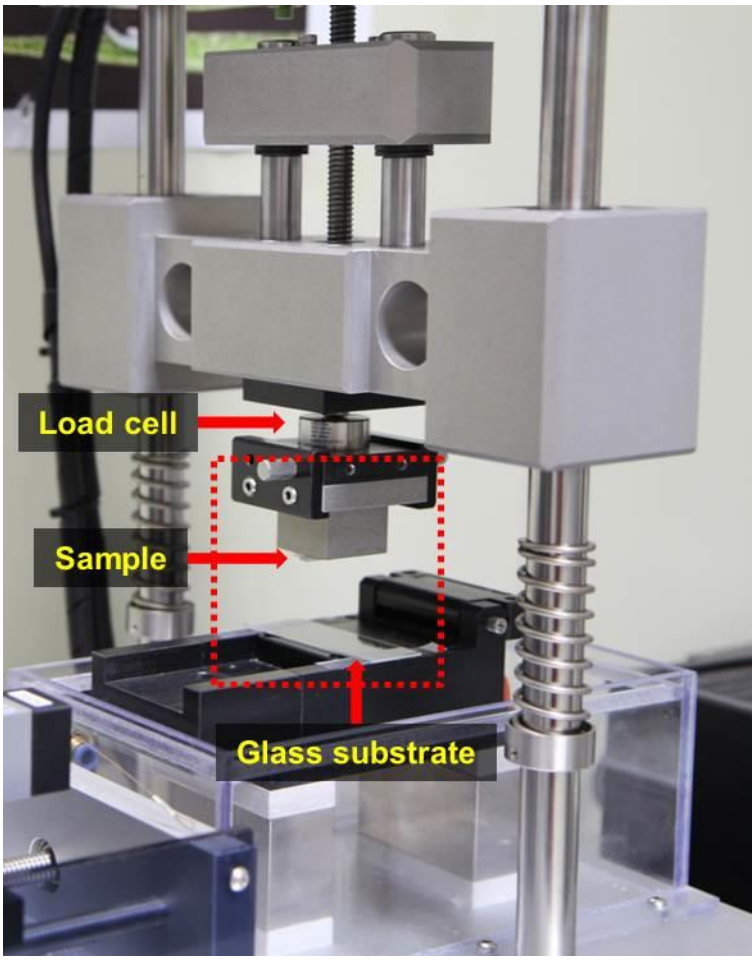

Figure. S1 A custom-built adhesion measurement system. The system is composed of a motorized driving part with a load cell moving in *z* (vertical) direction for installing an adhesive sample and a finely flat stage for contact surface.

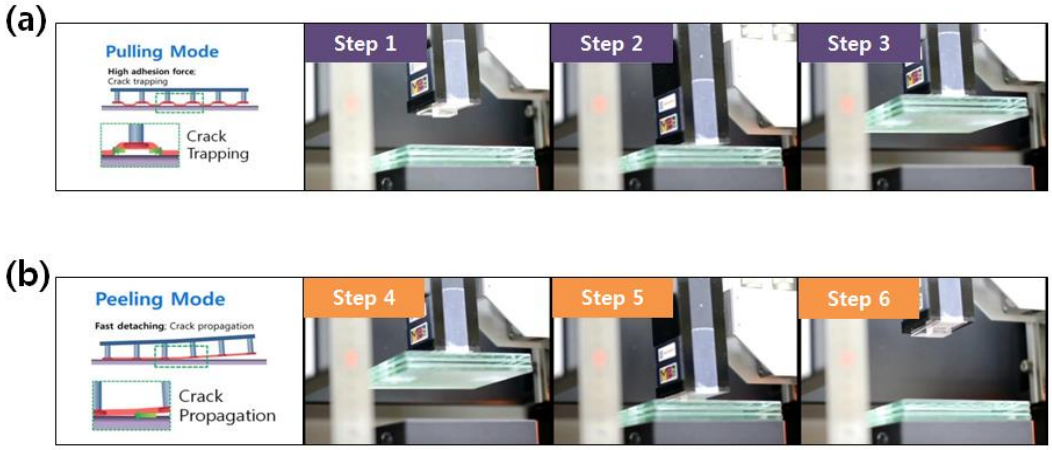

Figure. S2 Video snapshots show the sequential steps of pulling and peeling modes of the bridged micropillars. Each picture corresponds to the schematic illustration of the transportation system presented in **Figure 6a**.

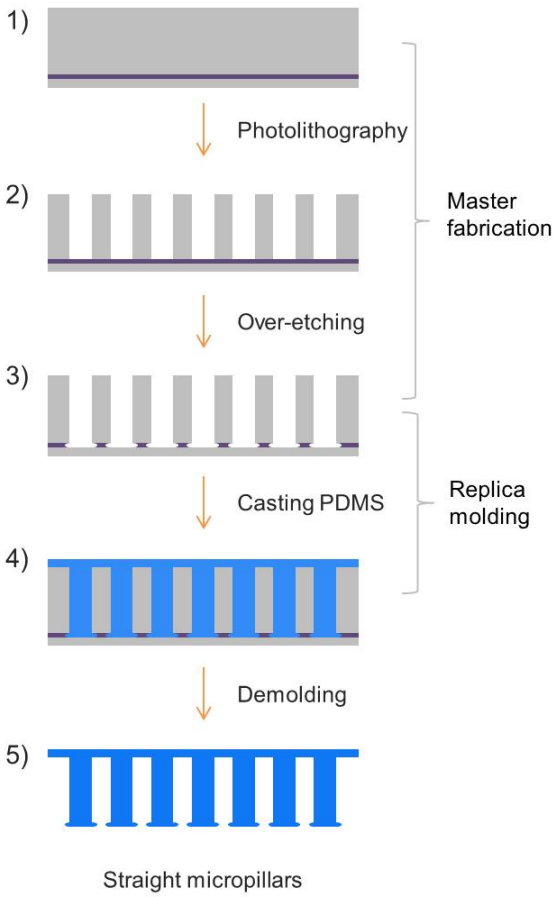

Figure. S3 A schematic illustration for fabricating the SOI master mold and replicating mushroom-like micropillars.

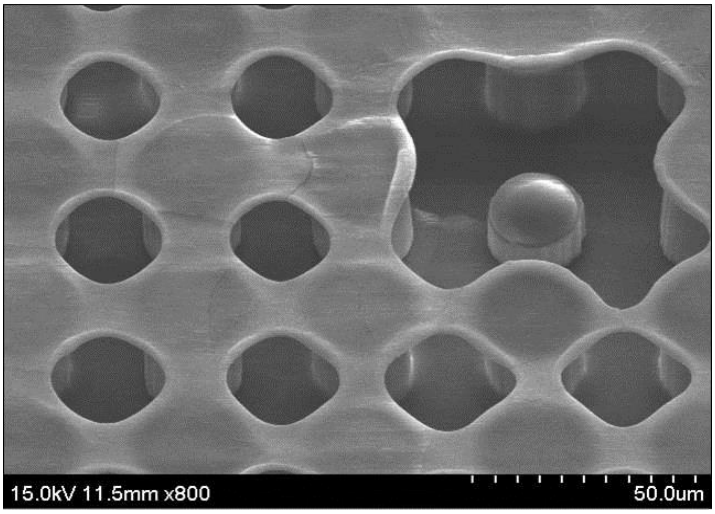

Figure. S4 An SEM image of the bridged micropillars with one arbitrary defect site, showing that the membrane of ~800 nm thickness is uniformly connecting the pillars in a grid, square pattern.

4-5. Summary

We have presented a smart fibrillar adhesive in the form of bridged micropillars covered with a thin elastomeric membrane and demonstrated an automated transportation system by exploiting the switchable adhesion. The fabrication process simply consists of replica moulding of micropillars and transfer of a low-viscosity PDMS precursor to the micropillar heads, which was then squeezed and merged to form a network of bridged micropillars capped by a uniform PDMS membrane. The fibrillar adhesive presented here is optimal for lifting a heavy object with flat surface at the expense of adhesion capability on rough surfaces; on a rough surface, mushroom-like micropillars would be more appropriate to render reasonable adhesion strength. We claim that the current scheme is highly useful for generating large normal adhesion as well as fast and easy detachment of flat objects, which can find diverse uses in the assembly and manipulation of micro- and macro-size parts.

Chapter 5. Bio-inspired design and fabrication for superhydrophobic metallic surface

5-1. Introduction

The unique wetting properties of lotus leaves have been a fascinating subject of research for many decades due to the fundamental interests in wetting and directional flow of water.[102] Lotus effect provides a variety of advantages such as non-wetting, self-cleaning from any dirts, and small flow resistance.[103] Extensive studies have been carried out to understand the mechanism of water repellency and self-cleaning behavior of lotus leaf.[104, 105] It is now widely accepted that superhydrophobicity is orchestrated by the existence of micro- and nanostructures on the low energy surface. Also, the scientists revealed that a distinctive hierarchical structure on the lotus leaf plays a key role in maintaining water repellency and self-cleaning behaviors.[106] These findings shed light on establishing the central design rule to build artificial superhydrophobic surfaces possessing the properties similar to those of lotus leaves.

A great number of methods have been developed to achieve artificial superhydrophobic surfaces.[107] Examples include nanoparticles-assembly,[108] lithographic patterning,[109] sol-gel method,[110] chemical vapor deposition,[111] electrospinning,[112] templating,[113] plasma fluorination.[114] Despite the success of

previous methods for extremely high contact angle (CA) (> 150°) and low CA hysteresis (< 5°), most structures have been made of soft materials such as polymers or colloidal assembly. Furthermore, a hydrophobic coating often required for hydrophobilization on the intrinsically hydrophilic surfaces. Superhydrophobic surfaces made of soft materials are usually fragile when exposed to mechanical impact such as raindrops or scratching. Moreover, the stability of hydrophobic coating is usually limited due to a process called aging.[115] Over time, a modified surface will be recovered to its original hydrophilic nature, rendering the superhydrophobicity decreased. For this reason, the widespread use of such kind of superhydrophobic surfaces in industrial applications is limited. Therefore, it is potentially of great benefit to develop a method to make a robust metallic superhydrophobic surface that does not collapse or deteriorate over time.

Attempts have been made to achieve the robustness of superhydrophobicity over mechanical wears and chemical deterioration using metallic surfaces. To create roughness on metallic surfaces, diverse methods have been proposed, such as laser texturing-chemical etching method,[116] femtosecond laser irradiation method,[117] sandblast method,[118] solution-immersion process,[119] anodic oxidation,[120] chemical etching,[121, 122] electrochemical etching,[123] boiling water immersion,[124] coating method[125] *etc*. In the laser texturing-chemical etching, a steel surface is structured with a microscale

roughness by using various laser power densities and texture directions. However, the method has potential weaknesses such as requirement of two-step processes (laser texturing and chemical etching) and use of flat two-dimensional surfaces to make a hierarchical structure. Laser irradiation method is a more improved way to texture a metallic surface, yet it still requires pretreatment such as chemical coating or polishing. Therefore, the methods based on laser are not suitable for generating hierarchical structures on curvature surfaces. In the sandblast and solution-immersion processes, a superhydrophobic metallic surface can be easily generated but a two-step fabrication process is still needed in the form of etching and chemical coating steps. Furthermore, it is hard to make well-defined dual-roughness surfaces with minimum run-to-run variations. Each of the rest of the aforementioned fabrication methods has its own merits with excellent water/oil-repellency; however, it has not been demonstrated to build a superhydrophobic metallic surface with a finely controlled hierarchical surface morphology in a minimized process, which does not include additional pretreatment steps of workpieces such as polishing or chemical treatments.

In this work, we present a one-step process for superhydrophobic metallic surface with hierarchical structure by wire electrical discharge machining (WEDM) on intrinsically hydrophobic Al 7075 alloy. In general, electrical discharge machining (EDM) utilizes a high potential difference between electrode and workpiece materials under dielectric liquids. The shapes of workpiece

materials can be controlled by the movement of electrode when a high potential difference melts or vaporizes workpiece materials. There are several types of EDM processes: die-sinking EDM, microEDM, and WEDM.[126, 127] Die-sinking EDM and microEDM can make various molds on difficult-to-cut materials according to the shape of electrode. Alternatively, WEDM uses a wire as an electrode to cut workpiece materials with features that can accommodate formation of complicated structures using a programmed wire path. During EDM process, an electrode and a workpiece are immersed in a dielectric fluid such as kerosene and de-ionized (DI) water.[128, 129] Generally, the working fluid for EDM has high resistivity, which keeps dielectric strength as the voltage is applied to an electrode and a workpiece. When the electrode approaches the surface of workpiece materials in a relatively narrow distance, the working fluid loses the dielectric character and becomes the medium of discharge sparks. Subsequently, when a high voltage is provided within the gap, an electrical discharge is initiated, in which electrical energy is converted into heat. As a result, a small amount of material is melted and vaporized at the electrode and workpiece.[129, 130] In this process, a small cavity, called crater, is generated both on the electrode and workpiece surfaces, ultimately leading to the formation of randomly distributed craters. While the craters are sometimes undesired, they can be potentially used to create roughness in different scale to create hierarchical structure for superhydrophobicity.

The surface roughness of these craters is determined by various discharge conditions such as discharge current and duration. In many industrial surfaces, WEDM is widely used to generate roughness on metallic surfaces simply by controlling electric pulse parameters.[131] There are several advantages of WEDM can be derived. First, a microscale sinusoidal pattern can be formed by a simple programming of wire path with a wide range of wavelengths (λ = 200 to 500 μm).[126] Second, it is possible to texture curved surfaces via WEDM by programming wire path with consideration for the profile of the workpiece. Third, a secondary microscale roughness is spontaneously created on the machined surface in the form of craters. When sculpturing of metallic surface is done on intrinsically hydrophobic mateirals, the nature of WEDM process will provide a hierarchical structure in one-step process without additional chemical treatment, which leads to a superhydrophobic surface with an exceptional robustness enough for industrial use.

5-2. Experimental

Materials: We used a commercially available Al 7075 alloy (duralumin). The Al 7075 alloy is composed of Al (87.1 - 91.4%), Cr (0.18 - 0.280%), Cu (1.20 - 2.0%), Fe (< 0.50%), Mg (2.10 - 2.90%), Mn (< 0.30%), Si (< 0.40%), Ti (< 0.20 %), and Zn (5.10 - 6.10%). This alloy is widely used in the structural components of aircraft and automotive industries due to its exceptionally high strength to weight ratio.[132]

Contact angle measurements: Static contact angles (CAs) and CA hysteresis of liquids used in experiment were measured using DSA100 goniometer (Kruss, Germany). In each measurement, a 6 μL of liquid was dispensed on the surface over the time span of 1.5 min. The measurement was averaged over at least six different locations for each sample conditions.

Surface energy measurement: The surface energy was evaluated using the Owens-Wendt method with de-ionized (DI) water and formamide (de-ionized, 99.5%, Sigma) as two probing liquids[133]. The wetting angles of both liquids were measured on nearly idealized-flat Al 7075 alloy surface. To achieve idealized flat-Al 7075 alloy surface, the bulk sample was ground with multi-step sand paper grinding of different grits from 320, 600, 1000, and 1500 accompanied by water flowing as lubricant. Finally, the sample was polished with alumina powder

suspension.[134] A shiny flat Al 7075 alloy was achieved after the process to simulate the idealized-flat surface for wetting angle measurement.

Scanning electron microscopy: SEM images were obtained using SEM (S-4800, Hitachi, Japan) at an acceleration voltage of 15.0 kV and an average working distance of 11.4 mm.

White light scanning interferometry: In order to acquire average roughness and morphologic images of the dual-scale roughness metallic surfaces, we mounted the specimen on a stage of non-contact three-dimensional surface profiler (NanoView-E1000; NanoSystem, Daejeon, Korea). Images of 600 μm × 500 μm area were acquired accordingly.

5-3. Results and Discussion

Figure 5-1a illustrates a schematic of the WEDM process for fabricating dual-scale roughness on metallic surfaces with superhydrophobicity. Here, the primary roughness is formed in the shape of sinusoidal profile in several hundreds of micrometer wavelength (see Table 5-1) and the secondary roughness is naturally generated with crater-like structures of a few micrometers in **Figure 5-1b**, covering the entire Al 7075 alloy surface. As seen from **Figure 5-1c**, the fabricated surface shows visible microscale wavy patterns (λ = 500 μm) with superhydrophobicity (CA > 156 ± 5°). To demonstrate the water-repellency on as-prepared metallic surface, the free falling of water drops was recorded with high-speed camera (Redlake HS4-C-2) at a rate of 500 frames/s with the pixel resolution of 436 × 416 (**Figure S1**). In this research, a commercial WEDM machine (EZ20S, Seoul Precision Machine Co., Ltd.) was used to make sinusoidal patterns and surface roughness on an Al 7075 alloy surface. In the machining process, DI water was used as the dielectric fluid. Because both the electrode and workpiece are machined simultaneously in the EDM process, a wire feed system needs to continuously supply a wire electrode for machining accuracy and prevent the wire breakage as shown in **Figure 5-2a**. The substrate used in this study was an Al 7075 alloy with the dimension of 30 mm length × 30 mm width × 2 mm thickness.

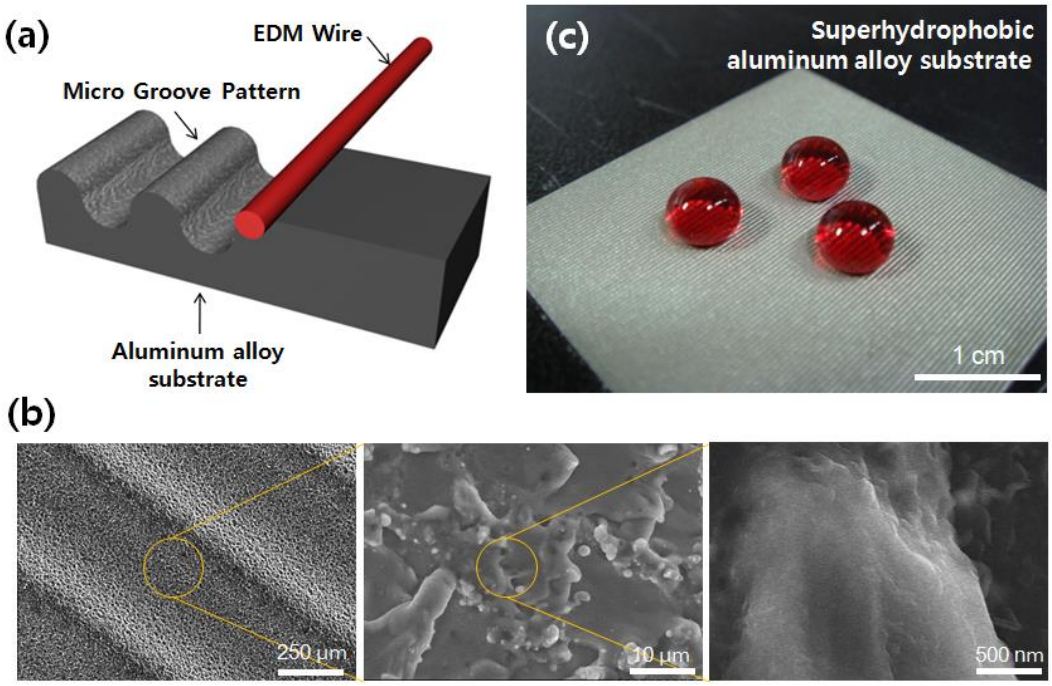

Figure 5-1. (a) Schematic diagram to fabricate dual-scale structures on metallic surfaces by WEDM. By using a single step machining of sinusoidal patterns, a secondary roughness is spontaneously formed due to surface exfoliation process. (b) Optical image of the droplets of dyed-DI water on the fabricated aluminum surface in (a). (c) The SEM images of patterned metallic surface with distinct dual-scale structures.

Table 5-1. Cross-sectional profiles of the primary roughness formed on the surface of Al 7075 alloy by WEDM

Wavelength, λ [µm]	Profile	Amplitude [µm]	Aspect ratio	Roughness factor
500	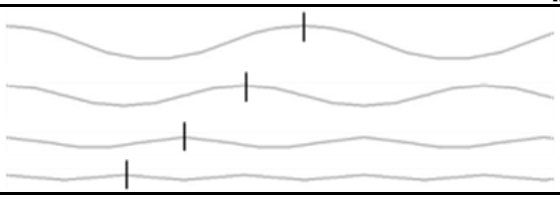	74	1.44	1.059
400		46	1.33	1.043
300		25	1.23	1.016
200		10	1.13	1.003

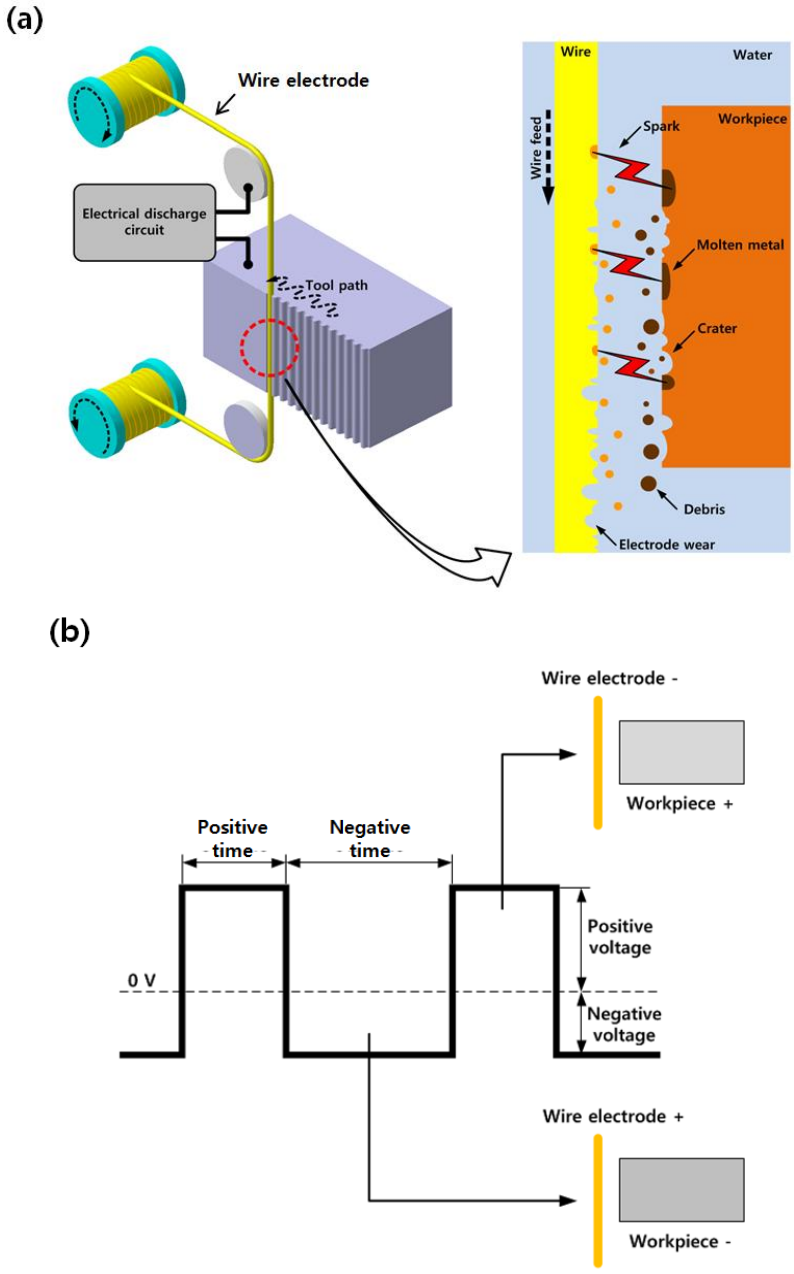

Figure 5-2. (a) Schematic diagram of WEDM process.(b) A waveform of voltage between a workpiece and a wire electrode

In **Figure 5-2b**, a square wave AC voltage was applied to the machining gap between the wire electrode and the workpiece for anti-corrosion.[135] Here, the positive duration ranged from 15 to 30 μs, and the negative duration from 20 to 50 μs (see Table S1). It is interesting to note that the average roughness was increased almost linearly with the increase of the applied energy in the WEDM process (i.e., applied voltage and current) and the charging duration. It seems that the formation of craters is attributed to the localized melting and evaporation of the surface due to the applied charges. The local defects and/or weak phases on Al 7075 alloy surface may become the initial seed for craters formation when a high potential energy difference is applied. In this case, the application of a higher energy will result in a highly localized increase of temperature for melting and evaporation of workpiece. Therefore, a larger crater or roughness can be made using a higher applied energy as shown in Table S1.

In the conventional WEDM process, a four–step process involving different applied energy has been usually implemented to make a smooth machining. In our experiment, the largest electrical discharge energy was applied in the first cutting, resulting in the highest surface average roughness of 4.16 μm (**Figure 5-3a**). The purpose of the first cut was to create the deepest cutting according to the programmed shape. In the subsequent cutting steps, the applied energy was gradually reduced in such a way that the surface average roughness monotonically decreased from 2.35 to 0.41 μm (**Figure 5-3b**). Therefore, the

surface became highly smooth and polished after the four cutting steps. **Figure 5-3c** shows the SEM images of WEDM processed Al 7075 alloy surface with secondary roughness from 1^{st} to 4^{th} cut.

To perform a detail study on the effect of WEDM process parameters such as roughness and wetting angles, the samples were classified based on the number of cutting steps and sinusoidal wavelength. As shown in Table 2, 16 different types of surfaces were fabricated by the WEDM and subsequently analyzed with CA measurements. For convenience, the samples were divided into four groups (4 samples in each group) depending on the wavelength of sinusoidal patterns: 200, 300, 400, and 500 μm. All samples in each group were subjected to a series of four cutting steps following the conditions in Table S1.

Superhydrophobicity can be achieved by creating hierarchical roughness on low surface energy coated materials.[105] Among various materials, metallic surfaces offer higher durability and robustness under harsh applications such as aerospace engines, ship hulls, and automobiles. In this case, the interplay between geometrical structures and surface chemistry is important for smart design and fabrication approaches for the superhydrophobicity on metallic surfaces.[118, 119, 121, 136] To this aim, aluminum alloys have been used in many industrial applications due to their superb properties, such as high corrosion resistance, good mechanical properties, abundance, and low weights. In addition to these properties, the Al

7075 alloy used in our experiment has a low surface energy (γ = 30.65 mJ/m^2) (See detail of surface energy components in Table 3).

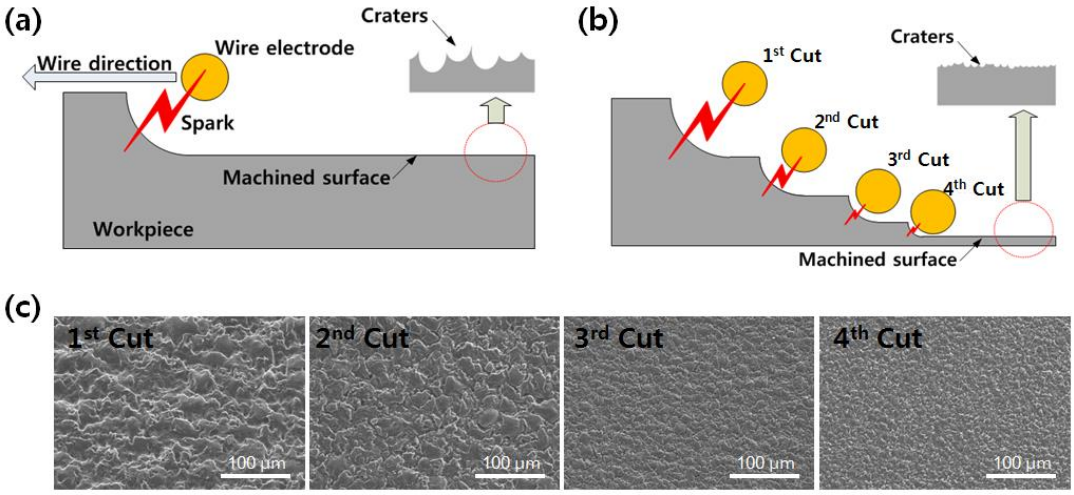

Figure 5-3. Schematic of the fabrication process with different machining conditions to obtain rough surface (a) and smooth surface (b). (c) SEM images of the secondary roughness with various cutting conditions.

Figure 5-4a shows a series of three-dimensional morphology images of the secondary roughness formed from the WEDM cutting process. The first cut of WEDM process with the highest energy produced the highest average roughness (Ra: ~ 4.16 μm) due to the formation of large craters. The second, third and fourth cuts produced lower average roughness of 2.37, 0.94, 0.41 μm, respectively, with lower energies, suggesting that there is a linear correlation between the surface roughness and the applied energy. The measurements of water CAs on the fabricated surfaces are shown in **Figure 2-4b** along with comparisons to theoretical models. Here, we employed the recent theoretical models by integrating the Wenzel and Cassie states on dual-scale structures, in which the wetting states can be categorized into four types:[105]

Wenzel-Wenzel or *W'-W"*:

$$\cos\theta_{app}^{W'-W"} = R'R"\cos\theta_e \qquad (1)$$

Wenzel-Cassie or *W'-C"*:

$$\cos\theta_{app}^{W'-C"} = R'\left\{f"\left(\cos\theta_e+1\right)-1\right\} \qquad (2)$$

Cassie-Wenzel or *C'-W"*:

$$\cos\theta_{app}^{C'-W"} = R"\left\{f'\left(\cos\theta_e+1\right)-1\right\} \qquad (3)$$

Cassie-Cassie or *C'-C"*:

$$\cos\theta_{app}^{C'-C''} = f'f''(\cos\theta_e + 1) - 1 \quad (4)$$

where *R*, *f*, θ_e represent the roughness, solid fraction, and equilibrium wetting angle, respectively, and the single and double apostrophes represent the first and second hierarchy scales, respectively. Based on the calculation of wetting angle on the secondary roughness of Al 7075 alloy, all cutting stages of WEDM produced wetting angles that were highly matched with the *C"* state with relatively low CAHs; 8.2°, 10.7°, 13.2°, 15.8° respectively. The Wenzel model for the same roughness values turned out to deviate largely from the experimental observations. On the other hand, Cassie-Baxter model shows a highly matched CAs on every sample with the estimated air fractions in the secondary roughness (*1-f"*) ranged from 0.65 to 0.5 on samples for the respective surface from 1st to 4th cut. It is indicative that the wetting state in the secondary roughness is stable in the Cassie-Baxter state. Therefore, we conclude that the possible wetting states in dual-scale roughness are only W-C and C-C in equations (2) and (4).

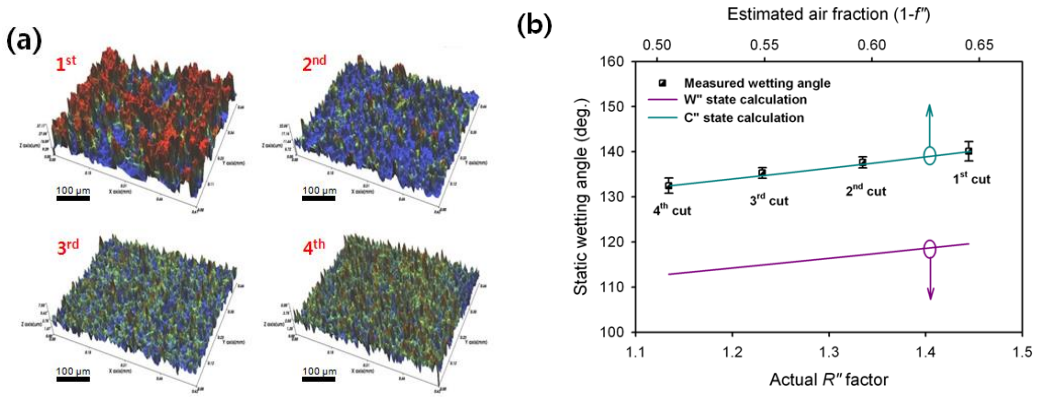

Figure 5-4. (a) Three-dimensional images of metallic surfaces after WEDM process taken by surface profiler. As shown, the 1st cut with higher energy produces the roughest surface compared to those in the 2nd, 3rd, and 4th cuts with lower energy. The static wetting angles on the corresponding surfaces are shown in (b) together with theoretical models using the Wenzel (purple line) and Cassie (blue line) states. Note that experimental measurements are highly matched with the Cassie state in all surfaces with relatively low CAHs; 8.2°, 10.7°, 13.2°, 15.8° respectively.

Further measurements of wetting angles on dual-scale roughness of Al 7075 alloy with the 1st cut process are shown in **Figure 5-5a**. Here, the microscale sinusoidal patterns with different wavelength show different wetting behaviors. For higher wavelengths (500 and 400 μm) with the 1st and 2nd cuts, the CAs were larger than 150° with CA hysteresis being lower than 3°. In contrast, for lower wavelengths (200 and 300 μm) with all cuts and higher wavelengths with the 3rd and 4th cuts, CAs were ~140° with higher CA hysteresis (> 5°). For the 1st and 2nd cuts in the wavelength of 500 and 400 μm, there was no significant difference in CAs seen in the front view (0°) and the side view (90°) because our hierarchical pattern structure had water droplet stay in the C'-C' state. However, there was a difference in CAs (<5°) on the rest of the cases in W'-C' state in **Figure S2**. A comparison between CA values (in Table 2) and the theoretical models with composite wetting states in equation (2) and (4) is shown in **Figure 2-5b**. Here, for the higher wavelengths with the 1st and 2nd cuts, the experimental data show good agreement to the *C'-C"* state. Then, there seems a transition to *W'-C"* state with the 3rd and 4th cuts. We postulate the transition from the *C'-C"* state to *W'-C"* is mainly due to the decrease of the amplitude of the sinusoidal profile of the surface as provided in Table 1, which give rise to the shift of the wetting state of the larger structures from Cassie-Baxter state to Wenzel state. In parallel, for the lower wavelengths the experimental measurements show excellent agreement

with the *W'-C"* state. This suggests that the WEDM method presented here has designing capability to tune surface texture and wettability.

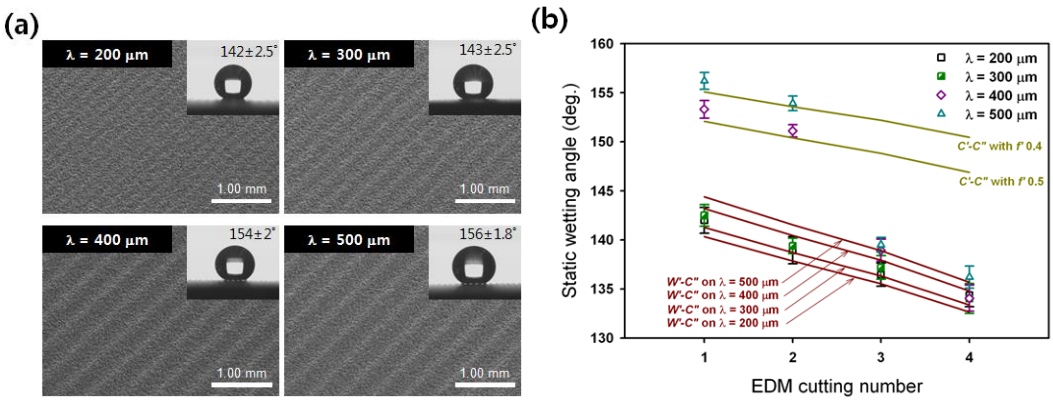

Figure 5-5. (a) SEM images of hierarchical structures on metallic surfaces with various wavelengths (λ) of sinusoidal micropatterns. The optical images of water droplets are shown in the inset. (b) Static wetting angles on the various samples in (a) with comparison to theoretical models. As shown, the wetting states are highly matched with the *C'-C"* state (superhydrophobic) for the samples with λ = 400 μm and 500 μm with one- or two-step WEDM process. For three-step WEDM process or higher, a transition to the *W'-C"* state is observed. For the samples with λ = 200 μm and 300 μm, the *W'-C"* state is likely to exist in all surfaces.

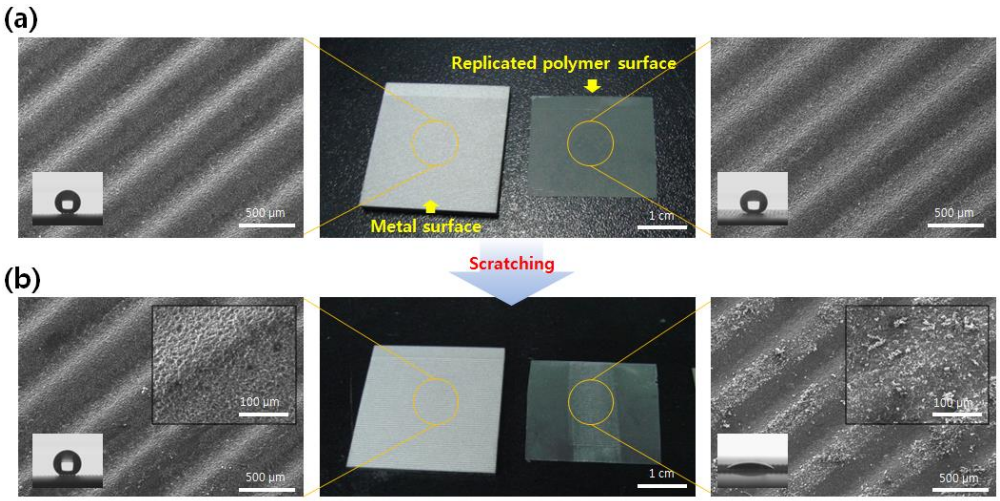

Figure 5-6. Comparison of superhydrophobicity robustness between Al 7075 alloy pattern by WEDM and its replica using hydrophobic polymer. A UV-curable perfluoropolyether(PFPE) was replicated from Al 7075 surface by UV-assisted capillary force lithography. (a) Optical and SEM images of as-prepared superhydrophobic Al 7075 alloy surface and polymer replica from the corresponding Al 7075 alloy surface. A similar geometry was achieved on the polymer replica. Insets in each SEM image shows the water wetting angle with the corresponding surfaces. Both Al 7075 alloy and its replica show superhydrophobicity with wetting angle of 156° and 165°, respectively. (b) Optical and SEM images of each sample after the scratching test using P3000 sand paper. While the Al 7075 alloy surface remained intact, the polymer surface was damaged after scratch test. The insets in SEM images show the corresponding water wetting angle after scratch test. On Al 7075 alloy the superhydrophobicity was maintained while on polymer replica the wetting angle was dropped into 15°.

Table 5-2. Set of samples with different types of surfaces profiles and their contact angles (CA)

	λ = 200 μm	λ = 300 μm	λ = 400 μm	λ = 500 μm
1st Cut	141.9°	142.5°	154.3°	156.5°
2nd Cut	139.0°	139.4°	151.1°	154.8°
3rd Cut	136.5°	137.2°	138.9°	140.3°
4th Cut	134.3°	136.0°	136.2°	140.8°

Table 5-3. Surface energy measurement of Al 7075 alloy

θ_e^{water} (deg.)	$\theta_e^{formimide}$ (deg.)	γ^{polar} (mJ/m^2)	$\gamma^{dispersive}$ (mJ/m^2)	γ (mJ/m^2)
109.5 ± 1.29	81.12 ± 0.85	0.07 ± 0.04	30.58 ± 1.38	30.65 ± 1.42

In order to briefly verify the potential of industrial use of our metallic superhydrophobic surface, two contrasting samples were prepared as demonstrated in **figure 5-6**, one of which is the metallic surface and the other is the replicated polymer surface made with perfluoropolyether(PFPE) which was fabricated by UV-assisted capillary force lithography[137]**.** After scratching both samples in a controlled manner with the P3000 sandpaper (Mean particle diameter: 7 μm) in **Figure S3**, In scratching experiment, the sandpaper was pulled out with 1.0 mm/s and stroke of 10 cm. When the preload was increased up to 2 N/cm^2, the metallic surface was found to remain intact, thereby holding the initial superhydrophobicity, whereas the polymer surface lost its water-repellency due to the mechanical damage on the surface. We could confirm that our metallic surface is superior to the polymer-based surface for industrial use which requires the robustness against harsh environment.

5-4. Supplemental

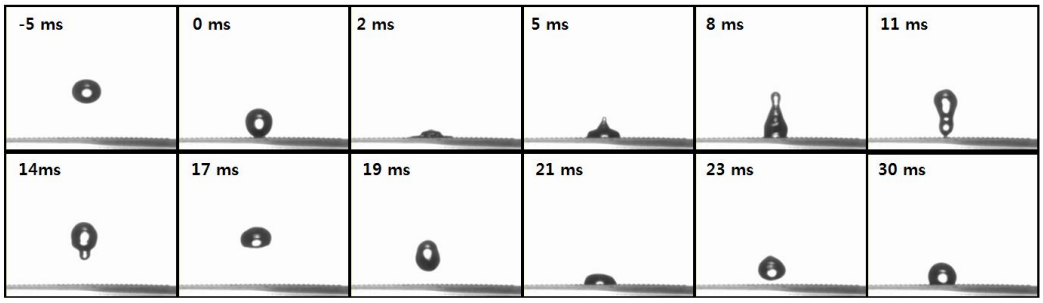

Figure S1. Snapshots of high-speed camera images of a bouncing water droplet on the fabricated superhydrophobic metal substrate in **Figure 1B** (λ = 500 μm, 1st cutting).

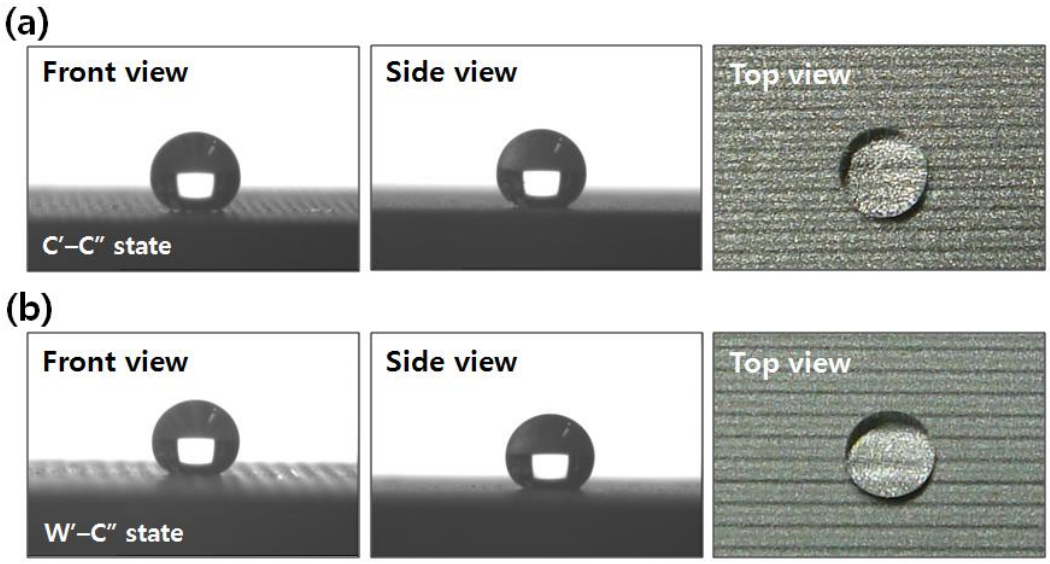

Figure S2. Optical images of water droplets on fabricated metallic surfaces with (a) C'-C" state, and (b) W'-C" state. In the C'-C' state, which was observed on the superhydrophobic surfaces, the CAs are barely different taken in two directions, a front view and a side view. On the other hand, in the W'-C" state, which was observed on the hydrophobic surfaces, the CAs have a little difference (less than 5°) in the two directions.

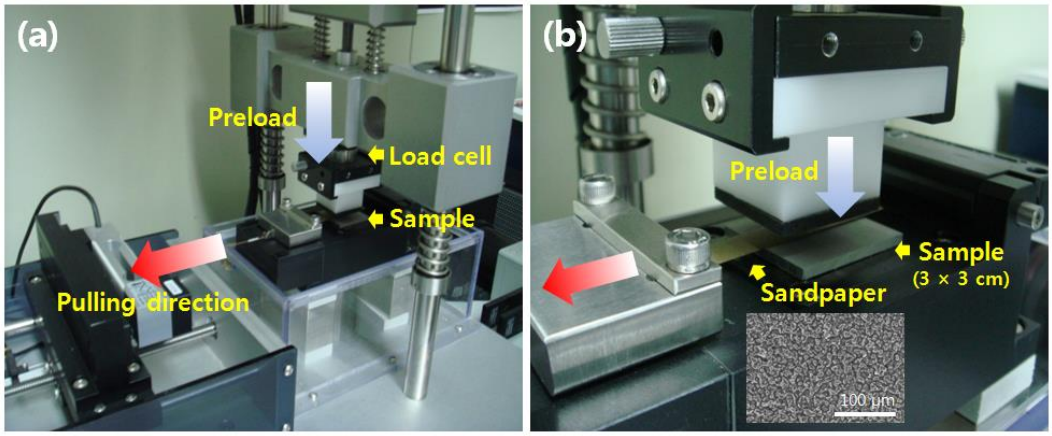

Figure S3. Optical images of the custom-built equipment used in our experiment for measurement of robustness of fabricated surface. (a) The P3000 sandpaper (Mean particle diameter: 7 μm, 1 cm in width) was laid on the fabricated dual-roughness surface was pressed with a controlled preload (~3N/cm^2). And then the sandpaper was pulled out to induce mechanical stimulus. (b) The magnified images and insert SEM images shows the P3000 sandpaper surface.

Table S1. WEDM process conditions used in the experiment.

WEDM Step	Positive voltage[v]	Negative voltage[v]	Current[A]	Positive duration	Negative duration	Roughness [Ra]	Roughness factor
1st Cut	+126 V	-80 V	150 A	28 μs	50 μs	4.16 μm	1.44
2nd Cut	+106 V	-80 V	42 A	30 μs	50 μs	2.37 μm	1.33
3rd Cut	+106 V	-76 V	12 A	14 μs	20 μs	0.94 μm	1.23
4th Cut	+84 V	-74 V	6 A	15 μs	20 μs	0.41 μm	1.13

5-5. Summary

We have presented a novel method to form dual-roughness superhydrophobic metallic surfaces by using WEDM process. Unlike the conventional methods involving a two-step fabrication of etching and coating, the current method allows for a robust metallic surface with the help of a one-step process involving a programmed wire path. A secondary roughness of several micrometers was spontaneously generated due to the exfoliation process without additional chemical treatment. The wetting state analysis demonstrated the presence of the Cassie state in the secondary roughness. Therefore, on dual-scale structures of metallic surfaces after the WEDM process, the corresponding wetting states were identified to be either the C'-C" state with a higher wavelength in the 1^{st} and 2^{nd} cuts or the W'-C" state in the 3^{rd} and 4^{th} cuts with a lower wavelength. This finding will be useful in designing an optimum process of superhydrophobic metallic surfaces by WEDM. It is envisioned that the WEDM method presented here will find many uses in making superhydrophobic metallic surfaces in more diverse applications with harsh environments.

Chapter 6. Bio-inspired design and fabrication for multiscale patterns by shape memory effect

6-1. Introduction

Tools for nanofabrication have played central roles in every field of nanoscience and nanotechnology. While photolithography has been and will be the mainstay for the purpose, there have been increasing demands for low-cost and high-throughput nanofabrication techniques in order to solve some of the limitations of photolithography. Accordingly, a myriad of unconventional lithographic methods have been introduced since the early 1990 based on various top-down and bottom-up approaches. Many extensive review papers are currently available to the interested readers.[138]

Among numerous achievements in the field of unconventional lithography, one notable success is the development of thermal nanoimprint lithography (t-NIL),[139] in which a thin polymer film on the substrate is imprinted with a hard mold at a temperature above the polymer's glass transition temperature (T_g). Due to its high reducibility and simplicity in the process, the method has been widely adopted and well established by many research groups with various materials and mold types. However, the use of high pressure and thermal treatment potentially limits the widespread application of t-NIL. As an alternative method, step and

flash imprint lithography (S-FIL) was suggested by Wilson's group.[140] Since S-FIL uses a low-viscosity UV-curing precursor as patterning material, the technique can be carried out at room temperature and at low pressure. Despite these major advances, the preparation of a high-resolution nanoscale mold still poses a hurdle to rapid turnover and commercialization of t-NIL and S-FIL methods.

To address this issue, many lithographic methods such as edge lithography[141], size reduction lithography[142], and nanopattern oxidation[143] have been developed in order to further reduce the feature size of nanopatterns for a given mold dimension. These methods have proven successful in terms of reduction capability but several drawbacks have been identified such as the need of high temperature, difficulty in controlling surface and edge profiles, uneven surface roughness in the oxidation process, *etc*. More recently, the technique termed "self-perfection by liquefaction (SPEL)" has been introduced to solve some of the limitations above,[144] but the application of SPEL over large areas appears challenging to ensure stringent fidelity and uniformity of patterns.

In addition to direct size reduction lithographic techniques, one can benefit from several excellent properties of smart materials (i.e., shape memory polymers or SMPs) when properly exploited in NIL. The SMP has an intrinsic ability to switch its shape from the temporary shape to the memorized one.[145, 146] This dramatic shape transition of SMPs can be used to reduce the size of initial patterns,

as first demonstrated by Khine group.[147] It has also been reported that nano-sized patterns can be made with SMPs via programmed thermal cycles.[148, 149] Although SMPs are suitable materials for micro- and nanopatterning, there has been no study utilizing the temperature memory effect (TME) of SMPs. According to recent findings[150, 151], SMPs remember specific temperatures at the time of programming, not the shapes. Namely, TME refers to the phenomenon that SMP recovers a specific shape depending on the temperature, based on the fact that SMP memorizes the very temperature when programmed. This observation is highly inspiring and beneficial in NIL, in the sense that it is possible to tailor or reduce the initial pattern sizes with proper thermal cycles.[152]

In this paper, we introduce a new cost-effective, scalable nanoimprint lithographic method for the sub-100nm-scale patterning by exploiting the TME in SMP and self-replication characteristic of UV-curable materials. We propose a two-step temperature programming procedure to take advantage of the TME in a polyethylene-based SMP sheet. Briefly, a sheet of SMP is strained by 100% in the first programming, and subsequently imprinted at a higher temperature via nanoimprint lithography, which is the second programming. The difference in these two temperatures allows for a process window to tailor the dimension of the initial nanopatterns. Using this approach, size and pitch reduction of nanopatterns is demonstrated, which is capable of reducing the spacing by ~ 90% with respect to its original size. Furthermore, by utilizing self-replication property of UV-

curable materials, various size-controllable nanopatterns are generated with reduced pitches and sizes.

6-2. Experimental

Shape Memory Polymer (SMP) with Different Shrink Ratio. We purchased commercially available SMPs (shrink ratio 2:1 or 3:1) with covalently cross-linked polyethylene backbone from LS cable Inc., Korea. The thickness of SMP sheet was ~1 00 μm. This polymer is generally used for package film and shrinkable tube.[153] Mechanical properties were measured with a dynamic mechanical analyzer (TA Instruments, DMA2980) to determine the storage modulus (E') as a function of temperature. The sample was subjected to a cyclic tensile strain with amplitude of 10% at a frequency of 1 Hz. The temperature was increased at a heating rate of 2˚C/min in the range of -100 to 200˚C in supporting information Figure S1.

Thermal Nanoimprint Lithography (t-NIL) on SMP Film. A silicon master mold was placed onto the underlying SMP sheet after inserting a sandwiched PDMS buffer block (~ 0.1 cm thick) for uniform pressure distribution between the silicon master and SMP substrate. In the course of applying the pressure to 0.5 bar, the imprinting temperature was increased to 115℃ and the master was pressed for 20 min. After cooling to room temperature, the master was carefully removed from the substrate, leaving behind a patterned surface over an area of 3×3 cm^2.

Fabrication of Silicon Masters and PUA Replicas. A silicon master was

prepared by photolithography and reactive ion etching. The PUA replicas were prepared by replica molding from the imprinted SMP sheet. A UV-curable polymer resin of PUA (MINS 311 RM, Minuta Tech, Korea) precursor was dispensed on the surface of the SMP mold and a transparent poly(ethylene terephthalate) (PET) film of 50 μm thickness that was used as a supporting backplane was uniformly placed in conformal contact. After backfilling into the cavities, UV (λ = 250 ~ 400 nm) light was irradiated at an intensity of 90 mW/cm^2 for a few tens of seconds. After the exposure, the cured PUA replica carefully detached from the SMP mold. The PUA replica was additionally exposed to UV for several hours for complete curing.

Fabrication of multiscale SMP channels by irreversible bonding. It was performed in two consecutive steps. First, the temperature was set to 84°C in a precisely controlled water bath, and the ⅔ portion of the whole sample was immersed (in Figure 5a, the part that was not immersed in the bath was marked as "no heating"). Subsequently, the temperature was set to be 86°C and as soon as the temperature reached 86°C, the half of the portion which had been already immersed at 84°C was immediately immersed in the bath. For channel bonding, the patterned SMP and a 100-μm thick PET substrate were treated in oxygen plasma for 60 s (60W, PDC-32G, Harrick Scientific, Ossining, NY), and then the SMP channels were carefully aligned on the PET substrate and firmly pressed (500 g cm^{-2}) at 50℃ for 10 minute for irreversible channel assembly.

Visualization of Liquid Flow Inside the Channels. To visualize fluid flow inside the multiscale channels, a dilute solution of Rhodamine B dye (0.5 wt%, Sigma, St Louis, MO) in deonized water was introduced into the channels by surface tension-driven flow. The fluorescent images were captured under an inverted fluorescence microscope (IX71, Olympus Optical Co. Ltd., Tokyo, Japen).

Measurement of the Pull-off Force by Atomic Force Microscopy (AFM). The pull-off force was measured in air with a PSIA XE-100 (PSIA Inc., Korea) with a contact mode tip with diameter of 5 nm and height of 5 nm. 256 lines were scanned at a scan rate of 0.7 Hz over a region of 3 μm × 3 μm. The approaching and retracting tip speed was 0.3 μm/sec and the force limit was 12 nN. The pull-of force was obtained using XEP software in force-distance mode. In this mode, it was defined as the difference between the measured force in the approaching and retracting directions.

Scanning Electron Microscopy (SEM). Images were taken using high-resolution SEM (S4800, Hitachi, Japan) at an acceleration voltage higher than 5 kV and a working distance of 8 mm. Samples were coated with a 3-nm Au layer prior to analysis to prevent electron charging.

Measurement of Adhesion Force with Various Pillar Densities. The macroscopic normal adhesion force per unit area (1 cm × 1 cm) was measured by a hanging test. Samples with SMP micropillars with different pillar density were

prepared prior to the adhesion test. Each sample was attached to the surface of silicon wafer under a preload of ~0.3 N/cm^2 and the direction of peeling by a hanging weight was set in the normal direction. The weight was gradually increased until an adhesion failure occurred and the corresponding weight was interpreted as an adhesion force.

6-2. Results and Discussion

For the shape memory material, we used a commercially available SMP (shrink ratio 2:1 or 3:1) which is composed of covalently cross-linked polyethylene backbone; it is generally used for package film and shrinkable tube.[153] This material is very cheap and easily purchased less than a dollar per square meter. As is known, at a temperature above T_{trans} (= 80℃), the SMP sheet becomes flexible and highly elastic, and thus can be deformed (at 80℃, E' = 5.5 MPa). Below T_{trans}, the flexibility becomes limited and the shape can be fixed without further modification (at 25℃, E' = 43.7 MPa). Reheating the SMP above T_{trans} cleaves physical cross-links in the switching phase and thus forces the material back to its original memory shape.[146]

In the recovery process, two temperature programming steps were devised: First we used a SMP sheet as a nanoimprinting substrate, which was initially programmed near at 80℃. This is because T_{trans} was measured to be ~ 80℃ (see DMA tests shown in supporting information Figure S1). Subsequently, the second programming was performed by nanoimprinting the sheet at a higher temperature (T_{im} = 115°C). The second programming temperature is predominantly memorized by the sheet due to TME. As a consequence, the sheet would not shrink below T_{trans}, and sharply recover its original shape above T_{trans}. It is noted

that sharper transitions were observed with the increase of the programming temperature.[150]

Pitch and size reduction process with selective contraction property.

Figure 6-1 shows a schematic diagram for the size reduction lithography to fabricate size-controllable nanopatterns from an imprinted SMP sheet. The sequential steps of imprinting process are shown in **Figure 6-1a**. First, a SMP sheet with a shrink ratio of 2:1 was prepared (thickness: 100 μm, size: 3×3 cm^2) by stretching uni-directionally twice at ~ 80℃ with respect to the original length direction. In this step, the length of the SMP sheet was increased by 100%, which was defined as the first thermal programming.

Second, the second programming was performed through t-NIL process; a nanopatterned silicon master mold was pressed onto the first programmed SMP sheet much above T_{trans}, typically at 115℃ for 20 minutes at 0.5 bar. In this step, the imprinting temperature must be higher than that of the first thermal programming so as to take advantage of wide temperature difference between the two steps as dictated by the TME. After cooling to room temperature, the silicon master was removed from the imprinted SMP film, leaving behind the replicated nanopatterns on the surface.

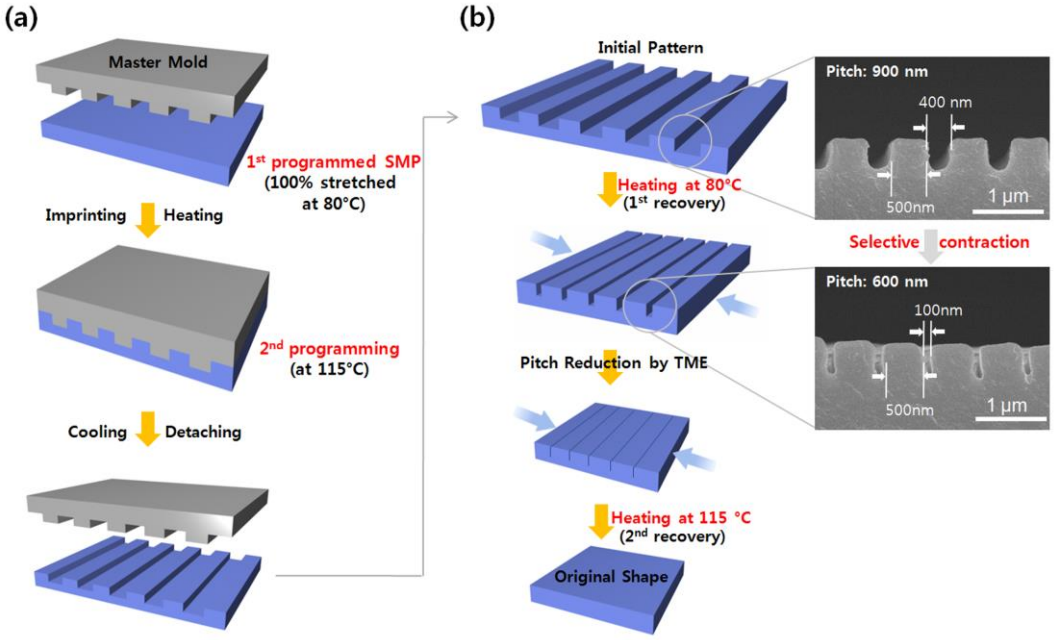

Figure 1. Schematic illustrations of (a) the nanoimprinting process with the first and second programming steps and (b) the recovery process via temperature memory effect (two step recoveries). First a nanopatterned SMP sheet was heated slightly above T_{trans} (80°C ~ 90°C) to selectively reduce the spacing part of the pattern. The cross–sectional SEM images show an example of reduced spacing by ~75% with respect to the original size. Finally, the SMP sheet recovers its original shape after heating to the second programming temperature of 115°C.

Figure 6-1b shows recovery process of the two-step programmed SMP film with line patterns. When the imprinted SMP was heated above T_{trans} (below the second temperature), it was reported that a new structure of heat-sensitive crosslink was formed, such that a gradual unidirectional contraction was observed.[154] It is intriguing to note that, when contracted through the recovery process, the spacing of the SMP film was selectively reduced. Consequently, we observed a monotonic decrease of the spacing by ~ 75% in proportion to the amount of temperature rise, without any noticeable reduction of line with and height. When the SMP was further heated to T_{im} of 115°C, then the space parts were ultimately collapsed, accompanying the reduction of pattern height as well (see supporting information Figure S2). The fact that the sheet shrinks largely in the lateral direction, not in the vertical direction, may be attributed to the initial lateral stretching at the first programming. Also, it is worthwhile noting that the polymer chains can readily memorize the second programming since the sheet still has storage modulus about 1 MPa at the second programming temperature (see supporting information Figure S1).

The cross-sectional SEM images in **Figure 6-1b** demonstrate this unique characteristic of the contracted SMP sheet. As shown, the initial nanopatterns on the second programmed SMP film showed 500 nm width, 400 nm spacing and 500 nm depth (pitch: 900 nm). After the recovery process (heating at 86℃ for 3 seconds), the geometry was reconstructed to 500 nm width, 100 nm spacing and

500 nm depth, suggesting that the reduction of pattern spacing precedes the recovery of line patterns, yielding a reduced pitch of 600 nm in the recovery process. As a result, an array of highly narrow and deep trench (aspect ratio: 5) was produced, which would be expensive to fabricate with other existing lithographic techniques. Also, the ability to form uniform nanopatterns over large areas (~ 3 × 1.5 cm^2) without many defects was evaluated as shown in Figure S3 (supporting information).

To investigate the effects of imprint temperature, we conducted the first and second programming at the same temperature. Under such conditions it was found that the patterns were collapsed at a temperature slightly above T_{trans}. As shown in **Figure 6-2**, the initial pattern was produced at T_{trans} of 80℃ (500-nm line, 400-nm spacing and 500-nm depth), showing good edge definition and pattern fidelity. When the heating was done at 84℃, the spacing became rounded with a reduced depth of 250 nm. For a higher temperature of 86℃, the initial pattern was further flattened with rounded corners with a smaller depth (150 nm). Finally, the SMP sheet completely recovered its original shape (i.e., flattened) at a higher temperature (> 86℃). This fact suggests the importance of the second programming step at a temperature much above T_{trans} to ensure good pattern fidelity throughout the heating cycles.

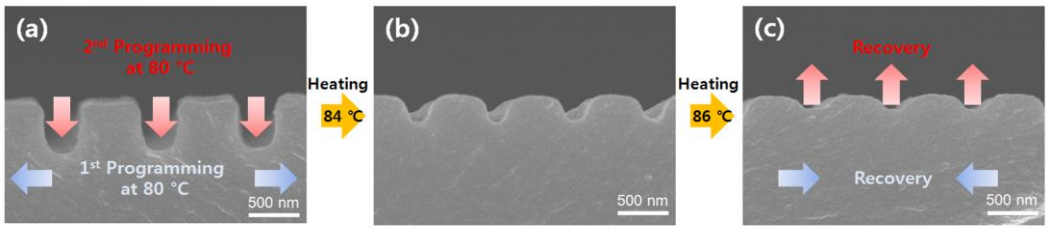

Figure 2. SEM images showing the pattern evolution when the first and second programming temperatures are the same (T_{trans} = T_{im} = 80℃): (a) initial nanoimprinted structure (500 nm line, 400 nm spacing and 500 nm depth), (b) a rounded structure with a reduced depth (~ 250 nm) when heated at 84℃ and (c) a further flattened structure (depth: ~ 150 nm) after recovery process at 86℃. As shown, the pattern gradually disappears as the temperature increases. Here, the horizontal contraction corresponds to the first programming, while the vertical recovery to the second programming,

Fabrication of various nanopatterns from one master mold.

Figure 6-3 illustrates the way to create various size-controllable nanopatterns with reduced pitch by using the TME and self replication characteristic. First, the imprinted SMP film with an equal line-and-space pattern (400-nm line and 400-nm space) was produced by nanoimprinting with a silicon master mold onto a first programmed SMP film (100% one-way stretched) (**Figure 6-3a**). Second, the imprinted SMP film was heated at 84℃ and the spacing of the pattern was reduced to 250 nm (**Figure 6-3b**). Then, the pattern was heated again at 86 ℃, resulting in the further reduction of the spacing to 100 nm with the same line width (**Figure 6-3c**). It is noted that the line width was not changed throughout the entire annealing steps with the pitch being selectively reduced from 800 to 500 nm.

In order to reduce the line width using the same recovery process, we utilized the replica molding and self-replication of UV-curable materials. In the self-replication step, a replica of UV-curable material with positive (or negative) sense can be made from the same material template with negative (or positive) sense after annihilating all reactive surface groups.[155] As an UV-curable mold material, poly(urethane acrylate) (PUA) was used for its relatively high Young's modulus (320 MPa) and flexibility.[77] After the replica molding and self-replication, one can obtain a PUA master mold with 400 nm width and 100 nm

spacing. This mold can be used to transfer the pattern to a new first programmed SMP film (100% one-way stretched) by nanoimprinting and the resulting structure is shown in **Figure 6-3d**. By repeating the same thermal cycles shown in Figure 3a-c, the pattern spacing was reduced to 250 nm at 84℃ (Figure 3e) and further to 100 nm at 86℃ (Figure 3f) with the same line width of 100 nm. Therefore, the final pattern dimension of 100 nm width and 100 nm spacing (pitch: 200 nm) was obtained, which was significantly reduced from the original dimension of 400 nm width and 400 nm spacing (pitch: 800 nm). This clearly demonstrates the capability of reducing the size and pitch at the same time by simply employing nanoimprinting, replica molding, and self-replication with a SMP film.

Also, the dimension of nanopatterns can be controlled with a SMP film with a different shrink ratio. For example, for the shrink ratio of 3:1, it was possible to reduce the spacing of nanopattern up to 90% in a facile manner. Figure 4 displays such an example by using an initial imprinted line pattern of 250 nm width and 750 nm spacing. To prepare the imprinted SMP line pattern, we performed the thermal imprinting process onto the 200% stretched SMP sheet (**Figure 6-4a**), which was followed by pattern replication by nanoimprinting to the stretched SMP substrate (**Figure 6-4b**). After similar thermal cycles in **Figure 6-3**, the pattern spacing was monotonically reduced from 750 nm to 250 nm (**Figure 6-4c**, T = 86℃) and 70 nm (**Figure 6-4d**, T = 89℃).

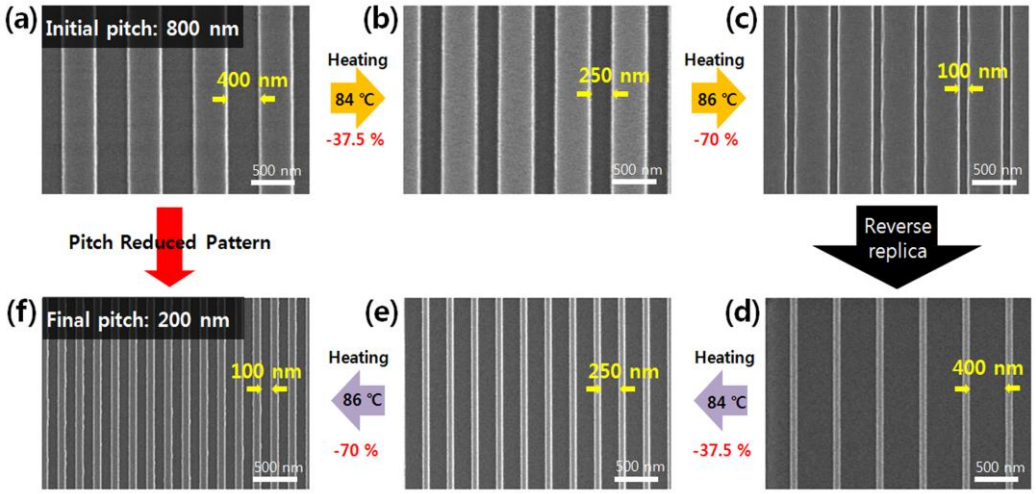

Figure 3. SEM images for the fabrication of various size-controllable nanopatterns by TME and self-replication of a UV curable PUA mold: (a) Initial imprinted SMP pattern with 400 nm width and 400 nm spacing. (b) Reduced spacing to 250 nm (37.5% reduction) when heated to 84°C, (c) Reduced spacing to 100 nm (75% reduction) when heated to 86°C. (d) Inverse replica of patterned SMP with 100 nm width and 400 nm spacing after replica molding and self-replication. (e) Reduced spacing to 250 nm (37.5% reduction) when heated to 84°C. (f) Reduced spacing to 100 nm (75% reduction) when heated to 86°C.

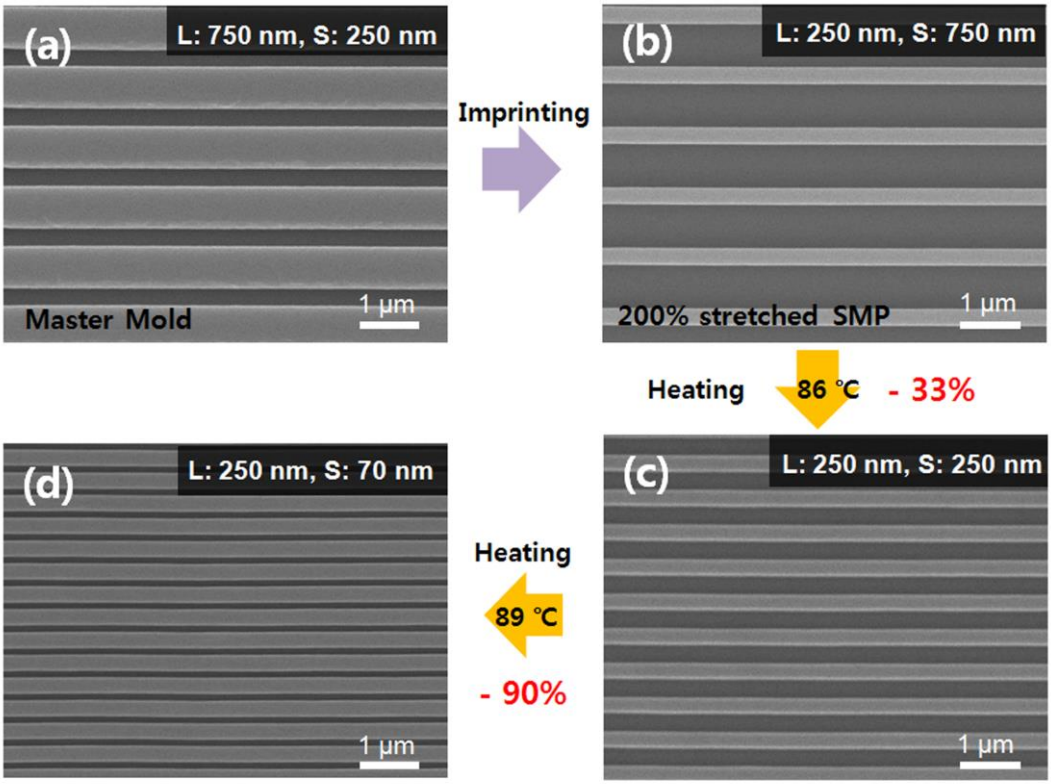

Figure 4. Pattern formation with a 200 % uni-directionally stretched SMP sheet (shrink ratio = 3:1). SEM images showing (a) silicon master mold for NIL, (b) imprinted SMP pattern, (c) the same after recovery process at 86℃ (spacing: 250 nm), and (d) the same after recovery process at 89℃ (spacing: 70 nm).

Fabrication of multiscale patterns and channels.

According to our experimental findings, there are three unique features compared to other size reduction lithographic methods. First, unlike previous size reduction methods (e.g., reflow and self perfection by liquefaction),[144, 149, 156] the pattern size and pitch can change simultaneously, which offers a great advantage in fabricating size-variable nanopatterns from a single master pattern. In the current scheme, only the spacing is reduced during the recovery process but the pattern width can also be varied by replica molding and self-replication as demonstrated above. Second, various patterns can be formed in a monolithic fashion, thereby removing any interfacial failure (e.g., thermal mismatch and poor adhesion) at the interface between the patterned film and the substrate.

Lastly, multiscale patterns with different spacing or gradient spacing can be prepared on a single substrate by local heat treatment as shown in **Figure 6-5a**. To this aim, we fabricated size-variable line arrays over a large area (3×3 cm^2) using initial pattern geometry of 1 μm width, 1 μm spacing, and 500 nm depth (shrink ratio: 3:1). The resulting pattern was composed of an array of parallel ridges (width: 1 μm) with various interspaces ranging from 1 μm to 250 nm by gradient heat treatment in a temperature-controlled water bath from 86℃ to 84℃. The film thickness also showed a gradual change along the multiscale pattern, ranging from ~ 100 um to ~ 200 um. The pattern dimensions were characterized by SEM, corresponding to the expected profiles for each heat treatment. These

multiscale patterns of SMP were transferred to PUA by replica molding as shown in **Figure 6-5b**, suggesting that the single to multiscale patterns can be generated via a suitable design of thermal cycles.

For potential applications to micro- to nanofluidics,[157] we fabricated multiscale SMP gradient channels (1 μm ~ 250 nm in width and 500 nm in height) after irreversible bonding. The bonding strength between PET and SMP was sufficiently high, such that a manual detachment was not possible.[158] Figure 5c shows a schematic illustration of fabricating SMP gradient channels and the fluorescent images after introducing a fluorescent dye of Rhodamine B (0.05 wt%, Sigma, St Louis, MO) in DI water by surface tension-driven flow. As shown, the multiscale channel dimensions are clearly visible under an optical microscope.

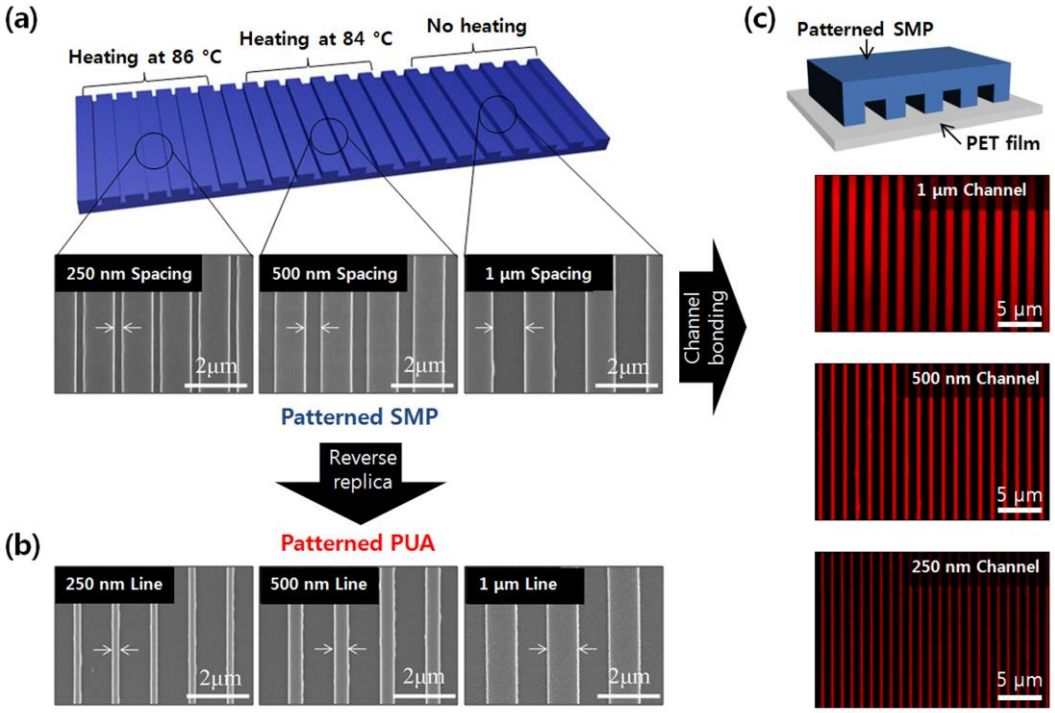

Figure 5. Fabrication of gradient patterns by a temperature gradient: (a) Fabrication of a SMP gradient pattern by local heating. As shown, multiscale patterns ranging from 1 μm to 250 nm (75% reduction) were formed on the same SMP substrate. (b) SEM images of the replicated PUA pattern from the patterned SMP. (C) Schematic of fabricating multiscale SMP gradient channels. Fluorescent images of a Rhodamine B dye in DI water after introduction into the channels by surface-tension driven flow.

Characterization of density variations along an imprinted pattern.

The most significant and notable observation is that only the pattern spacing is reduced with the same line width during the recovery procedure. To address this issue, we assumed that the memory effect would be different for the imprinted and non-imprinted regions. Unlike a typical deformation process involving a SMP, the current nanoimprinting process might generate an anisotropic physical distortion of polymer chains in the vertical and lateral directions. Namely, the spacing part would be more compressed than the line part, implying that the molecular or chain density would be different along the imprinted polymer surface.[159] As described earlier, the memory effect would not be annihilated at the imprint temperature as evidenced by a fairly high modulus of ~ 1 MPa (see supporting information Figure S1). As such, when an imprinted SMP sheet is heated above the first programming temperature, the memory effect would be more exerted in the compressed region of the polymer film. As a result, the spacing part becomes contracted first, preceding the recovery of the line part.

To verify this hypothesis, we analyzed density variations of the imprinted SMP layer with AFM set-up. This can be done by measuring the pull-off force in force-distance mode, being defined as the difference between the measured forces in the approaching and retracing directions. For the analysis, we used an imprinted

pattern of 350 nm width, 350 nm spacing, and 350 nm depth (Figure 6a) and AFM images in contact mode (PSIA XE-150, PSIA Inc., Korea).

Figure 6-6b shows representative force-distance curves, demonstrating that the pull-off force of the space part was three times higher than that of the line part. **Figure 6-6c** shows histograms of pull-off force for line and spacing parts of the imprinted SMP nanopattern with different regions. For statistical significance, measurements were performed over 100 locations for each line and spacing parts and the average values are plotted in the graph. The X axis is the pull-off force and the Y axis is the number of counts. As shown, both cases constitute a normal distribution with the average pull-off force being 2.06 nN (standard deviation: 0.365 nN) on the line part and 6.33 nN (standard deviation: 0.37 nN) on the spacing part. This result clearly supports our hypothesis that the imprinted region would be more compressed than non-imprinted region: the difference of density on SMP surface caused a sequential contraction in SMP recovery procedure.

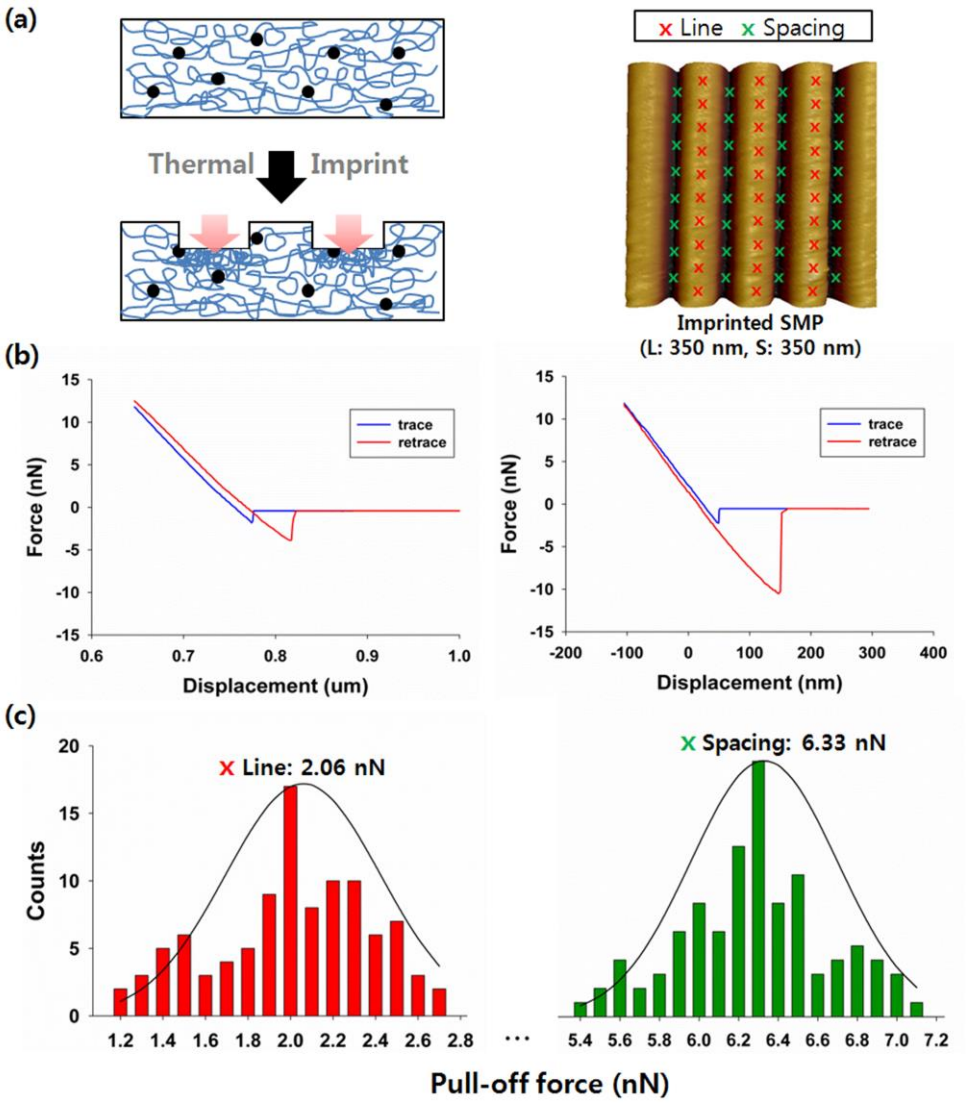

Figure 6. Measurement of the pull-off force in force-distance mode of AFM: (a) Schematic illustration of the density variations along the imprinted surface. Also shown is a three-dimensional AFM image of the imprinted SMP nanopattern with 350 nm line, 350 nm spacing and 350 nm depth. (b) Representative force-distance curves to measure the average pull-off force. (c) Histograms of pull-off force for line (red) and spacing (green) parts of the imprinted SMP nanopattern.

6-3. Supplemental

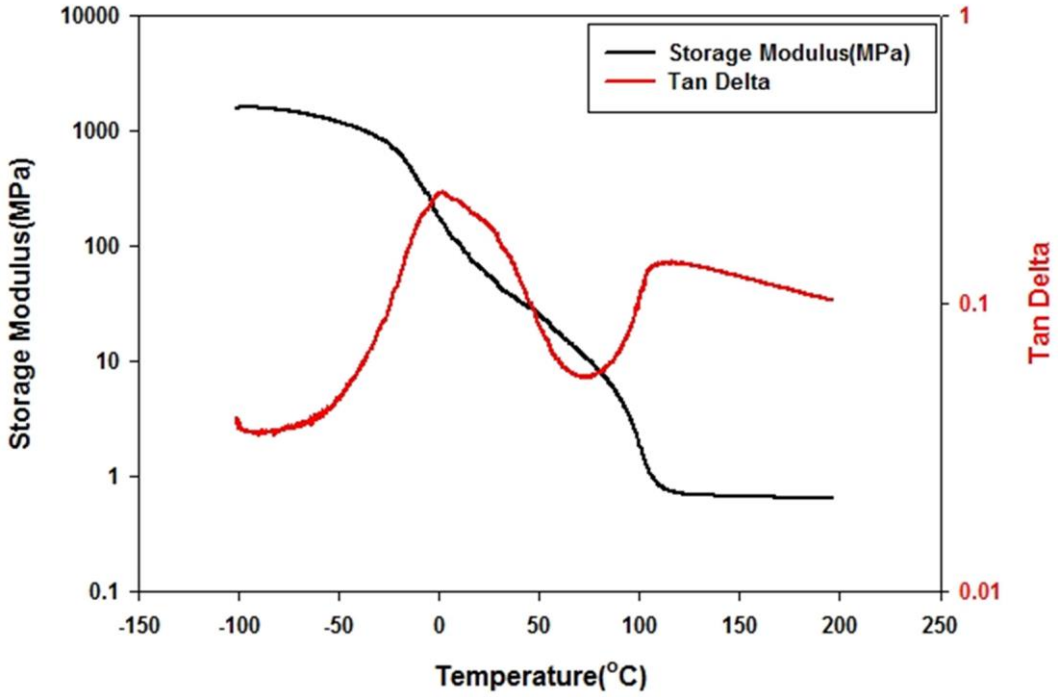

Figure S1. Dynamic Mechanical Analysis (DMA) measurements of a commercial SMP sheet used in our experiment at 1 Hz with a scan rate of 2˚C /min.

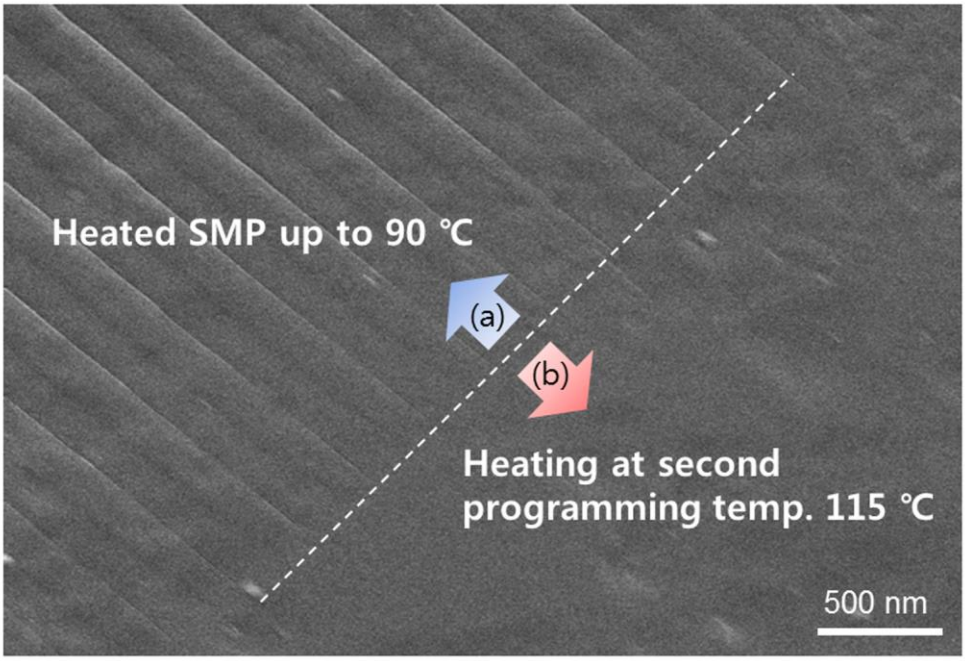

Figure S2. SEM image showing the effect of heating temperature: (a) First, a SMP sheet was heated to 90℃ to recover almost its first memorized shape before stretching. Small traces of nanoimprinting are still seen from the image. (b) The half of the SMP sheet was heated to the second programming temperature (115℃), revealing that the traces have disappeared, resulting in the full recovery of the second memorized shape before stretching.

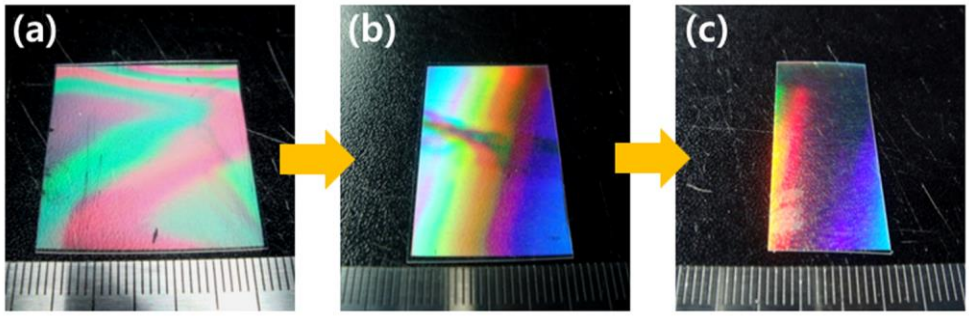

Figure S3. Optical micrographs of SMPs in a series of heating steps: (a) Initial imprinted SMP sheet (900 nm pitch, 400 nm spacing). (b) An intermediate shape (600 nm pitch, 100 nm spacing) (see also Figure 1b) after the recovery process at 85℃. (c) A fully shrunken SMP after the recovery process at 90℃. Some traces of nanopatterns are still seen from the image at this temperature (see also Figure S2).

6-4. Conclusions

We have developed a simple, yet robust method for fabricating size-controllable nanopatterns with reduced sizes and pitches by exploiting the TME of SMPs. Two sequential thermal programming steps were devised to induce selective reduction of the pattern spacing. The method is based on thermal nanoimprinting of a SMP sheet at T_{im} and thermal shrinkage at a temperature above T_{trans} for a certain period of time (~ few minutes) without any further surface modification, allowing for a simple, cheap, and low-expertise route to size and pitch reduction lithography. By utilizing replica molding and self-replication of a UV-curable material together with the TME, a significant size and pitch reduction was achieved for the 400 nm line and 400 nm spacing pattern (pitch: 800 nm). For this specific line-and-space pattern, the final dimension was reduced to 100 nm line and 100 nm spacing (pitch: 200 nm) without modification or collapse of the pattern. Also, it was observed that only the pattern spacing was reduced with the same line width, which was attributed to the enhanced memory effect in the imprinted region, as evidenced by the enhanced density of polymer chains via measurement of pull-off forces.

References

[1] R. Lakes, Nature 1993, 361, 511; C. Sanchez, H. Arribart, M. M. G. Guille, Nat. Mater. 2005, 4, 277; P. Fratzl, F. G. Barth, Nature 2009, 462, 442; E. C. Yusko, J. M. Johnson, S. Majd, P. Prangkio, R. C. Rollings, J. Li, J. Yang, M. Mayer, Nat. Nanotechnol. 2011, 6, 253; T.-S. Wong, S. H. Kang, S. K. Tang, E. J. Smythe, B. D. Hatton, A. Grinthal, J. Aizenberg, Nature 2011, 477, 443; H. C. Ko, M. P. Stoykovich, J. Song, V. Malyarchuk, W. M. Choi, C.-J. Yu, J. B. Geddes Iii, J. Xiao, S. Wang, Y. Huang, Nature 2008, 454, 748.

[2] F. Xia, L. Jiang, Adv. Mater. 2008, 20, 2842.

[3] A. R. Studart, Adv. Mater. 2012, 24, 5024.

[4] H. Lee, B. P. Lee, P. B. Messersmith, Nature 2007, 448, 338.

[5] K. Autumn, Y. A. Liang, S. T. Hsieh, W. Zesch, W. P. Chan, T. W. Kenny, R. Fearing, R. J. Full, Nature 2000, 405, 681.

[6] X. Gao, X. Yan, X. Yao, L. Xu, K. Zhang, J. Zhang, B. Yang, L. Jiang, Adv. Mater. 2007, 19, 2213.

[7] N. Becker, E. Oroudjev, S. Mutz, J. P. Cleveland, P. K. Hansma, C. Y. Hayashi, D. E. Makarov, H. G. Hansma, Nat. Mater. 2003, 2, 278; F. Vollrath, D. P. Knight, Nature 2001, 410, 541; Y. Liu, Z. Shao, F. Vollrath, Nat. Mater. 2005, 4, 901.

[8] Y. Zheng, H. Bai, Z. Huang, X. Tian, F.-Q. Nie, Y. Zhao, J. Zhai, L. Jiang, Nature 2010, 463, 640.

[9] P.-Y. Chen, A. Y.-M. Lin, J. McKittrick, M. A. Meyers, Acta Biomaterialia 2008, 4, 587; H. Rhee, M. Horstemeyer, Y. Hwang, H. Lim, H. El Kadiri, W. Trim, Materials Science and Engineering: C 2009, 29, 2333.

[10] I. H. Chen, J. H. Kiang, V. Correa, M. I. Lopez, P.-Y. Chen, J. McKittrick, M. A. Meyers, Journal of the Mechanical Behavior of Biomedical Materials 2011, 4, 713.

[11] W. Yang, I. H. Chen, B. Gludovatz, E. A. Zimmermann, R. O. Ritchie, M. A. Meyers, Adv. Mater. 2013, 25, 31.

[12] H. E. Jeong, J.-K. Lee, H. N. Kim, S. H. Moon, K. Y. Suh, Proc. Natl. Acad. Sci. U. S. A. 2009, 106, 5639; Y. Xiu, L. Zhu, D. W. Hess, C. Wong, Nano letters 2007, 7, 3388; E. Arzt, S. Gorb, R. Spolenak, Proceedings of the National Academy of Sciences 2003, 100, 10603.

[13] L. Feng, S. Li, Y. Li, H. Li, L. Zhang, J. Zhai, Y. Song, B. Liu, L. Jiang, D. Zhu, Adv. Mater. 2002, 14, 1857.

[14] S. Liao, F. Cui, W. Zhang, Q. Feng, Journal of Biomedical Materials Research Part B: Applied Biomaterials 2004, 69, 158; R. Murugan, S. Ramakrishna, Composites Science and Technology 2005, 65, 2385; S. Wu, X. Liu, T. Hu, P. K. Chu, J. Ho, Y. Chan, K. Yeung, C. Chu, T. Hung, K. Huo, Nano letters 2008, 8, 3803; J. Y. Lim, H. J. Donahue, Tissue engineering 2007, 13, 1879; S. Y. Chew, R. Mi, A. Hoke, K. W. Leong, Biomaterials 2008, 29, 653; J. Tan, W. M. Saltzman, Biomaterials 2004, 25, 3593; V. L. Colvin, Nature biotechnology 2003, 21, 1166; T. Dvir, B. P. Timko, D. S. Kohane, R. Langer, Nat. Nanotechnol. 2010, 6, 13.

[15] J. Han, H. Craighead, Science 2000, 288, 1026; G. Chen, G. T. McCandless, R. L. McCarley, S. A. Soper, Lab on a Chip 2007, 7, 1424; J. O. Tegenfeldt, C. Prinz, H. Cao, R. L. Huang, R. H. Austin, S. Y. Chou, E. C. Cox, J. C. Sturm, Analytical and bioanalytical chemistry 2004, 378, 1678.

[16] H. Cao, J. O. Tegenfeldt, R. H. Austin, S. Y. Chou, Applied Physics Letters 2002, 81, 3058.

[17] C. Ye, L. Zhang, X. Fang, Y. Wang, P. Yan, J. Zhao, Adv. Mater. 2004, 16, 1019; Y. T. Tseng, W. H. Tseng, C. H. Lin, R. M. Ho, Adv. Mater. 2007, 19, 3584.

[18] J. Henzie, M. H. Lee, T. W. Odom, Nat. Nanotechnol. 2007, 2, 549; M. A. Chong, Y. B. Zheng, H. Gao, L. K. Tan, Applied physics letters 2006, 89, 233104; J. A. Rogers, M. Meier, A. Dodabalapur, E. J. Laskowski, M. A. Cappuzzo, Applied physics letters 1999, 74, 3257.

[19] A. R. Parker, H. E. Townley, Nat. Nanotechnol. 2007, 2, 347.

[20] M. Choi, K. Na, J. Kim, Y. Sakamoto, O. Terasaki, R. Ryoo, Nature 2009, 461, 246; Z. Li, Y. Ding, Y. Xiong, Q. Yang, Y. Xie, Chemical communications 2005, 918; R. Srivastava, M. Choi, R. Ryoo, Chemical communications 2006,

4489.
[21] K. Liu, L. Jiang, Nano Today 2011, 6, 155; Q. Chen, N. M. Pugno, Journal of the mechanical behavior of biomedical materials 2012; K. Liu, L. Jiang, ACS nano 2011, 5, 6786.
[22] M. A. Meyers, P.-Y. Chen, A. Y.-M. Lin, Y. Seki, Progress in Materials Science 2008, 53, 1.
[23] W. Peng, X. Hu, D. Zhang, Journal of Magnetism and Magnetic Materials 2011, 323, 2064.
[24] H. J. Ensikat, P. Ditsche-Kuru, C. Neinhuis, W. Barthlott, Beilstein journal of nanotechnology 2011, 2, 152.
[25] L. Feng, Y. Zhang, J. Xi, Y. Zhu, N. Wang, F. Xia, L. Jiang, Langmuir 2008, 24, 4114.
[26] M. Liu, S. Wang, Z. Wei, Y. Song, L. Jiang, Adv. Mater. 2009, 21, 665.
[27] L. J. Gibson, Journal of Biomechanics 2005, 38, 377.
[28] W. Hansen, K. Autumn, Proceedings of the National Academy of Sciences of the United States of America 2005, 102, 385; S. Kim, E. Cheung, M. Sitti, Langmuir 2009, 25, 7196; K. Autumn, A. M. Peattie, Integrative and Comparative Biology 2002, 42, 1081.
[29] S. Gorb, M. Varenberg, A. Peressadko, J. Tuma, Journal of The Royal Society Interface 2007, 4, 271.
[30] K. Autumn, M. Sitti, Y. A. Liang, A. M. Peattie, W. R. Hansen, S. Sponberg, T. W. Kenny, R. Fearing, J. N. Israelachvili, R. J. Full, Proceedings of the National Academy of Sciences 2002, 99, 12252.
[31] P. Vukusic, J. R. Sambles, Nature 2003, 424, 852; M. S. Gudiksen, L. J. Lauhon, J. Wang, D. C. Smith, C. M. Lieber, Nature 2002, 415, 617; R. A. Potyrailo, H. Ghiradella, A. Vertiatchikh, K. Dovidenko, J. R. Cournoyer, E. Olson, Nature Photonics 2007, 1, 123; Y.-F. Huang, S. Chattopadhyay, Y.-J. Jen, C.-Y. Peng, T.-A. Liu, Y.-K. Hsu, C.-L. Pan, H.-C. Lo, C.-H. Hsu, Y.-H. Chang, Nat. Nanotechnol. 2007, 2, 770; H. Kim, J. Ge, J. Kim, S.-e. Choi, H. Lee, H. Lee, W. Park, Y. Yin, S. Kwon, Nature Photonics 2009, 3, 534; Y. Zheng, X. Gao, L. Jiang, Soft Matter 2007, 3, 178; P. Vukusic, I. Hooper, SCIENCE-NEW YORK

THEN WASHINGTON- 2005, 5751, 1151.

[32] S. Weiner, H. D. Wagner, Annual Review of Materials Science 1998, 28, 271; J.-Y. Rho, L. Kuhn-Spearing, P. Zioupos, Medical engineering & physics 1998, 20, 92; A. Bignon, J. Chouteau, J. Chevalier, G. Fantozzi, J.-P. Carret, P. Chavassieux, G. Boivin, M. Melin, D. Hartmann, Journal of Materials Science: Materials in Medicine 2003, 14, 1089; C. Rubin, A. S. Turner, S. Bain, C. Mallinckrodt, K. McLeod, Nature 2001, 412, 603; R. Huiskes, R. Ruimerman, G. H. Van Lenthe, J. D. Janssen, Nature 2000, 405, 704; C. E. Hamm, R. Merkel, O. Springer, P. Jurkojc, C. Maier, K. Prechtel, V. Smetacek, Nature 2003, 421, 841; T. M. Keaveny, E. F. Morgan, G. L. Niebur, O. C. Yeh, Annual review of biomedical engineering 2001, 3, 307.

[33] M. Marin-Grez, J. Fleming, M. Steinhausen, 1986; L. A. Stevens, J. Coresh, T. Greene, A. S. Levey, New England Journal of Medicine 2006, 354, 2473; R. Rodewald, M. J. Karnovsky, The Journal of cell biology 1974, 60, 423; H. G. Rennke, R. S. Cotran, M. A. Venkatachalam, The Journal of cell biology 1975, 67, 638.

[34] S. Singh, J. Houston, C. Frank van Swol, Nature 2006, 442, 526; V. Zorba, E. Stratakis, M. Barberoglou, E. Spanakis, P. Tzanetakis, S. H. Anastasiadis, C. Fotakis, Adv. Mater. 2008, 20, 4049; X. Feng, L. Jiang, Adv. Mater. 2006, 18, 3063.

[35] M. Xu, R. V. Lewis, Proceedings of the National Academy of Sciences 1990, 87, 7120; C. Y. Hayashi, N. H. Shipley, R. V. Lewis, International Journal of Biological Macromolecules 1999, 24, 271; J. M. Gosline, M. E. DeMont, M. W. Denny, Endeavour 1986, 10, 37; J. Gatesy, C. Hayashi, D. Motriuk, J. Woods, R. Lewis, Science 2001, 291, 2603; B. L. Thiel, K. B. Guess, C. Viney, Biopolymers 1997, 41, 703.

[36] A. Rafsanjani, D. Derome, F. K. Wittel, J. Carmeliet, Composites Science and Technology 2012, 72, 744; G. Karam, L. Gibson, Materials Science and Engineering: C 1994, 2, 113; L. S. Evans, Z. Kahn-Jetter, C. Marks, K. R. Harmoney, The Journal of the Torrey Botanical Society 2007, 134, 458; U. G. Wegst, M. F. Ashby, Journal of Materials Science 2007, 42, 9005.

[37] D. H. Kim, N. Lu, R. Ma, Y. S. Kim, R. H. Kim, S. Wang, J. Wu, S. M. Won, H. Tao, A. Islam, K. J. Yu, T. I. Kim, R. Chowdhury, M. Ying, L. Xu, M. Li, H. Chung, H. Keum, M. McCormick, P. Liu, Y. W. Zhang, F. G. Omenetto, Y. Huang, T. Coleman, J. A. Rogers, Science 2011, 333, 838; T. Yamada, Y. Hayamizu, Y. Yamamoto, Y. Yomogida, A. Izadi-Najafabadi, D. N. Futaba, K. Hata, Nat. Nanotechnology 2011, 6, 296; T. Sekitani, U. Zschieschang, H. Klauk, T. Someya, Nat. Mater. 2010, 9, 1015; D. H. Kim, N. Lu, R. Ghaffari, Y. S. Kim, S. P. Lee, L. Xu, J. Wu, R. H. Kim, J. Song, Z. Liu, J. viventi, B. d. Graff, B. Elolampi, M. Mansour, M. J. Slepian, S. Hwang, J. D. Moss, S. M. Won, Y. Huang, B. Litt, J. A. Rogers, Nat. Mater. 2011, 10, 316; A. Milenković, C. Otto, E. Jovanov, Comput. Commun. 2006, 29, 2521.

[38] C. Konya, H. Sanada, J. Sugama, M. Okuwa, Y. Kamatani, G. Nakagami, K. Sakaki, J. Clin. Nurs. 2010, 19, 1236.

[39] M. K. Kwak, H. E. Jeong, K. Y. Suh, Adv. Mater. 2011.

[40] J. M. Karp, R. Langer, Nature 2011, 477, 42.

[41] L. Qu, L. Dai, M. Stone, Z. Xia, Z. L. Wang, Science 2008, 322, 238.

[42] L. Ge, S. Sethi, L. Ci, P. M. Ajayan, A. Dhinojwala, Proc. Natl. Acad. Sci. 2007, 104, 10792; A. Mahdavi, L. Ferreira, C. Sundback, J. W. Nichol, E. P. Chan, D. J. D. Carter, C. J. Bettinger, S. Patanavanich, L. Chignozha, E. Ben-Joseph, Proc. Natl. Acad. Sci. 2008, 105, 2307; C. Greiner, A. del Campo, E. Arzt, Langmuir 2007, 23, 3495; J. S. Kaiser, M. Kamperman, E. J. de Souza, B. Schick, E. Arzt, Int. J. Artif. Organs 2011, 34, 180.

[43] G. Carbone, E. Pierro, S. N. Gorb, Soft Matter 2011, 7, 5545.

[44] E. A. Wilder, S. Guo, S. Lin-Gibson, M. J. Fasolka, C. M. Stafford, Macromolecules 2006, 39, 4138.

[45] S. Gupta, F. Carrillo, C. Li, L. Pruitt, C. Puttlitz, Mater. Lett. 2007, 61, 448.

[46] M. P. Murphy, B. Aksak, M. Sitti, Small 2009, 5, 170.

[47] H. E. Jeong, K. Y. Suh, Nano Today 2009, 4, 335.

[48] H. Yao, H. Gao, J. Mech. Phys. Solids. 2006, 54, 1120; L. F. Boesel, C. Greiner, E. Arzt, A. Del Campo, Adv. Mater. 2010, 22, 2125.

[49] K. Autumn, C. Majidi, R. Groff, A. Dittmore, R. Fearing, J. Exp. Biol. 2006, 209, 3558.
[50] D. Sameoto, C. Menon, J. Micromech. Microeng. 2009, 19, 115002.
[51] H. E. Jeong, M. K. Kwak, K. Y. Suh, Langmuir 2010, 26, 2223.
[52] S. Kim, M. Sitti, Appl. Phys. Lett. 2006, 89, 261911.
[53] H. E. Jeong, K. Y. Suh, Soft Matter 2012, DOI: 10.1039/c2sm07440k.
[54] D. Chandra, S. Yang, Accounts. Chem, Res. 2010, 43, 1080.
[55] D. Chandra, S. Yang, Langmuir 2009, 25, 10430.
[56] K. Johnson, K. Kendall, A. Roberts, Proc. Roy. Soc. Lond. A 1971, 324, 301.
[57] A. Bietsch, B. Michel, J. Appl. Phys. 2000, 88, 4310.
[58] A. Mata, A. J. Fleischman, S. Roy, Biomed. Microdevices 2005, 7, 281.
[59] C. Pang, G. Y. Lee, T. Kim, S. M. Kim, H. N. Kim, S. H. Ahn, K. Y. Suh, Nat. Mater. 2012, 11, 795; W. G. Bae, D. Kim, M. K. Kwak, L. Ha, S. M. Kang, K. Y. Suh, Adv. Health. Mater. 2012, 1.
[60] M. K. Kwak, C. Pang, H. E. Jeong, H. N. Kim, H. Yoon, H. S. Jung, K. Y. Suh, Advanced Functional Materials 2011, 21, 3606.
[61] H. E. Jeong, J. K. Lee, H. N. Kim, S. H. Moon, K. Y. Suh, Proceedings of the National Academy of Sciences 2009, 106, 5639.
[62] L. Ge, S. Sethi, L. Ci, P. M. Ajayan, A. Dhinojwala, Proc. Natl. Acad. Sci. U. S. A. 2007, 104, 10792; D. Sameoto, C. Menon, Smart. Mater. Struct. 2010, 19, 103001; M. K. Kwak, H. E. Jeong, T. Kim, H. Yoon, K. Y. Suh, Soft Matter 2010, 6, 1849; Y. Rahmawan, T. Kim, S. J. Kim, K. R. Lee, M. W. Moon, K. Y. Suh, Soft Matter 2012, 8, 1673.
[63] L. F. Boesel, C. Greiner, E. Arzt, A. Del Campo, Advanced Materials 2010, 22, 2125.
[64] H. E. Jeong, K. Y. Suh, Soft Matter 2012, 8, 5375.
[65] Y. Tian, N. Pesika, H. Zeng, K. Rosenberg, B. Zhao, P. McGuiggan, K. Autumn, J. Israelachvili, Proc. Natl. Acad. Sci. U. S. A. 2006, 103, 19320; Y. Rahmawan, H. Yoon, M. W. Moon, H. G. Jeong, K. Y. Suh, 2012, 1.
[66] S. Reddy, E. Arzt, A. del Campo, Adv. Mater. 2007, 19, 3833.

[67] H. Yoon, H. E. Jeong, T. Kim, T. J. Kang, D. Tahk, K. Char, K. Y. Suh, Nano Today 2009, 4, 385.
[68] M. T. Northen, K. L. Turner, Nanotechnology 2005, 16, 1159.
[69] H. Yoon, M. K. Kwak, S. M. Kim, S. H. Sung, J. Lim, H. S. Suh, K. Y. Suh, K. Char, Small 2011, 7, 3005.
[70] C. Pang, T. Kim, W. G. Bae, D. Kang, S. M. Kim, K. Y. Suh, Adv. Mater. 2012, 24, 445.
[71] M. K. Kwak, H. E. Jeong, K. Y. Suh, Adv. Mater. 2011, 23, 3949.
[72] H. Duan, K. K. Berggren, Nano lett. 2010, 10, 3710; B. Pokroy, S. H. Kang, L. Mahadevan, J. Aizenberg, Science 2009, 323, 237; P. Roca-Cusachs, F. Rico, E. Martinez, J. Toset, R. Farré, D. Navajas, Langmuir 2005, 21, 5542.
[73] G. Carbone, E. Pierro, Small 2012, 8, 1449; S. Kim, B. Aksak, M. Sitti, Appl. Phys. Lett. 2007, 91, 221913.
[74] K. Y. Suh, R. Langer, J. Lahann, Appl. Phys. Lett. 2003, 83, 4250.
[75] N. J. Glassmaker, A. Jagota, C. Y. Hui, W. L. Noderer, M. K. Chaudhury, Proceedings of the National Academy of Sciences 2007, 104, 10786.
[76] L. Shen, N. J. Glassmaker, A. Jagota, C. Y. Hui, Soft Matter 2008, 4, 618; S. Kim, M. Sitti, T. Xie, X. Xiao, Soft Matter 2009, 5, 3689.
[77] S. J. Choi, H. N. Kim, W. G. Bae, K. Y. Suh, J. Mater. Chem. 2011, 21, 14325.
[78] S. H. Crandall, *An introduction to the mechanics of solids*, McGraw-Hill: New York, 1999.
[79] C. Chen, Y. Shi, Y. Zhang, J. Zhu, Y. Yan, Phys. Rev. Lett. 2006, 96, 75505.
[80] J. N. Israelachvili, *Intermolecular and surface forces*, Academic press: San Diego, CA, 1991.
[81] G. Reiter, A. Sharma, A. Casoli, M. O. David, R. Khanna, P. Auroy, Langmuir 1999, 15, 2551.
[82] H. E. Jeong, R. Kwak, A. Khademhosseini, K. Y. Suh, Nanoscale 2009, 1, 331.
[83] K. Liu, J. Du, J. Wu, L. Jiang, Nanoscale 2012, 4, 768.

[84] S. Kim, J. Wu, A. Carlson, S. H. Jin, A. Kovalsky, P. Glass, Z. Liu, N. Ahmed, S. L. Elgan, W. Chen, Proceedings of the National Academy of Sciences 2010, 107, 17095; Y. Mengüç, S. Y. Yang, S. Kim, J. A. Rogers, M. Sitti, Advanced Functional Materials 2012, 22, 1246.

[85] A. Mahdavi, L. Ferreira, C. Sundback, J. W. Nichol, E. P. Chan, D. J. D. Carter, C. J. Bettinger, S. Patanavanich, L. Chignozha, E. Ben-Joseph, A. Galakatos, H. Pyror, I. Pomerantseva, P. T. Masiakos, W. Faquin, A. Zumbuehl, S. Hong, J. Borenstein, J. Vacanti, R. Langer, J. M. Karp, Proceedings of the National Academy of Sciences 2008, 105, 2307.

[86] W. G. Bae, D. Kim, M. K. Kwak, L. Ha, S. M. Kang, K. Y. Suh, Advanced Healthcare Materials 2013, 2, 109.

[87] S. N. Gorb, M. Sinha, A. Peressadko, K. A. Daltorio, R. D. Quinn, Bioinspiration and Biomimetics 2007, 2, S117; B. Aksak, M. P. Murphy, M. Sitti, IEEE Int. Conf. Robotics and Automation (ICRA 2008) 2008, 3058.

[88] W. G. Bae, J. H. Choi, S. H. Lee, D. Kang, K. W. Jung, K. Y. Suh, 3rd IEEE RAS and EMBS Int. Conf. Biomedical Robotics and Biomechatronics (BioRob) 2010, 594; S.-H. Lee, Y.-T. Kim, S. Yang, E.-S. Yoon, D.-E. Kim, K. Y. Suh, ACS Applied Materials & Interfaces 2010, 2, 1308; G. Tortora, P. Glass, N. Wood, B. Aksak, A. Menciassi, M. Sitti, C. Riviere, 2012 Ann. Int. Conf. IEEE Engineering in Medicine and Biology Society (EMBC) 2012, 908.

[89] M. T. Northen, C. Greiner, E. Arzt, K. L. Turner, Advanced Materials 2008, 20, 3905; J. Cui, D. M. Drotlef, I. Larraza, J. P. Fernández-Blázquez, L. F. Boesel, C. Ohm, M. Mezger, R. Zentel, A. del Campo, Advanced Materials 2012, 24, 4601; A. G. Gillies, J. Kwak, R. S. Fearing, Advanced Functional Materials 2013, DOI: 10.1002/adfm.201203122.

[90] E. P. Chan, E. J. Smith, R. C. Hayward, A. J. Crosby, Advanced Materials 2008, 20, 711; P.-C. Lin, S. Vajpayee, A. Jagota, C.-Y. Hui, S. Yang, Soft Matter 2008, 4, 1830; S. Vajpayee, K. Khare, S. Yang, C. Y. Hui, A. Jagota, Advanced Functional Materials 2011, 21, 547.

[91] W. Noderer, L. Shen, S. Vajpayee, N. Glassmaker, A. Jagota, C. Y. Hui, Proceedings of the Royal Society A: Mathematical, Physical and Engineering

Science 2007, 463, 2631; M. P. Murphy, S. Kim, M. Sitti, ACS Applied Materials & Interfaces 2009, 1, 849.
[92] H. Shahsavan, B. Zhao, Soft Matter 2012, 8, 8281.
[93] M. K. Kwak, H. E. Jeong, W. G. Bae, H. S. Jung, K. Y. Suh, Small 2011, 7, 2296; J. Tamelier, S. Chary, K. L. Turner, Langmuir 2012, 28, 8746.
[94] M. D. Bartlett, A. B. Croll, D. R. King, B. M. Paret, D. J. Irschick, A. J. Crosby, Advanced Materials 2012, 24, 1078.
[95] A. del Campo, C. Greiner, I. Á lvarez, E. Arzt, Advanced Materials 2007, 19, 1973.
[96] S. Vajpayee, R. Long, L. Shen, A. Jagota, C.-Y. Hui, Langmuir 2009, 25, 2765.
[97] P. J. Yunker, T. Still, M. A. Lohr, A. Yodh, Nature 2011, 476, 308.
[98] U. Abusomwan, M. Sitti, Applied Physics Letters 2012, 101, 211907.
[99] D. Maugis, *Contact, Adhesion and Rupture of Elastic Solids*, Springer-Verlag, Berlin 1999.
[100] H. Gao, H. Yao, Proceedings of the National Academy of Sciences of the United States of America 2004, 101, 7851.
[101] Y. Tian, J. Wan, N. Pesika, M. Zhou, Scientific Reports 2013, 3, 1382.
[102] Y. Zheng, H. Bai, Z. Huang, X. Tian, F. Q. Nie, Y. Zhao, J. Zhai, L. Jiang, Nature 2010, 463, 640; T. Sun, L. Feng, X. Gao, L. Jiang, Accounts Chem. Res. 2005, 38, 644.
[103] X. Zhang, F. Shi, J. Niu, Y. Jiang, Z. Wang, J. Mater. Chem. 2008, 18, 621.
[104] A. Lafuma, D. Quéré, Nature materials 2003, 2, 457; A. Cassie, S. Baxter, Trans. Faraday Soc. 1944, 40, 546; R. N. Wenzel, Ind. Eng. Chem, 1936, 28, 988; S. Shibuichi, T. Onda, N. Satoh, K. Tsujii, J. Phys. Chem. 1996, 100, 19512; L. Gao, T. J. McCarthy, Langmuir 2009, 25, 14105.
[105] Y. Rahmawan, M. W. Moon, K. S. Kim, K. R. Lee, K. Y. Suh, Langmuir 2009, 26, 484.
[106] L. Gao, T. J. McCarthy, Langmuir 2006, 22, 2966; T. G. Cha, J. W. Yi, M. W. Moon, K. R. Lee, H. Y. Kim, Langmuir 2010, 26, 8319.

[107] X. M. Li, D. Reinhoudt, M. Crego-Calama, Chem. Soc. Rev. 2007, 36, 1350; K. Liu, X. Yao, L. Jiang, Chem. Soc. Rev. 2010, 39, 3240.
[108] L. Xu, R. G. Karunakaran, J. Guo, S. Yang, ACS Appl. Mater. Interfaces 2012, 4; X. Du, X. Li, J. He, ACS Appl. Mater. Interfaces 2010, 2, 2365.
[109] J. Y. Shiu, C. W. Kuo, P. Chen, C. Y. Mou, Chem. Mater. 2004, 16, 561; H. E. Jeong, M. K. Kwak, C. I. Park, K. Y. Suh, J. Colloid Interf. Sci. 2009, 339, 202.
[110] Y. Zheng, L. Jiang, J. Wang, D. Han, Appl. Phys. Lett. 2008, 93, 094107.
[111] H. Tavana, A. Amirfazli, A. Neumann, Langmuir 2006, 22, 5556.
[112] H. S. Lim, J. H. Baek, K. Park, H. S. Shin, J. Kim, J. H. Cho, Adv. Mater. 2010, 22, 2138.
[113] C. Guo, L. Feng, J. Zhai, G. Wang, Y. Song, L. Jiang, D. Zhu, ChemPhysChem 2004, 5, 750.
[114] I. Woodward, W. Schofield, V. Roucoules, J. Badyal, Langmuir 2003, 19, 3432.
[115] M. Morra, E. Occhiello, R. Marola, F. Garbassi, P. Humphrey, D. Johnson, J. Colloid Interf. Sci. 1990, 137, 11.
[116] C. Dong, Y. Gu, M. Zhong, L. Li, K. Sezer, M. Ma, W. Liu, J. Mater. Process. Tech. 2011, 211, 1234.
[117] A. M. Kietzig, S. G. Hatzikiriakos, P. Englezos, Langmuir 2009, 25, 4821; A. M. Kietzig, M. Negar Mirvakili, S. Kamal, P. Englezos, S. G. Hatzikiriakos, J. Adhes. Sci. Technol. 2011, 25, 2789.
[118] Z. Guo, J. Liang, J. Fang, B. Guo, W. Liu, Adv. Eng. Mater. 2007, 9, 316.
[119] M. Qu, B. Zhang, S. Song, L. Chen, J. Zhang, X. Cao, Adv. Funct. Mater. 2007, 17, 593.
[120] K. Tsujii, T. Yamamoto, T. Onda, S. Shibuichi, Angew. Chem. Int. Edit. 1997, 36, 1011; W. Wu, X. Wang, D. Wang, M. Chen, F. Zhou, W. Liu, Q. Xue, Chem. Commun. 2009, 1043.
[121] Z. Guo, F. Zhou, J. Hao, W. Liu, J. Am. Chem. Soc. 2005, 127, 15670.
[122] N. Saleema, D. K. Sarkar, D. Gallant, R. W. Paynter, X. G. Chen, ACS Appl. Mater. Interfaces 2011.

[123] J. Song, W. Xu, Y. Lu, J. Mater. Sci. 2011, 1.
[124] R. Jafari, M. Farzaneh, Appl. Phys. A-Mater. 2011, 102, 195.
[125] X. Men, Z. Zhang, J. Yang, X. Zhu, K. Wang, W. Jiang, New J. Chem. 2011, 35, 881.
[126] K. Ho, S. Newman, Int. J. Mach. Tool. Manu. 2003, 43, 1287.
[127] D. K. Chung, H. S. Shin, M. S. Park, B. H. Kim, C. N. Chu, Int. J. Precis. Eng. Man. 2011, 12, 371.
[128] D. K. Chung, B. H. Kim, C. N. Chu, J. Micromech. Microeng. 2007, 17, 867.
[129] M. Kunieda, B. Lauwers, K. Rajurkar, B. Schumacher, CIRP Ann.-Manuf. Techn. 2005, 54, 64.
[130] P. Bleys, J. P. Kruth, B. Lauwers, B. Schacht, V. Balasubramanian, L. Froyen, J. Van Humbeeck, Adv. Eng. Mater. 2006, 8, 15.
[131] N. Mohd Abbas, D. G. Solomon, M. Fuad Bahari, Int. J. Mach. Tool. Manu. 2007, 47, 1214.
[132] E. Starke, J. Staley, Prog. Aerosp. Sci. 1996, 32, 131.
[133] D. K. Owens, R. C. Wendt, J. Appl. Polym. Sci. 1969, 13, 1741.
[134] G. Nanz, L. E. Camilletti, IEEE T. Semiconduct. M. 1995, 8, 382.
[135] D. K. Chung, H. S. Shin, B. H. Kim, C. N. Chu, Int. J. Precis. Eng. Man. 2011, 12, 1125.
[136] Z. Chen, Y. Guo, S. Fang, Surf. Interface. Anal. 2010, 42, 1.
[137] K. Y. Suh, M. C. Park, P. Kim, Adv. Funct. Mater. 2009, 19, 2699.
[138] J. Henzie, J. Lee, M. H. Lee, W. Hasan, T. W. Odom, Annu. rev. Phys. Chem. 2009, 60, 147; B. J. Wiley, D. Qin, Y. Xia, ACS Nano 2010, 4, 3554; Y. C. Lee, C. Y. Chiu, J. Micromech. Microeng. 2008, 18, 075013; E. A. Costner, M. W. Lin, W. L. Jen, C. G. Willson, Annu. Rev. Mater. Res. 2009, 39, 155; B. D. Gates, Q. Xu, J. C. Love, D. B. Wolfe, G. M. Whitesides, Annu. Rev. Mater. Res. 2004, 34, 339.
[139] L. J. Guo, Adv. Mater. 2007, 19, 495; S. Y. Chou, P. R. Krauss, P. J. Renstrom, Appl. Phys. Lett. 1995, 67, 3114; S. Y. Chou, P. R. Krauss, P. J. Renstrom, Science 1996, 272, 85.

[140] T. Bailey, S. Johnson, S. Sreenivasan, J. Ekerdt, C. Willson, D. Resnick, J. Photopolym. Sci. Tec. 2002, 15, 481; K. Y. Suh, Y. S. Kim, H. H. Lee, Adv. Mater. 2001, 13, 1386.
[141] Y. Zhao, E. Berenschot, M. de Boer, H. Jansen, N. Tas, J. Huskens, M. Elwenspoek, J. Micromech. Microeng. 2008, 18, 064013.
[142] Y. K. Choi, J. Zhu, J. Grunes, J. Bokor, Gabor. A. Somorjai*, §, J. Phys. Chem. B. 2003, 107, 3340; X. M. Yan, S. Kwon, A. Contreras, J. Bokor, G. Somorjai, Nano Lett. 2005, 5, 745.
[143] Q. Xia, K. J. Morton, R. H. Austin, S. Y. Chou, Nano Lett. 2008, 8, 3830.
[144] S. Y. Chou, Q. Xia, Nat. nanotechnology 2008, 3, 295; Y. Wang, X. Liang, Y. Liang, S. Y. Chou, Nano Lett. 2008, 8, 1986.
[145] A. Lendlein, H. Jiang, O. Jünger, R. Langer, Nature 2005, 434, 879.
[146] A. Lendlein, S. Kelch, Angew. Chem. Int. Edit. 2002, 41, 2034.
[147] C. C. Fu, A. Grimes, M. Long, C. G. L. Ferri, B. D. Rich, S. Ghosh, L. P. Lee, A. Gopinathan, M. Khine, Adv. Mater. 2009, 21, 4472; D. Nguyen, D. Taylor, K. Qian, N. Norouzi, J. Rasmussen, S. Botzet, M. Lehmann, K. Halverson, M. Khine, Lab Chip 2010, 10, 1623; D. Dyer, S. Shreim, S. Jayadev, V. Lew, E. Botvinick, M. Khine, Appl. Phys. Lett. 2011, 99, 034102.
[148] Z. Wang, C. Hansen, Q. Ge, S. H. Maruf, D. U. Ahn, H. J. Qi, Y. Ding, Adv. Mater. 2011, 23, 3669.
[149] J. J. Chae, S. H. Lee, K. Y. Suh, Adv. Funct. Mater. 2011, 21, 1146.
[150] K. Kratz, S. A. Madbouly, W. Wagermaier, A. Lendlein, Adv. Mater. 2011, 23, 4058.
[151] T. Xie, K. A. Page, S. A. Eastman, Adv. Funct. Mater. 2011, 23, 4058; L. Sun, W. M. Huang, Soft Matter 2010, 6, 4403.
[152] M. Bothe, K. Y. Mya, E. M. J. Lin, C. C. Yeo, X. Lu, C. He, T. Pretsch, Soft Matter 2012, 8, 965; T. Xie, Nature 2010, 464, 267.
[153] S. Ota, Radiat. Phys. Chem. 1981, 18, 81; K. Nakayama, J. Soc. Rubber Ind., Jpn. 1990, 63, 529; W. Chen, K. Xing, L. Sun, Radiat. Phys. Chem. 1983, 22, 593.
[154] A. Lendlein, S. Kelch, Angew. Chem. Int. Edit. 2002, 41, 2034.

[155] H. E. Jeong, R. Kwak, J. K. Kim, K. Y. Suh, Small 2008, 4, 1913.
[156] Q. Xia, S. Y. Chou, Nanotechnology 2008, 19, 455301; M. H. Lee, M. D. Huntington, W. Zhou, J. C. Yang, T. W. Odom, Nano Lett. 2011, 11, 311.
[157] X. Liang, K. J. Morton, R. H. Austin, S. Y. Chou, Nano Lett. 2007, 7, 3774.
[158] L. Yang, J. Chen, Y. Guo, Z. Zhang, Appl. Surf. Sci. 2009, 255, 4446.
[159] Y. S. Woo, J. K. Kim, D. E. Lee, K. Y. Suh, W. I. Lee, Appl. Phys. Lett. 2007, 91, 253111; J. K. Kim, D. E. Lee, W. I. Lee, K. Y. Suh, Nanotechnology 2010, 21, 295306.

국문초록

본 논문은 자연계에 존재하는 다양한 생물체들이 가지고 있는 마이크로/나노 스케일의 미세구조물에 대한 멀티스케일 분석을 통한 그 특성을 파악하고, 기존의 인류에게 필요로 했지만 극복하기 어려웠던 다양한 문제들을 해결하기 위한 자연모사 관점의 공학적 설계와 제조방법을 제시한 연구이다. 자연계의 많은 동물들은 진화라는 시스템을 바탕으로 독특한 기능성들을 가지고 있는데, 이러한 특정 기능성을 발현하게 되는 원인을 그들의 독특한 구조로부터 기인하는 것으로 보고, 최근 발달된 마이크로/나노 기술을 바탕으로 인류가 원하는 다양한 기능성을 가지는 생물체를 연구하였다. 구체적으로 본 연구에서는 초소수성 표면, 건식접착 표면에 대하여 이론적 접근 및 해석을 통하여, 기능성을 최대화 할 수 있는 최적설계 방안을 제시하고 이러한 기능성 표면을 모방한 인공적인 표면을 제작 함으로써 그 응용 연구까지 수행 하였다.

첫 번째로, 본 논문에서는 기존의 건식접착 표면의 문제점으로 지적되어온 복잡한 공정 및 높은 공정비로 인한 상용화의 문제점과 표면에 나노 구조물로 인하여 재사용이 불가능 하다는 문제점을 해결하고자 하였다. 그 결과 마이크로 구조물에 재료적인 복합구조를 제안하여, 자연계의 마이크로/나노 구조물의 기능성을 모방하였고 최적설계를 통한 구조물 제작으로 인하여 높은 접착 표면을 제작 할 수

있었다. 구체적으로, 마이크로 섬모구조의 기둥 부분을 높은 탄성계수를 가지는 고분자 재료(hard polydimethylsiloxane (h-PDMS), Young's modulus: ~8.2 MPa) 로 1 차적으로 성형을 하고, 섬모 끝단은 낮은 탄성계수를 가지는 고분자 재료 (PDMS with a higher amount of curing agent, e.g., 15%, Young's modulus: ~2.8 MPa)로 코팅을 하여 복합재료로 이루어진 건식접착 마이크로 구조물을 제안하였다. 이러한 섬모구조의 특징은, 높은 탄성계수로 인한 섬모의 무너짐 방지 효과가 있을 뿐만 아니라 섬모와 섬모간의 접촉으로 인한 섬모의 무너짐 현상도 효과적으로 방지할 수 있는 장점을 가진다. 그리고 섬모 끝단의 낮은 고분자 물질로 인하여 마치 나노 섬모 구조가 있는것과 같은 효과를 지니게 되는데, 그 특징으로 나노 거칠기를 가지는 표면에 균일한 접착(Conformal contact)을 유도하게 되는 장점이 있다. 그로 인하여 기존의 건식 접착 표면에 비해서 내구성은 보장하면서 높은 접착력을 보이는 건식 접착 패치를 제작 할 수 있었다. 이러한 패치의 장점은 민감한 사람 피부와 같은 거친 표면에도 잘 접착 할 수 있다는 것인데, 이러한 특징을 이용하여 생체 신호를 실시간을 측정 할 수 있는 생체 신호 측정 건식접착 패치의 응용 연구 또한 수행 하였다. 연구 결과 기존의 생체신호 측정 패치와 비교하여 동일한 수준의 신호를 측정 함으로써 미래사회의 노령화로 인한 패치 사용의 증가 및 입는 또는 붙이는 전자기기의 접착을 위한 훌륭한 대안을 제시 하였다.

나아가, 건식접착 패치의 독특한 기능성 중의 하나인, 접착

표면에 이물질을 남기지 않는 특징을 이용한 청정 이송 장치를 위한 새로운 건식접착 섬모구조를 제안하였다. 새로운 섬모 구조는 섬모의 끝단이 모두 연결된 구조(Bridged structure)로써 단순 섬모 구조보다 3 배이상의 높은 접착력과 3 배 이사 빠른 탈착 속도가 특징이다. 이러한 접착 패치를 이용하여 웨이퍼와 유리 패널을 효과적으로 이송하는 장비를 설계하고 제작하였다. 그 결과 기존 이송 장치 보다 30% 빠르게 이송 가능한 결과를 확인 하였다.

다음으로, 자연계의 대표적인 기능성 표면인 초소수성 표면을 마이크로/나노 구조물 관점에서 분석하고, 기존의 고분자 기반의 표면으로 인하여 내구성으로 인해서 상용화 및 산업화가 되지 못했던 문제점을 해결 하였다. 기존 초소수성 표면의 가장 큰 문제점인 내구성을 획기적으로 개선하기 위해서, 본 연구에서는 금속을 이용한 마이크로/나노 멀티스케일 구조물을 간단한 가공 방법으로 제작할 수 있는 공정을 최초로 제안하였다. 그 결과 외부의 물리적인 자극을 가한 후에도 초소수성 특성을 잘 유지하는 표면을 제작 하였고, 기존의 웨이퍼 기반의 소면적 공정을 금속 가공 기반의 대면적 공정으로 대체할 수 있음을 확인 하였다. 이러한 금속 초소수성 표면은 엔진, 기차 표면, 비행기 표면 등에 폭넓게 활용 될 수 있을 것으로 기대한다.

주요어: 생체모사 공학, 건식접착 표면, 나노 섬모, 피부 부착형 디바이스, 멀티스케일 구조물, 초소수성 표면, 형상기억 폴리머

학번: 2009-21069